THREE DIMENSIONAL ACOUSTIC MICROBUBBLE DYNAMICS NEAR RIGID BOUNDARY

by

Kawa M A Manmi

A thesis submitted to
The University of Birmingham
for
Doctor of Philosophy

School of Mathematics
The University of Birmingham
January 2015

Abstract

Dynamics of cavitation microbubbles due to high intensity ultrasound are associated with important applications in biomedical ultrasound, ultrasonic cleaning and sonochemistry. Previous numerical studies on this phenomenon were for an axisymmetric configuration. In this thesis, a computational model is developed to simulate the three dimensional dynamics of acoustic bubbles by using the boundary integral method. A bubble collapses much more violently subjected to high intensity ultrasound than when under normal constant ambient pressure. A few techniques are thus implemented to address the associated numerical challenge. In particular, a high quality mesh of the bubble surface is maintained by implementing a new hybrid approach of the Lagrangian method and elastic mesh technique. It avoids the numerical instabilities which occur at a sharp jet surface as well as generates a fine mesh needed at the jet surface.

In Chapter 2, we explore microbubble dynamics near a wall subjected to ultrasound propagating parallel to the wall, where the Bjerknes forces due to the ultrasound and the wall are perpendicular to each other. The jet direction depends mainly on the dimensionless standoff distance $\gamma = s/R_{\max}$ of the bubble from the wall, where s is the distance between the wall and the bubble centre at inception and $R_{\max}$ is the maximum bubble radius.

In Chapter 3, we study the dynamics of ultrasound contrast agents (UCAs), which are microbubbles stabilized with a thin shell. The effects of the encapsulating shell are

approximated by adapting Hoff's model for thin-shell contrast agents. The oscillation amplitude and period reduce significantly due to the coating. A bubble jet forms when the amplitude of ultrasound is sufficiently large. The effects of shell thickness and viscosity are analyzed and determined to affect the bubble dynamics, including jet development.

In Chapter 4, the viscous effects on microbubble dynamics are investigated, using the boundary integral method coupled with the viscous potential flow theory. The viscous effects are incorporated into the model through including the normal viscous stress and viscous correction pressure at the bubble surface. The model agrees well with the Gilmore equation for a spherical bubble for several cycles, and the experimental data and the axisymmetric model based on the Navier-Stokes equation for transient gas bubble dynamics near a rigid boundary. The viscous effects in microbubble dynamics are analyzed in terms of jet velocity, centroid movement, Kelvin impulse, bubble energy and bubble volume, etc.

In Chapter 5, we model and simulate three dimensional toroidal bubble dynamics using the vortex ring model. The transform from a singly connected bubble to a toroidal bubble is performed automatically. The potential due to a vortex ring is calculated by using the Biot-Savart law where the integral from the infinite to the point considered is performed analytically. We evaluate the numerical model by comparing with the axisymmetric BIM and the experiment result. We analyse toroidal bubble dynamics subject to buoyancy near a vertical wall, including jet impacting and rebounding toroidal bubbles with oblique jetting.

Acknowledgments

First and foremost I wish to thank my supervisor, Dr Qianxi Wang, for his support and guidance over the course of my studies. Your door has always been open and I very much appreciate everything you have done. It has been both a pleasure and privilege working with you.

I would like to thank the members of staff at the University of Birmingham who have assisted me on several occasions.

I gratefully acknowledge the funding I received from my scholarship Kurdistan Regional Government (KRG).

My PhD studies would not have been possible without the support of my wonderful (and very patient) wife Narmeen. I am truly grateful for your support, encouragement and wise words. I would also like to say a special thanks to my parents, Fatim and Mustafa,for their belief that I would finish it.

LIST OF PAPERS AND ABSTRACTS

Papers accepted for publication directly from this doctoral research

1. Q. X. Wang, and **K. Manmi**, Three dimensional microbubble dynamics near a wall subject to high intensity ultrasound, *Phys. Fluids* (1994-present) 26(3), 032104 (2014).

2. Q. X. Wang, **K. Manmi** and Michael L. Calvisi, Numerical modeling of the 3D dynamics of ultrasound contrast agent microbubbles using the boundary integral method , *Phys. Fluids*. Accepted.

In addition, the following abstracts arose from presentations of material from this thesis

1. Michael Calvisi, **Kawa Manmi** and Qianxi Wang, Numerical Modeling of 3-D Dynamics of Ultrasound Contrast Agent Microbubbles Using the Boundary Integral Method. *67th Annual Meeting of the APS Division of Fluid Dynamics*. Volume 59, Number 20, November 2325, 2014; San Francisco, California.

2. Kuo-Kang Liu, **Kawa Manmi** and Qianxi Wang, Cell mechanics in biomedical cavitation. *Amazing (cavitation) bubbles: great potentials and challenges. Royal Society's Theo Murphy Intl. Sci. Meeting*, 2014

Table of Contents

Chapter 1

Introduction

1.1 Application background

Traditional research on bubble dynamics has been associated with cavitation on fast ship propellers and turbines, as well as with underwater explosions. About one century ago, the first cavitation observation was identified in heavy erosion of ship propellers after a short time in use [98]. Later found that the cavitation may occur in many type of hydraulic and hydrofoil machineries. The propeller is eroded which may reduce the efficiency and also underwater noise is produced, all effects unwanted.

The cavitation also occurred when the bubble motion driven by acoustic wave, known as acoustic cavitation. Recently microbubble dynamics due to ultrasound have become a hot research topic, because it is associated with important applications in cavitation cleaning, chemical reactions (sonochemistry) and biomedical ultrasound.

Acoustically driven cavitation is one of the most effective cleaning procedures for electrical and medical micro-devices [101, 87, 66]. Bubble collapse near a solid surface results in high-speed liquid jets impinging on the solid, responsible for ultrasonic cleaning. In sonochemistry, acoustic cavitation is used to promote mixing and reactions [7, 37]. High

strain rates in the immediate vicinity of a bubble can lead to polymer cleavage. A vigorous acoustic jet can have important mixing, molecular, and bond-cleavage effects and for catalysis of heterogeneous chemical reactions.

The medical applications includes extracorporeal shock wave lithotripsy [28, 57, 48, 12, 69, 49], tissue ablating (histotripsy) [99, 21, 22], and oncology and cardiology [70]. In those applications, cavitation microbubbles absorb and concentrate significant amounts of energy from ultrasound, leading to violent collapsing, shock waves and bubble jetting [123]. These mechanisms are also associated in sonochemistry [104, 68, 5] and ultrasound cavitation cleaning - one of the most effective cleaning processes for electrical and medical micro-devices [101, 87].

The coated microbubbles are widely used as ultrasound contrast agents (UCAs) in nondestructive medical imaging [108]. When injected into the bloodstream they can travel to all organs of the body. Their high compressibility relative to the surrounding blood and tissues leads to strong scattering of ultrasound, thereby enhancing blood-tissue contrast in the resulting image. For this reason, they have gained widespread applications in clinical diagnostic ultrasound to enhance contrast of cardiographic or radiologic features [30]. While UCAs have been commercially available since 1991 [25, 46], they have more recently generated interest for use in therapeutic applications, for example, as vehicles for drug delivery and gene therapy [21] , and thermal and mechanical tissue ablation [54, 130].

UCAs are rapidly evolving from the diagnostic modality into a therapeutic tool [21]. One important potential application is to use UCAs to deliver a drug/gene. Upon arriving at a target, the microbubbles are activated by ultrasound, leading to violent collapse. This violently collapsing bubbles release the drug/gene cargo [14, 53, 61] and also cause cell membranes nearby to become perforated and thus temporarily leaky, a phenomenon known as sonoporation [86, 62]. It aids the gene/drug to enter the target cells via diffusion

and also convection if microjets arise [38, 78]. The relevance of this work in a clinical context is underscored by the recent experiment of Chen et al. [18]. They observed that coated ultrasound bubbles in micro-blood-vessels of rat mesentery are often associated with large non-spherical deformation and high speed liquid jetting.

Bubbles tend to maintain sphericity due to surface tension. When subjected to ultrasound, its pressure gradient generates non-spherical bubble motion. If the wave is strong enough a high-speed liquid jet forms towards the end of the collapse phase. Recently, there were several studies into jetting for acoustic bubbles for an axisymmetric configuration for a bubble in an infinite liquid by Calvisi et al. [13], Wang and Blake [121, 122], and near a boundary subjected to ultrasound propagating in the direction perpendicular to the boundary by Klaseboer and Khoo [58, 59], Fong et al. [40, 39] , Calvisi et al. [13, 12], Curtiss et al. [22]. This study is concerned with three-dimensional bubble dynamics near a wall subjected to ultrasound.

1.2 Research review

In order to effectively utilize microbubble in biomedical applications, it is necessary to understand the interplay between the incident ultrasound and the dynamics of the encapsulated microbubbles. While several theoretical models have been proposed to model UCAs, they have been mainly restricted to the case of spherical oscillations [19, 41, 45, 84, 44, 17, 79, 107, 34, 33, 88]. Liu et al. [76] investigated the shape stability of a nearly spherical bubble encapsulated by a viscoelastic membrane in an ultrasound field. They derived the equations for the shape oscillation of an encapsulated bubble and predicted the stability condition.

Nonspherical oscillations of microbubble can clearly arise, particularly at large ultrasound amplitudes due to instability of the spherical mode and also in the proximity of

surfaces, such as surrounding tissues [25, 96, 97, 36, 81]. The manifestation of nonspherical oscillations has several implications in the context of utilizing UCAs for biomedical applications.

First, nonspherical surface modes give rise to frequency components subharmonics, harmonics and ultraharmonics that are not at the incident ultrasound frequency as can the spherical mode if driven to a nonlinear response [21]. These additional frequency components contribute to the signal scattered by UCAs, and are important for distinguishing the microbubbles from the surrounding tissue, thus enhancing contrast [36]. Experimental observations of pulsating contrast agents indicate the possibility for parametric excitation of nonspherical modes [36]. Tsigklifis and Pelekasis [106] studied nonlinear stability of pulsating contrast agents in the context of axisymmetry using the boundary element method. They accounted for inertia effects and pressure changes in the host fluid, coupled with stretching and bending elastic forces in the shell that coats the microbubble.

Second, it is well known that the oscillation of bubbles near a surface can give rise to phenomena including microstreaming around the bubble [1, 85, 32] and the generation of high-speed jets during bubble collapse [8, 9]. In the case of a rigid or semi-rigid surface, these jets form on the distal side of the bubble and are directed toward the surface. If sufficiently violent, such jets can cause localized damage, as evidenced in ship propellers affected by cavitation nucleation on the low pressure side and in silicon wafers subject to ultrasonic cleaning.

Chen et al. [18] observed that coated ultrasound bubbles in microscopic blood vessels of rat mesentery are often associated with nonspherical deformation and liquid jetting (see figure 1.1). This phenomenon was also observed by Vos et al. [110, 111]. In this case of UCAs, a jet may potentially enhance tissue poration or cause mechanical destruction of cells. Such a mechanism may be desired in the case of tumor destruction, for instance,

but may be undesirable in cases where tissue integrity must be maintained. In either case, an understanding of the relationship between the tissue environment, the incident ultrasound, the mechanical properties of the material encapsulating the UCAs, and the ensuing microbubble dynamics is critical for utilizing UCAs with maximum efficacy in any clinical setting.

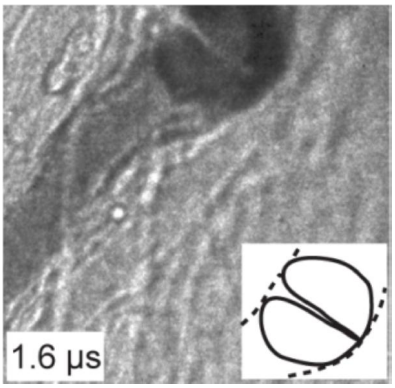

Figure 1.1: Vascular rupture in rat mesentery involving a liquid jet [18]. The amplitude of ultrasound is 4 MPa and the vessel diameter is 15 μm. Sketches are shown of the bubble jet in solid lines and the microvessel in dashed lines.

The complex nature of nonspherical bubble oscillations makes them less amenable to analytical modeling and invites the application of numerical methods to describe their dynamics. In this study, we use the boundary integral method to study the dynamics of coated and uncoated microbubble near a rigid wall subject to ultrasound propagating parallel and perpendicular to the boundary.

Hsiao & Chahine [47] recently modeled the bubble coating using a layer of Newtonian viscous fluid. Their model did not consider the elastic features of the coating, which we believe is an essential feature of bubble coatings since they are viscoelastic materials. Their model is threedimensional, yet all the cases presented are axisymmetric, where azimuthal averaging was applied to smooth the value of curvature computed. The complexity of the phenomenon and the significant challenges involved in modeling them mathematically

have resulted in this being a very sparsely addressed area, despite the large numbers of experimental studies on therapeutic ultrasound that have been performed worldwide.

The boundary integral method (BIM) is widely used in simulating bubble dynamics [8, 9, 15], which is grid free in the flow domain. Acoustic bubble dynamics were simulated using an axisymmetric BIM model for a bubble in an infinite liquid [13, 121, 122] and near a boundary subject to ultrasound propagating in the direction perpendicular to the boundary [58, 59, 40, 39, 22]. In this study we implement the three-dimensional BIM model for microbubble dynamics subjected to ultrasound. A bubble collapses much more violently subjected to a high intensity ultrasound than when under normal constant ambient pressure. As an example, the jet develops much faster when subjected to high intensity ultrasound and its speed is significantly larger. A few techniques are implemented to model the associated violent collapse. In this study, a high quality surface mesh is maintained by implementing a hybrid approach of the Lagrangian method and elastic mesh technique. The bubble surface is updated using the fourth-order Runge-Kutta method and interpolated using a polynomial scheme coupled with the moving least square method. These works were based on the inviscid potential flow theory, but the viscous effects may not be negligible for micron size bubbles [67, 93, 72].

Transient gas bubble dynamics including viscous effects were simulated based on the Navier-Stokes equations using the finite volume method or finite element method [93, 56, 83]. Domain simulation of this multi-scaled problem of multiple oscillations is computational demanding. As such simulations based on the domain approaches are usually carried out for axisymmetric configurations and for one cycle of oscillation.

Viscous fluid dynamics can be described approximately by potential flows when the vorticity is small or is confined to a narrow layer near the boundary. It is particularly useful for a gasliquid two-phase flow with an interface. A key issue in the theory is that

the shear stress should approximately vanish at a gas-liquid interface, but it does not in the irrotational approximation. An auxiliary function, the viscous pressure correction to the potential pressure, has been introduced to address this discrepancy by Joseph et al. [51, 50]. They argued that the power done by the shear stress due to the irrotational flow should be equal to the power done by the viscous correction pressure to conserve the energy of the system. Accurate physical descriptions of the viscous flows have been provided by the viscous potential theory with the viscous pressure correction, including the motion of bubbles and drops [50, 51], capillary instability of a liquid cylinder [115, 114], the decay of free surface waves [50–52], and the Kelvin-Hemholtz instability [55].

This theory was applied for transient bubble dynamics based on the BIM by Lind & Phillips [71–73] for transient bubbles near a boundary in a axisymmetric configuration, and by [60, 131] for a bubble rising and deforming in a viscous liquid. In chapter four, we will model 3D microbubble dynamics in a viscous liquid subject to ultrasound using the viscous potential theory of Joseph et al. [50, 51] based on the following three considerations.

Firstly, the Reynolds number R_e for the liquid flow associate with acoustic microbubble dynamics appears large. $R_e = \rho R_0^2 \omega_M / \mu$, where R_0 is the equilibrium radius of the bubble,ρ and μ are the density and viscosity of the liquid and ω_M is the larger of the natural frequency of the bubble and the ultrasound frequency. The natural frequency of a bubble is $\omega_b = \frac{1}{R_0}\sqrt{\frac{2p_0}{\rho} + \frac{4\sigma}{\rho R_0}}$ where p_0 is the ambient pressure and σ is the surface tension. It can be estimated that $R_e \geq 42$ as $R_0 \geq 2$ μm, using with the following parameters for water: $p_0 = 100$ kPa, $\rho = 1000$ kg/m^3, $\mu = 10^{-3}$ Pa s and $\sigma = 0.07$ N/m. Microbubble dynamics are thus usually associated with an irrotational flow in the bulk volume but a thin vorticity layer at the bubble surface.

Secondly, a bubble is approximately spherical during most of lifetime due to surface tension. In the case of spherical bubbles, viscosity only enters the analysis through the normal

stress on the surface of the bubble but plays no role in the fluid body, apart from viscous dissipation. Physically this is realized in the extra work required to expand the bubble against the additional normal viscous force on the bubble surface [42, 92].

Thirdly, a bubble subject to ultrasound may become nonspherical during a very short period at the end of collapse [123], when the inertial effects are dominant and the viscous effects are not significant.

When a bubble collapses in non-spherical environment, a high speed liquid jet often forms. The jet subsequently penetrates through the bubble forming a toroidal bubble. The liquid domain is transformed from a singly-connected to a doubly-connected form, which results in non-uniqueness to the potential problem. The doubly-connected domain can be made singly-connected by using a vortex sheet by Zhang et al. [134] and Zhang & Duncan [133] or a branch cut by Best [2]. The vortex sheet model describes the shear layer around the jet surface, but the associated boundary integral equation is high order and relatively unstable.

Pedley [90] and Lundgren & Mansour [77] modelled the dynamics of a bubble ring with a vortex ring inside, started with a circular cross-section. Wang et al. [124, 126] developed a vortex ring model from these earlier ideas to model toroidal bubbles generated due to jet impact. In this model, a vortex ring is placed inside the toroidal bubble once the jet impacts on the opposite bubble surface. The strength of the vortex-ring is equal to the jump of the potential across the contact point at the time of impact.

Zhang et al. [135] simulated three-dimensional (3D) toroidal bubble dynamics using the vortex ring model. Wang et al. [113, 112] developed an elastic mesh technique (EMT) for improving the mesh quality for the simulation of toroidal bubbles. Zhang et al. [132] simulated the three-dimensional interaction of a toroidal bubble and a free surface using the vortex ring model.

The challenging in the 3D model is largely due to the detailed numerical techniques of transition from a singly connected bubble to a toroidal bubble, the surface mesh for toroidal bubble where the liquid hole through the bubble is thin at the beginning of the toroidal phase, as well as the calculation of the potential due to a vortex ring, etc.

1.3 Thesis overview

In chapter 1, the application background and research of acoustic cavitation bubble dynamics are reviewed. In Chapter 2, a computational model is developed to simulate the three dimensional dynamics of acoustic bubbles near rigid boundary by using the boundary integral method. A few techniques are implemented to improve the numerical model. In particular, a high quality mesh of the bubble surface is maintained by implementing a new hybrid approach of the Lagrangian method and elastic mesh technique. It avoids the numerical instabilities which occur at a sharp jet surface as well as generates a fine mesh needed at the jet surface. In the Lagrangian approach, the nodes on the bubble surface are updated with the material velocities at the nodes. This may result in a poor quality mesh for a non-spherical bubble motion at large amplitude. In the EMT the mesh sizes on the bubble surface tends to be uniform. The optimum mesh is obtained by using artificial tangential velocity plus prescribed normal velocity to update the bubble surface. The artificial tangential velocity is obtained by minimizing the total elastic energy as assumed that the segments of the mesh have some stored energy. However, non-uniform mesh is more suitable for a bubble surface with a varying curvature. A finer mesh should be used for the part of the bubble surface where the curvature radius is small, such as around the jet surface. We showed that a high quality surface mesh with suitable mesh density variation can be obtained by implementing a hybrid approach of the Lagrangian method and elastic mesh technique. We implemented the hybrid approach in all chapters. To evaluate the numerical model, the convergence test to the mesh size is conducted. The

numerical model is validated against the Rayleigh-Plesset equation and an axisymmetric model for spherical and axisymmetric cases, respectively. We then exam bubble dynamics near a wall subjected to ultrasound, including the bubble shape and Kelvin impulse, jet shape and velocity, etc. in terms of the dimensionless standoff distance of the bubble from the wall and the amplitude of ultrasound.

The acoustic radiation forces on gas bubbles are normally referred to as Bjerknes forces after C. A. Bjerknes and his son V. F. K. Bjerknes, who were the first to report on such forces [6]. It is conventional to divide the Bjerknes forces into two types, namely, primary Bjerknes forces, which are experienced by single bubbles due to pressure gradients in the liquid, and secondary Bjerknes forces, which are responsible for bubble-wall and bubble-bubble interactions [35]. When acoustic wave propagating parallel to the boundary Bjerknes force due to the ultrasound (primary Bjerknes) and the wall are perpendicular (secondary Bjerknes) to each other.

In Chapter 3, we investigate the dynamics of coated bubbles using a BIM model adapted to account for the effect of the encapsulation. We assume the shell is much thinner than the bubble radius and is comprised of a linear, incompressible, and viscoelastic solid. We adapt the Hoff model [44] for spherical bubbles to nonspherical bubbles by replacing the radius with the inverse of the local mean curvature in the model. The numerical model is validated by comparing with the modified Rayleigh-Plesset equation for coated spherical bubbles. Results of numerical analyses for the dynamics of UCAs in an infinite fluid and near a rigid wall subject to acoustic waves propagating parallel and perpendicular to the wall, presented respectively, in parameter regimes of clinical relevance.

In Chapter 4, this chapter investigates the viscous effects in bubble dynamics using the boundary integral method based on the viscous potential flow theory. The viscous effects are incorporated into the model through including the normal viscous stress in the dynamic

boundary condition at the bubble surface. The viscous correction pressure of Joseph [50, 51] is implemented to resolve the discrepancy between the non-zero shear stress of the irrotational flow at a free surface and the physical boundary condition of zero shear stress. The 3D model is validated by comparing with the Gilmore equation for spherical bubble oscillating in a viscous and unbounded fluid, the experiment [86] and the volume of fluid method (VOF) based on the Navier-Stokes equation [83] for the dynamics of a transient bubble near a rigid boundary. we analyze bubble dynamics near a rigid boundary subject to ultrasound travelling perpendicular and parallel to the boundary, respectively.

In Chapter 5, three dimensional bubble dynamics in toroidal phase are modelled based on the vortex ring model. The transformation from a singly connected bubble to a toroidal bubble is performed automatically. The potential due to a vortex ring is calculated directly from Biot-Savart law. The model was validated with the experimental data [74] and axisymmetric model [126] for a toroidal bubble near a horizontal rigid boundary. We analyzed toroidal bubble dynamics near a vertical rigid boundary subject to buoyancy force.

Finally the summary and conclusions of the thesis and possible future developments are presented in Chapter 6.

Chapter 2

Three dimensional microbubble dynamics near a wall subject to high intensity ultrasound

2.1 Physical and mathematical model

Consider the dynamics of a microbubble near an infinite rigid plane wall subjected to ultrasound, as shown in figure 2.1. A Cartesian coordinate system $O-xyz$ is adopted with the origin at the centre of the initial spherical bubble, the z-axis perpendicular to the wall and the x-axis along the wave direction. The ultrasound is described as a plane harmonic acoustic wave as follows,

$$p_\infty(x,t) = p_0 + p_a \sin(kx - \omega t + \phi_0), \tag{2.1.1}$$

where p_0 is the hydrostatic pressure, t is time, and k, p_a, ω and ϕ_0 are the wave number, pressure amplitude, angular frequency, and phase shift of the ultrasound. The initial phase ϕ_0 in this study is chosen as zero unless stated otherwise. We assume that the pressure p_b

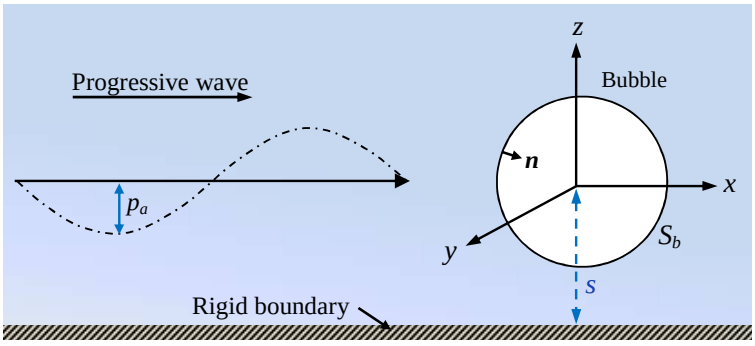

Figure 2.1: Configuration and coordinate system for a microbubble near a rigid wall subjected to ultrasound propagating parallel to the wall.

within the bubble is uniform and consists of the vapour pressure p_v and the gas pressure p_g. Assuming that the non-condensing gas is ideal and its expansion and compression are adiabatic, the bubble pressure is given in terms of the bubble volume V according to Dalton law as follows [11],

$$p_b = p_v + p_g = p_v + p_{g0}\left(\frac{V_0}{V}\right)^{\kappa} \tag{2.1.2}$$

where p_{g0} is the initial gas pressure of the bubble, V_0 is the initial bubble volume and κ is the ratio of specific heats of the gas.

We neglect the viscous effects of the surrounding liquid, since we are concerned with a violent collapsing bubble subjected to high intensity ultrasound where the Reynolds number of the liquid flow is large. More complicated models are available in the literature mainly for an axisymmetric configuration (as an example Yang and Prosperetti [127], in which heat transfer and viscous effect were taken into account). The compressible effects of the liquid may cause a substantial energy loss of a bubble system at the end of the collapse phase and affects the subsequent oscillations of the bubble significantly [121, 122, 119]. However, bubble dynamics during the first oscillation, including the bubble shape and jet velocity, are not affected significantly by the compressible effects of the liquid [121].

We assume that the liquid surrounding the bubble is inviscid, incompressible, and the liquid flow is irrotational. The fluid velocity $\boldsymbol{u}$ thus has a potential φ, $\boldsymbol{u} = \nabla\varphi$ which satisfies Laplace's equation, $\nabla^2\varphi = 0$. Using Green's second identity the potential φ may be represented as a surface integral over the bubble surface S_b as follows,

$$c(\boldsymbol{r})\varphi(\boldsymbol{r}) = \int_{S_b} \left(\frac{\partial\varphi(\boldsymbol{q})}{\partial n} G(\boldsymbol{r},\boldsymbol{q}) - \varphi(\boldsymbol{q}) \frac{\partial G(\boldsymbol{r},\boldsymbol{q})}{\partial n} \right) dS(\boldsymbol{q}), \tag{2.1.3}$$

where $\boldsymbol{r}$ is the field point and $\boldsymbol{q}$ is the source point, $c(\boldsymbol{r})$ is the solid angle and $\boldsymbol{n}$ is the unit outward normal of the bubble surface S_b.

To satisfy the impermeable boundary condition on the wall, the Green function is given as follows,

$$G(\boldsymbol{r},\boldsymbol{q}) = \frac{1}{|\boldsymbol{r}-\boldsymbol{q}|} + \frac{1}{|\boldsymbol{r}-\acute{\boldsymbol{q}}|}, \tag{2.1.4}$$

where $\acute{\boldsymbol{q}}$ is the image of $\boldsymbol{q}$ reflected to the wall.

The kinematic and dynamic boundary conditions on the bubble surface S_b are as follows,

$$\frac{d\boldsymbol{r}}{dt} = \nabla\varphi \quad \text{on} \quad S_b, \tag{2.1.5}$$

$$p_L = p_b - 2\sigma\nabla\cdot\boldsymbol{n} \quad \text{on} \quad S_b, \tag{2.1.6}$$

where p_L is the liquid pressure on the bubble surface S_b, σ is the surface tension coefficient, and $\nabla\cdot\boldsymbol{n}$ is the mean curvature of the bubble surface. Equation (2.1.6) can be written in terms of the velocity potential φ using Bernoulli's equation,

$$\begin{aligned} \frac{d\varphi}{dt} &= \frac{p_0 + p_a\sin(kx-\omega t+\phi_0) + 2\sigma\nabla\cdot\boldsymbol{n}}{\rho} \\ &+ \frac{1}{2}|\nabla\varphi|^2 - \frac{1}{\rho}\left(p_v + p_{g0}\left(\frac{V_0}{V}\right)^{\lambda} \right) \quad \text{on} \quad S_b. \end{aligned} \tag{2.1.7}$$

We choose the reference length R_0 (initial radius of the bubble) and the reference pressure $\Delta p = p_0 - p_v$ and introduce the following asterisk (*) for the dimensionless variables,

$$\boldsymbol{r}_* = \frac{\boldsymbol{r}}{R_0}, \tag{2.1.8a}$$

$$t_* = \frac{t}{R_0}\sqrt{\frac{\Delta p}{\rho}}, \tag{2.1.8b}$$

$$\varphi_* = \frac{\varphi}{R_0}\sqrt{\frac{\rho}{\Delta p}}, \tag{2.1.8c}$$

$$\varepsilon = \frac{p_{g0}}{\Delta p}, \tag{2.1.8d}$$

$$\sigma_* = \frac{\sigma}{R_0 \Delta p}, \tag{2.1.8e}$$

$$p_{a*} = \frac{p_a}{\Delta p}, \tag{2.1.8f}$$

$$\omega_* = \omega R_0 \sqrt{\frac{\rho}{\Delta p}}, \tag{2.1.8g}$$

$$k_* = R_0 k. \tag{2.1.8h}$$

The dimensionless dynamic boundary condition on the bubble surface is,

$$\frac{d\varphi_*}{dt_*} = 1 + p_{a*}\sin(k_* x_* - \omega_* t_* + \phi_0) + 2\sigma_* \nabla \cdot \boldsymbol{n} + \frac{1}{2}\left|\nabla \varphi_*\right|^2 - \varepsilon \left(\frac{V_0}{V}\right)^{\kappa} \text{ on } S_b. \tag{2.1.9}$$

However, the standoff distance normalized with respect to the maximum equivalent bubble radius following the convention,

$$\gamma = \frac{s}{R_{\max}}, \tag{2.1.10}$$

where s is the distance between the wall and the bubble centre at inception, $R_{\max}$ is the

maximum radius a bubble initially in equilibrium would attain in an infinite ambient fluid subject to the imposed ultrasound.

We assume that both the bubble and liquid are initially motionless and the bubble is assumed in equilibrium with a constant far field pressure p_0. This requires the following balance pressure,

$$p_L|_{t=0} = p_0 = p_b|_{t=0} - 2\sigma\nabla \cdot \boldsymbol{n}, \tag{2.1.11}$$

where $p_b|_{t=0} = p_v + p_{g0}$ and with the dimensionless form obtained using (2.1.8d) and (2.1.8e),

$$\varepsilon = 1 + 2\sigma_* \tag{2.1.12}$$

2.2 Numerical modeling

The numerical model is based on the BIM using planer triangular elements. The initial mesh of the bubble surface is generated from an icosahedron shape by dividing each triangle into smaller equilateral triangles and projecting the new vertices on the bubble surface [116]. The integration in (2.1.3) can be expressed as the summation of the integrations over all the boundary elements. On each element, linear interpolations are used for the potential φ and normal velocity $\psi = \partial\varphi/\partial n$. The diagonal elements of the influence coefficient matrices are integrated analytically and the non-diagonal elements are calculated numerically using the Gaussian quadrature [116].

2.2.1 Bubble surface interpolation

The normal $\boldsymbol{N}_0$ at a node $\boldsymbol{r}_i$ can be approximated by a weighted average of the unit normals $\boldsymbol{n}_k^e$ of its surrounding elements, as shown in figure 2.2,

$$\boldsymbol{N}_0 = \sum_{k=1}^{M_s} w_k \boldsymbol{n}_k^e, \tag{2.2.1}$$

where M_s is the number of the surrounding triangles to the node $\boldsymbol{r}_i$, and w_k is the weighted coefficient for each of the elements. The normal $\boldsymbol{n}_k^e$ of each surrounding element can be regarded as the approximate normal of the surface at the element centre $\boldsymbol{r}_k^e$. The weighted coefficient w_k thus should decrease with the distance between $\boldsymbol{r}_i$ and $\boldsymbol{r}_k^e$. In this work, w_k is chosen to decrease exponentially with the distance,

$$w_k = \exp\left(-\frac{|\boldsymbol{r}_k^e - \boldsymbol{r}_i|}{2d}\right), \tag{2.2.2}$$

where d is the average distance from the surrounding nodes to the node $\boldsymbol{r}_i$.

Thus, the initial unit normal is,

$$\boldsymbol{n}_0 = \frac{\boldsymbol{N}_0}{|\boldsymbol{N}_0|} \tag{2.2.3}$$

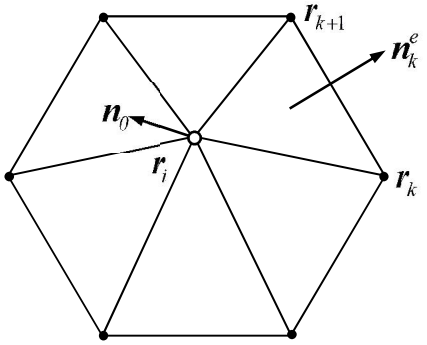

Figure 2.2: Sketch of the surrounding elements to the node $\boldsymbol{r}_i$.

The bubble surface is interpolated using a moving least square method following Zhang et al. [135] and Wang [118]. A local Cartesian coordinate system, $O-XYZ$, is introduced, with its origin O at the point considered, and its Z-axis along the normal direction $\boldsymbol{n}_0$. A second order polynomial is implemented for the bubble surface as follows,

$$Z = F(X,Y) = a_1 + a_2X + a_3Y + a_4XY + a_5X^2 + a_6Y^2 \tag{2.2.4}$$

The coefficients, a_j, j=1, 2, $\cdots$, 6, are determined from the nearest neighboring nodes within $2d$ from the node considered. Denote the nearest neighbouring nodes as (X_k, Y_k, Z_k), k=1, 2, $\cdots$, N_b, where N_b is the number of the neighbouring nodes. The error function Φ associated with the moving least-squares method is defined as,

$$\Phi(a_1,a_2,a_3,a_4,a_5,a_6) = \sum_{k=1}^{N_b} w_k \left[F(X_k,Y_k) - Z_k\right]^2 . \tag{2.2.5}$$

The coefficients a_j are determined by setting the derivative of Φ in a_j to be zero to minimize the error function,

$$\frac{\partial \Phi}{\partial a_j} = 0 \text{ for } j = 1,2,\cdots,6, \tag{2.2.6}$$

Substituting ((2.2.4) and (2.2.5)) into (2.2.6) yields

$$\sum_{j=1}^{6} A_{ij}a_j = B_i \text{ for } i = 1,2,\cdots,6, \tag{2.2.7}$$

where A_{ij} and B_i are given in terms of w_k and $(X_k,\, Y_k,\, Z_k)$,

$$A_{ij} = \sum_{k=1}^{N_b} w_k B_{kj} B_{ki}, \tag{2.2.8a}$$

$$B_i = \sum_{k=1}^{N_b} w_k Z_k B_{ki}, \tag{2.2.8b}$$

$$\begin{aligned} B_{k1} = 1,\ B_{k2} = X_k,\ B_{k3} = Y_k, \\ B_{k4} = X_k^2,\ B_{k5} = X_k Y_k,\ B_{k6} = Y_k^2. \end{aligned} \quad \text{for} \quad k = 1, 2, \cdots, N_b. \tag{2.2.8c}$$

A more accurate normal is further obtained as follows with the second order interpolation (2.2.4),

$$\boldsymbol{n} = \frac{\nabla f}{|\nabla f|} = \mp \frac{(a_2, a_3, -1)}{\sqrt{a_2^2 + a_3^2 + 1}}, \tag{2.2.9}$$

where the sign is chosen such that $\boldsymbol{n} \cdot \boldsymbol{n}_0 > 0$, where $\boldsymbol{n}_0$ is the approximate normal at $\boldsymbol{r}_i$ calculated from (2.2.3).

The mean curvature for the implicit surface $f(X, Y, Z) = F(X, Y) - Z = 0$ is given as,

$$\begin{aligned} \nabla \cdot \boldsymbol{n} &= \frac{\nabla f \times H(f) \times (\nabla f)^T - |\nabla f|^2 \, Trace(H)}{2 \, |\nabla f|^3} \\ &= -\frac{a_5 + a_6 + a_6 a_2^2 + a_5 a_3^2 - a_2 a_3 a_4}{(1 + a_2^2 + a_3^2)^{3/2}}, \end{aligned} \tag{2.2.10}$$

where $H(f) = \nabla(\nabla f)$ is the Hessian matrix of f and $Trace(H)$ is the summation of its diagonal elements [43]. The above interpolation scheme works for the potential distribution on the bubble surface too, except that Z_k in (2.2.5) and (2.2.8b) should be replaced by the potential φ_k at the node $(X_k,\, Y_k,\, Z_k)$. Denote the interpolation for the potential as follows,

$$\varphi(X, Y) = b_1 + b_2 X + b_3 Y + b_4 XY + b_5 X^2 + b_6 Y^2, \tag{2.2.11}$$

the tangential velocity $\boldsymbol{v}_\tau$ on the bubble surface can be calculated using the following formula,

$$\boldsymbol{v}_\tau = b_2 \nabla X(x, y, z) + b_3 \nabla Y(x, y, z), \tag{2.2.12}$$

where $X(x, y, z)$ and $Y(x, y, z)$ are determined from the transform from the coordinates (x, y, z) to the local coordinates (X, Y, Z).

2.2.2 Lagrangian time integration

Assume the bubble shape and the potential distribution on it are known at time t. The normal velocity can be obtained by solving (2.1.3) using the BIM. The tangential velocity is obtained from (2.2.12). The bubble surface and the potential distribution at the next time step $t + \Delta t$ are obtained by integrating the kinematic and dynamic boundary conditions (2.1.5, 2.1.9), respectively. The numerical integrations are performed using the fourth-order Runge-Kutta scheme (RK4) , which has demonstrated greater stability than lower order schemes. A varied time-step size Δt_* is chosen as follows to save the CPU time,

$$\Delta t_* = \frac{\Delta \varphi_*}{\max \left| 1 + p_{a*} \sin(k_* x_* - \omega t_* + \phi_0) + 2\sigma_* \nabla \cdot \boldsymbol{n} + \frac{1}{2} |\nabla \varphi|^2 - \varepsilon \left(\frac{V_0}{V} \right)^\kappa \right|} \tag{2.2.13}$$

where $\Delta \varphi_*$ is some constant, the maximum is taken over all nodes on the bubble surface. With this choice of Δt_*, the changes in potential at all nodes is bounded above by the prescribed value $\Delta \varphi_*$.

2.2.3 Elastic mesh technique for improving mesh quality

In the Lagrangian approach, the nodes on the bubble surface are updated with the material velocities at the nodes. This may result in a poor quality mesh for a non-spherical bubble motion at a large amplitude. Figure 2.3a provides the computational result using the

Lagrangian approach for a bubble surface for a typical case, when the bubble jet is developing. Numerical instabilities occur over the jet surface due to the distorted mesh. This case is for an ultrasound bubble in an infinite liquid, to be chosen as water in the calculations in this study, in which the speed of sound is 1500 m s^{-1}. The initial radius for the bubble is $R_0 = 4.5$ μm, the amplitude and frequency of the ultrasound are $p_{a*} = 1.6$, $f = 300$ kHz. The bubble surface is discretized into $M = 980$ triangular elements with $\Delta\varphi_*$= 0.002 used in (2.2.13) for setting time-step. In all cases considered in this chapter, the parameters for the liquid and gas are chosen as $\kappa = 1.667$, $\sigma = 0.073$ N m^{-1}, $p_0 =$ 101.3 kPa, $p_v = 0.023p_0$ and $\rho = 999$ kg m^{-3}.

Wang et al.[113, 112] developed an elastic mesh technique (EMT) for improving the mesh quality for the simulation of bubble dynamics. It is assumed in the EMT that each segment of a surface mesh is an elastic ribbon and the optimum mesh is found by minimizing the total elastic energy stored in all segments of the mesh. In this approach, a mesh node at time t is updated with the normal velocity at the node plus an artificial tangential velocity, since the bubble surface at the next time $t + \Delta t$ is only determined by the normal velocity distribution on the bubble surface. The artificial tangential velocity is obtained by the requirement of minimizing the total elastic energy.

The elastic force f_e associated with a segment is a function of the segment length l, i.e., the constitutive relation of a segment is defined as follows,

$$f_e = f_e(l). \tag{2.2.14}$$

In this thesis we use $f_e(l) = k_e l^3$, where k_e is the elasticity coefficient. The coefficient k_e will be eliminated in the model subsequently in (2.2.19) and its value does not affect the computational results.

The elastic energy E_{mesh} stored in the mesh at the new time step $t + \Delta t$ is,

$$E_{\text{mesh}} = \sum_{i=1}^{N} \sum_{j=1}^{M_i} \int_0^{l_{ij}} f_e(l) dl, \tag{2.2.15}$$

where the summation is taken over all segments of the mesh, M_i is the number of the surrounding nodes to the node i, N is the total node number of the mesh, and l_{ij} is the segment length between the two nodes $\boldsymbol{r}_i^{new}$ and $\boldsymbol{r}_j^{new}$ at the next time step $t + \Delta t$, i.e.

$$l_{ij} = \left| \boldsymbol{r}_i^{new} - \boldsymbol{r}_j^{new} \right| = \left| \boldsymbol{r}_i - \boldsymbol{r}_j + \Delta t (\boldsymbol{u}_i - \boldsymbol{u}_j) \right|, \tag{2.2.16}$$

where $\boldsymbol{u}_i$ and $\boldsymbol{u}_j$ are velocities at the nodes i and j respectively.

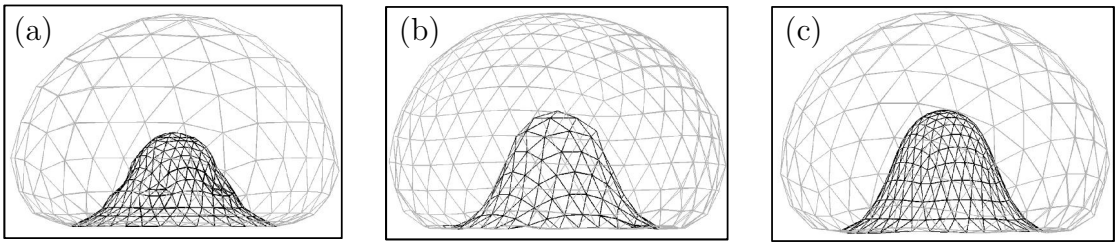

Figure 2.3: The comparison of the meshes of the bubble surface at $t_* = 5.51$ using (a) the Lagrangian approach, (b) the EMT and (c) the hybrid approach. The parameters used are $R_0 = 4.5$ μm, $p_{a*} = 1.6$, $f = 300$ kHz, $M = 980$, $\Delta\varphi_* = 0.002$, $\kappa = 1.667$, $\sigma = 0.073$ N/m, $p_0 = 101.3$ kPa, $p_v = 0.023$ p_0 and $\rho = 999$ kg/m^3.

The optimum mesh can be obtained by minimizing the elastic energy E_{mesh}, therefore the derivative of E_{mesh} with respect to $\boldsymbol{u}_i = (u_i, v_i, w_i)$ must be zero,

$$\frac{\partial E_{\text{mesh}}}{\partial u_i} = 0, \ \frac{\partial E_{\text{mesh}}}{\partial v_i} = 0, \ \frac{\partial E_{\text{mesh}}}{\partial w_i} = 0. \tag{2.2.17}$$

Substituting 2.2.15 into equation 2.2.17 results in

$$\sum_{j=1}^{M_i} \left(f_e\left(l_{ij}\right) \frac{l_{ij}}{|l_{ij}|} \right) = 0, \tag{2.2.18}$$

The following iterative scheme is employed to solve (2.2.17),

$$\boldsymbol{u}_i^{n+1} = \psi_i \boldsymbol{n}_i + P \left(\frac{\left(\sum_{j=1}^{M_i} f(l_{ij}^n) \left(\boldsymbol{r}_j - \boldsymbol{r}_i + \Delta t \boldsymbol{u}_j^n \right) / l_{ij}^n \right)}{\Delta t \sum_{j=1}^{M_i} f(l_{ij}^n)/l_{ij}^n} \right), \tag{2.2.19}$$

where $\boldsymbol{u}_i^n$ is the n^{th} iteration of the prescribed velocity at node i, $P(\boldsymbol{v})$ stands for the tangent component of a vector $\boldsymbol{v}$, i.e.

$$P(\boldsymbol{v}) = \boldsymbol{v} - \left(\boldsymbol{v} \cdot \boldsymbol{n}_i .\right) \boldsymbol{n}_i. \tag{2.2.20}$$

The optimum prescribed velocity $\boldsymbol{u}_i^{emt}$ for the EMT is obtained by solving (2.2.19) using iteration. The bubble surface and potential distribution on it are then updated as follows,

$$\frac{\delta \boldsymbol{r}}{\delta t} = \boldsymbol{u}_i^{emt} \tag{2.2.21a}$$

$$\frac{\delta \varphi}{\delta t} = \frac{\partial \varphi}{\partial t} + \boldsymbol{u}_i^{emt} \cdot \nabla \varphi = \left(\boldsymbol{u}_i^{emt} - \boldsymbol{u}_i \right) \cdot \nabla \varphi + \frac{d\varphi}{dt}. \tag{2.2.21b}$$

Figure 2.3b shows the bubble surface calculated using the EMT, which avoids the numerical instabilities occurred in the Lagrangian approach shown in figure 2.3a.

2.2.4 Hybrid approach for improving mesh quality

In the EMT the mesh sizes on the bubble surface tends to be uniform but a non-uniform mesh is more suitable for a bubble surface with a varying curvature. A finer mesh should be used for the part of the bubble surface where the curvature radius is small, such as around the jet surface. We implement a hybrid-approach of the Lagrangian and EMT approaches as follows,

$$\boldsymbol{u}_i^{hybrid} = W\,\boldsymbol{u}_i + (1-W)\boldsymbol{u}_i^{emt},\ W \in [0,1], \tag{2.2.22}$$

where W was chosen based on the numerical tests as 0.7, which worked well for all the cases in this thesis. Figure 2.3c shows the bubble mesh of the hybrid approach, where the jet surface is smoother and with finer mesh than the EMT (figure 2.3b). The EMT and the hybrid approach were applied once every 10 time steps.

2.3 Validations of the numerical model

2.3.1 Comparisons with the Rayleigh-Plesset equation

The case considered is for the radial oscillation of a spherical bubble with an initial radius of $R_0 = 4.5$ μm and an initial pressure of $\varepsilon = 20.0$ in an otherwise quiescent infinite liquid. The bubble surface is discretized into $M = 500$ triangular elements with $\Delta\varphi_* = 0.01$ used in (2.2.13) for setting time-step. The rest of the parameters are the same as in the case shown in figure (2.3).

In this case the initial bubble pressure is larger than the constant ambient pressure, the bubble starts expanding and oscillates subsequently. Figure 2.4 compares the BIM computational results with the Rayleigh-Plesset equation (RPE) for the bubble radius

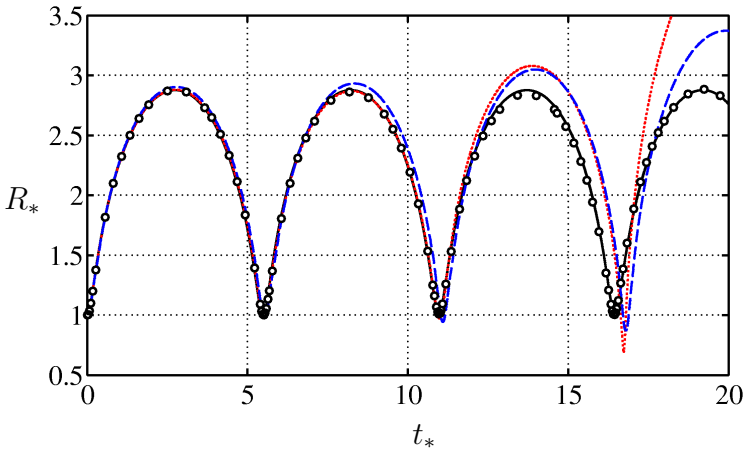

Figure 2.4: Comparison of the bubble radius history of the RPE (solid line) with the BIM model using: (i) the RK4 coupled with the weighted average method (dotted line), (ii) the Euler method coupled with the polynomial interpolations (dashed line), and (iii) the RK4 coupled with the polynomial interpolations (circle marks). The parameters used are $R_0 = 4.5\ \mu\text{m}, \varepsilon = 20, p_{a*} = 0, M = 500$, and the other parameters being the same as in figure 2.3.

history. The results of three different computations are shown: (i) the RK4 for updating the bubble surface and the weighted average method for calculating the tangential velocity on the bubble surface [117] , (ii) the Euler method for updating the bubble surface and the polynomial interpolations as described in Section 2.2.1 for calculating the curvature and tangential velocity on the bubble surface, and (iii) the RK4 coupled with the polynomial interpolations. All three options provided reasonable results for the first two cycles of oscillation but only option (iii) provided a good result for the third cycle of oscillation. The RK4 coupled with the polynomial interpolations was thus used in this thesis.

2.3.2 Comparison with an axisymmetric BIM model

We compare the present 3D BIM model with the axisymmetric BIM model by Calvisi et al. [13] for the case shown in figure 2.3. The results of the 3D model are provided with three options for advancing the bubble shape and the potential distribution on it by using (a) the Lagrangian approach, (b) the EMT method and (c) the hybrid approach.

Figure 2.5 shows the bubble shapes at the end of the collapse phase, when a sharp jet forms in the wave direction. The three-dimensional results of all the three options agree with the axisymmetric model, in terms of the bubble shape, jet shape and location. In the Lagrangian approach (figure 2.5a), some numerical instabilities developed around the jet surface. In the EMT (figure 2.5b), the mesh is not fine enough at the jet surface. The hybrid approach is stable, generating a smooth jet surface with a fine mesh over there, and agrees best with the axisymmetric model (figure 2.5c).

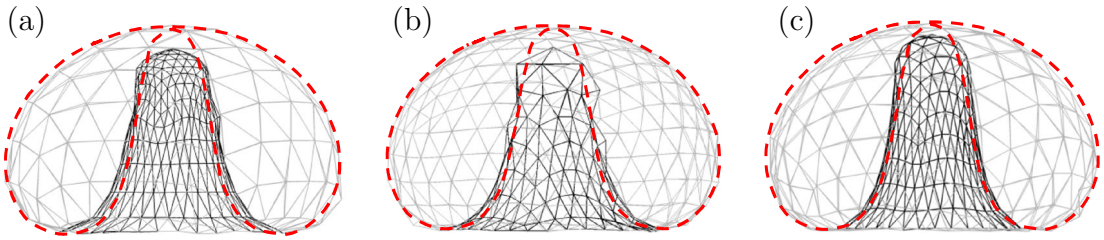

Figure 2.5: The bubble shapes at the end of the collapse phase at $t_* = 5.53$ for the case shown in figure 2.3 using (a) the Lagrangian approach, (b) the EMT method and (c) the hybrid approach, compared to the axisymmetric model (dashed line, Calvisi et al. [17])

2.3.3 Convergence to mesh size

We have performed the convergence test of the numerical model for the case shown in figure 2.3 at various numbers of surface elements, $M = 1280$, 1620 and 2000, respectively. The bubble shapes at the end of the collapse phase are shown in figure 2.6, compared with the corresponding axisymmetric result [13]. As the mesh size reduces, the 3D results approach well to the axisymmetric result and the jet becomes sharper. The 3D results are convergent to the mesh size and approaches to the axisymmetric result. The small discrepancy between the two models is because the mesh size used in the 3D model is larger than that in the axisymmetric model.

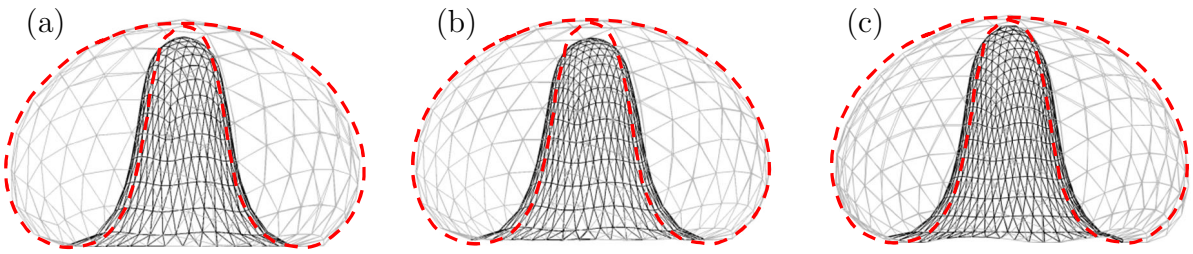

Figure 2.6: The bubble shapes at the end of the collapse phase $t_* = 5.53$ with various numbers of surface elements for the case shown in figure 2.3: (a) M=1280, (b) M=1620 and (c) M=2000, compared to the axisymmetric model (dashed line, Calvisi et al. [13])

2.3.4 Evaluation of the hybrid elastic mesh technique

To examine the hybrid EMT, we will compare the volume and Kelvin impulse of the bubble calculated with and without using the technique. The Kelvin impulse of the bubble was introduced by Benjamin and Ellis [1], which is defined as the surface integral of the potential φ on the bubble surface S_b,

$$\boldsymbol{I}_{K*} = \int_{S_b} \boldsymbol{n}\ \varphi_*\ dS. \tag{2.3.1}$$

The Kelvin impulse $\boldsymbol{I}_{K*}$ gives an indication of the degree of asymmetry of the bubble's motion, which often has the same directions of the jet and the bubble migration [121, 124, 125, 116, 117].

The case considered is for bubble dynamics near a wall subjected to ultrasound propagating parallel to the wall at γ= 3.75, with the rest of the parameters being the same as in the case shown in figure 2.3. In this case the bubble is with three dimensional deformations as to be shown in figure 2.8 in the next section.

If we compare two simulations with and without the hybrid EMT respectively, the results of the latter are affected by the poor mesh after bubble jetting as shown in figure 2.5. We will apply the hybrid EMT once every 10 time steps and we compare the results before

t_*	E_V	E_{θ_K}	E_{IK}
4.12	0.0002	0.0000°	0.0000
5.56	0.0018	0.0011°	0.0002
5.58	0.0024	0.0070°	0.0023

Table 2.1: The comparison of the results before and after using the hybrid EMT at three typical times in terms of the relative error of the bubble volume E_V, the error for the direction $E_{\theta K}$ of the Kelvin impulse, and the relative error for the amplitude E_{IK} of the Kelvin impulse for a bubble near a wall subjected to ultrasound propagating parallel to the wall at $\gamma = 3.75$, with the rest of the parameters being the same as in the case shown in figure 2.3.

and after using the hybrid EMT at a specific time. Three typical times are chosen for the comparison (a) at the maximum volume when the bubble is approximately spherical, (b) at the start of bubble jetting, and (c) just before jet impact, respectively. Table 2.1 shows the comparison at the three times in terms of the relative error of the bubble volume E_V, the error for the direction $E_{\theta K}$ of the Kelvin impulse, and the relative error for amplitude E_{IK} of the Kelvin impulse. The changes due to the hybrid EMT are very small and increase with the deformation of the bubble from a spherical shape.

2.4 Numerical results and discussions

2.4.1 Effects of standoff distance γ

In this section, we perform the numerical studies of microbubble dynamics near a rigid wall subjected to ultrasound propagating parallel to the wall. To study effects of the standoff distance of the bubble from the wall, we consider three cases at $\gamma = 0.75$, 3.75 and 11.25, respectively, with the rest of the parameters kept the same as in figure 2.3.

The bubble shapes at $\gamma = 0.75$ at typical times is shown in figure 2.7. The bubble expands from figures 2.7a to 2.7b and collapses subsequently. The bottom of the bubble is flattened by the wall in the later stage of the expansion phase (figure 2.7b). The bubble elongates

vertically during the collapse phase (figures 2.7(c-e)), as a result that the bottom part of the bubble surface is attracted by the wall and the rest of the bubble surface collapses. At the final stage of the collapse phase, a wide high-speed liquid jet forms and is directed towards the wall (figures 2.7e, f). It takes about 1% of the bubble lifetime from the beginning of the jet formation to its impact on the opposite bubble surface, which is much faster than when under a constant normal ambient pressure. For the latter the jet development at γ=0.75 takes approximately 6% of its lifetime [126].

The bubble shapes at $\gamma = 3.75$ at typical times are shown in figure 2.8. The wall attraction on the bubble is weak compared with the previous case. The bubble expands and collapses spherically before a high-speed liquid jet develops rapidly towards the end of the collapse phase (figures 2.8c, d). The bubble is acted on by the Bjerknes force due to the ultrasound and the second Bjerknes force due to the wall, which are parallel and perpendicular to the wall respectively. They are comparable in amplitude in this case. As a result, the jet is at the bisector direction of the two forces, with the angle between the jet direction and the wall being about $-45°$.

The bubble dynamics at $\gamma = 11.25$ (figure 2.9) are similar to that at $\gamma = 3.75$ (figure 2.8). The bubble remains spherical for most of its lifetime before a high-speed jet develops rapidly at the end of the collapse phase. The jet development takes only 0.4% of the bubble lifetime in the two cases. The jet at $\gamma = 11.25$ is approximately in the direction of the ultrasound (figure 2.9d), since the effects of the wall in this case is negligible.

Figure 2.10 shows the bubble and jet shapes at the end of the collapse phase for the cases in the range of $0.75 \leq \gamma \leq 11.25$, with the rest of the parameters kept the same as in figure 2.3. The jet is directed towards the wall at γ=0.75 ($\theta_j \approx -88°$), rotates anticlockwise to the direction of the ultrasound with increasing γ as the bubble initiated further away from the wall, and is approximately along the direction of the ultrasound ($\theta_j \approx 4°$) at γ=11.25.

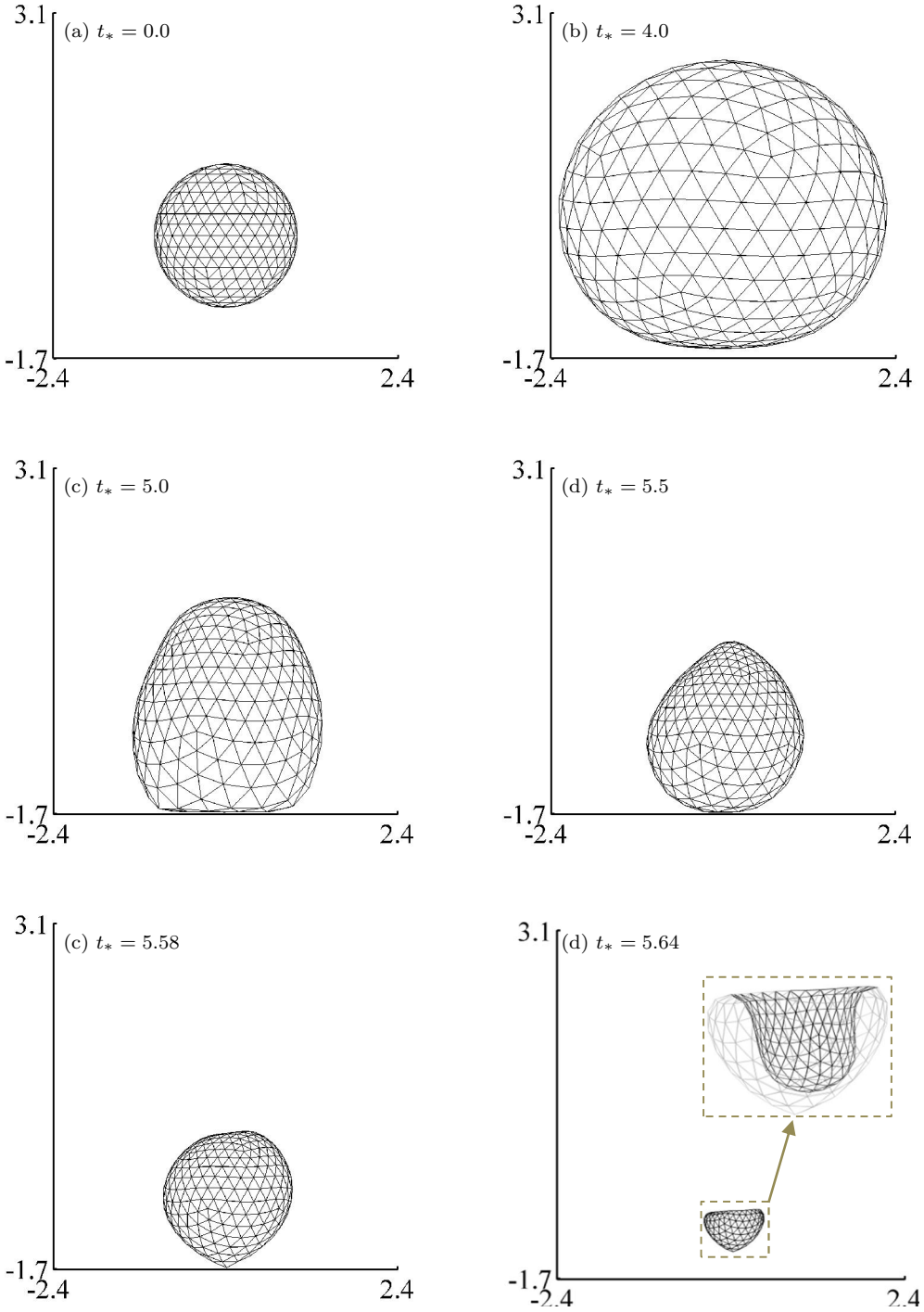

Figure 2.7: The bubble dynamics near a wall subjected to ultrasound propagating parallel to the wall at $\gamma = 0.75$, with the rest of the parameters being the same as in the case shown in figure 2.3. The bubble shapes are during the expansion phase (a-b) and collapse phase (b-f).

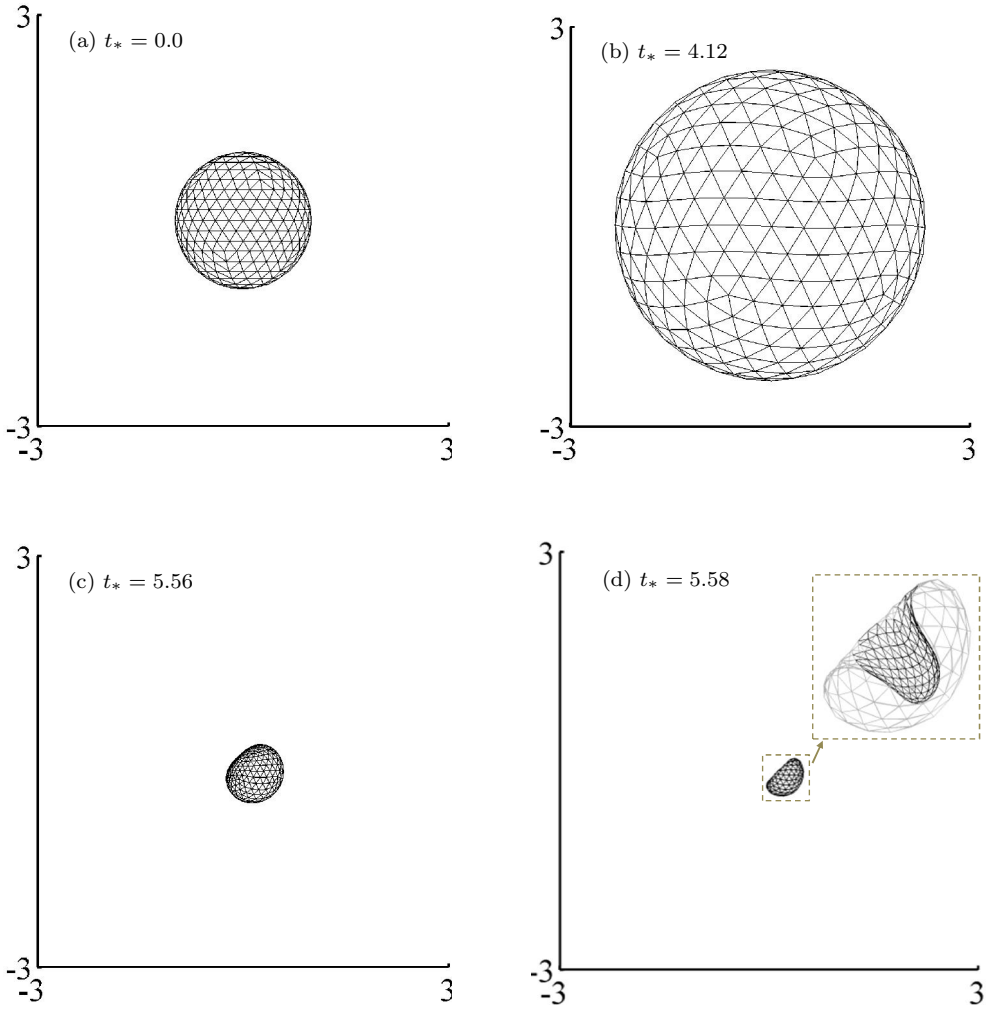

Figure 2.8: The bubble dynamics near a wall subjected to ultrasound propagating parallel to the wall at $\gamma = 3.75$, with the rest of the parameters being the same as in the case shown in figure 2.3. The bubble shapes are during the expansion phase (a-b) and collapse phase (b-d).

Note that as the jet is slightly asymmetric, its direction θ_j is estimated from the direction of its baseline, which is assumed being perpendicular to the jet. The jet width reduces apparently with the standoff distance γ.

Figure 2.11 depicts the bubble lifetime T_{c*} and the maximum equivalent radius $R_{\max*}$ versus the standoff distance γ for the cases shown in figure 2.10. As the bubble is initiated further away from the wall, its maximum volume increases while its lifetime decreases.

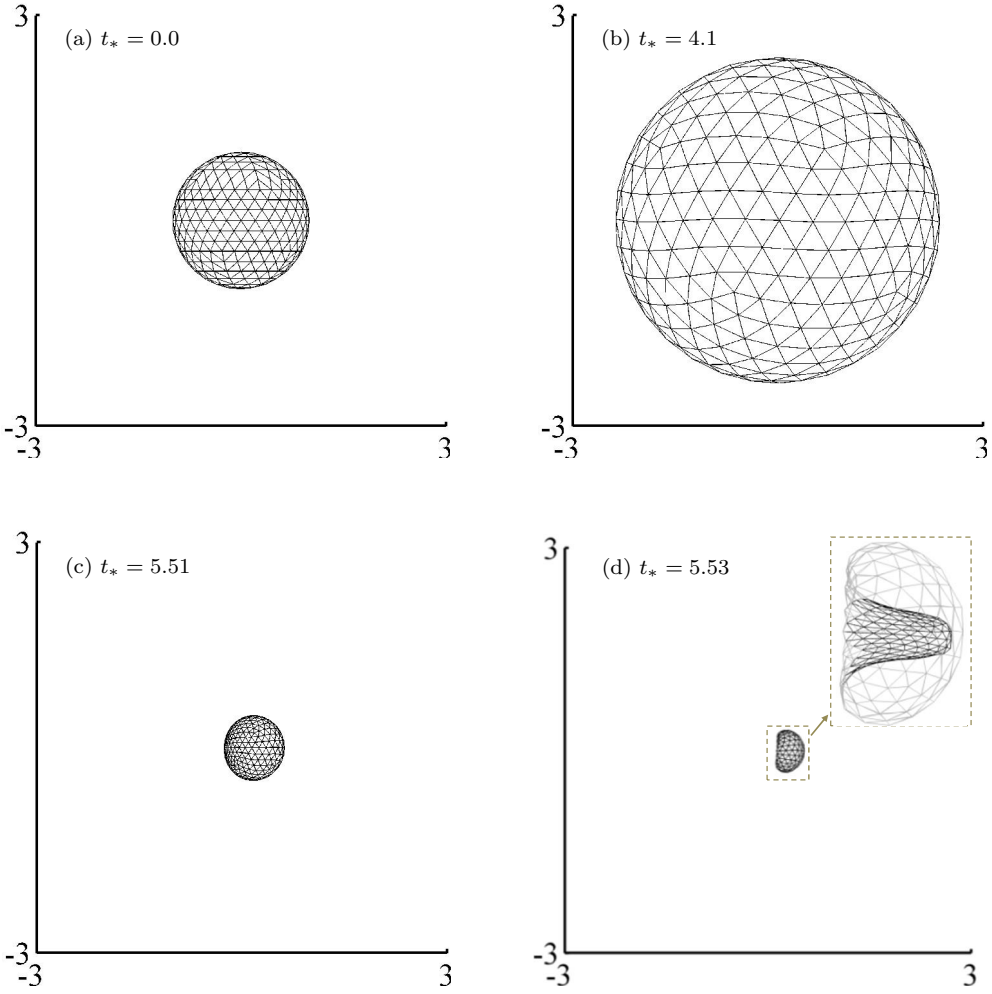

Figure 2.9: The bubble dynamics near a wall subjected to ultrasound propagating parallel to the wall at $\gamma = 11.25$, with the rest of the parameters being the same as in the case shown in figure 2.3. The bubble shapes are during the expansion phase (a-b) and collapse phase (b-d).

This is the same as that for bubble dynamics under a constant ambient pressure [66].

In figure 2.12 the direction θ_K of the Kelvin impulse is compared with the direction θ_j of the bubble jet and the direction $\theta_c = \tan^{-1}(z_c/x_c)$ of migration of the bubble centroid at the end of its lifetime. They are approximately equal for the cases considered. The Kelvin impulse can thus be used to estimate the directions for the bubble jet and bubble migration for acoustic bubble dynamics. This figure also shows that the magnitude I_{K*} of the Kelvin impulse reduces with the standoff distance of the bubble from the wall.

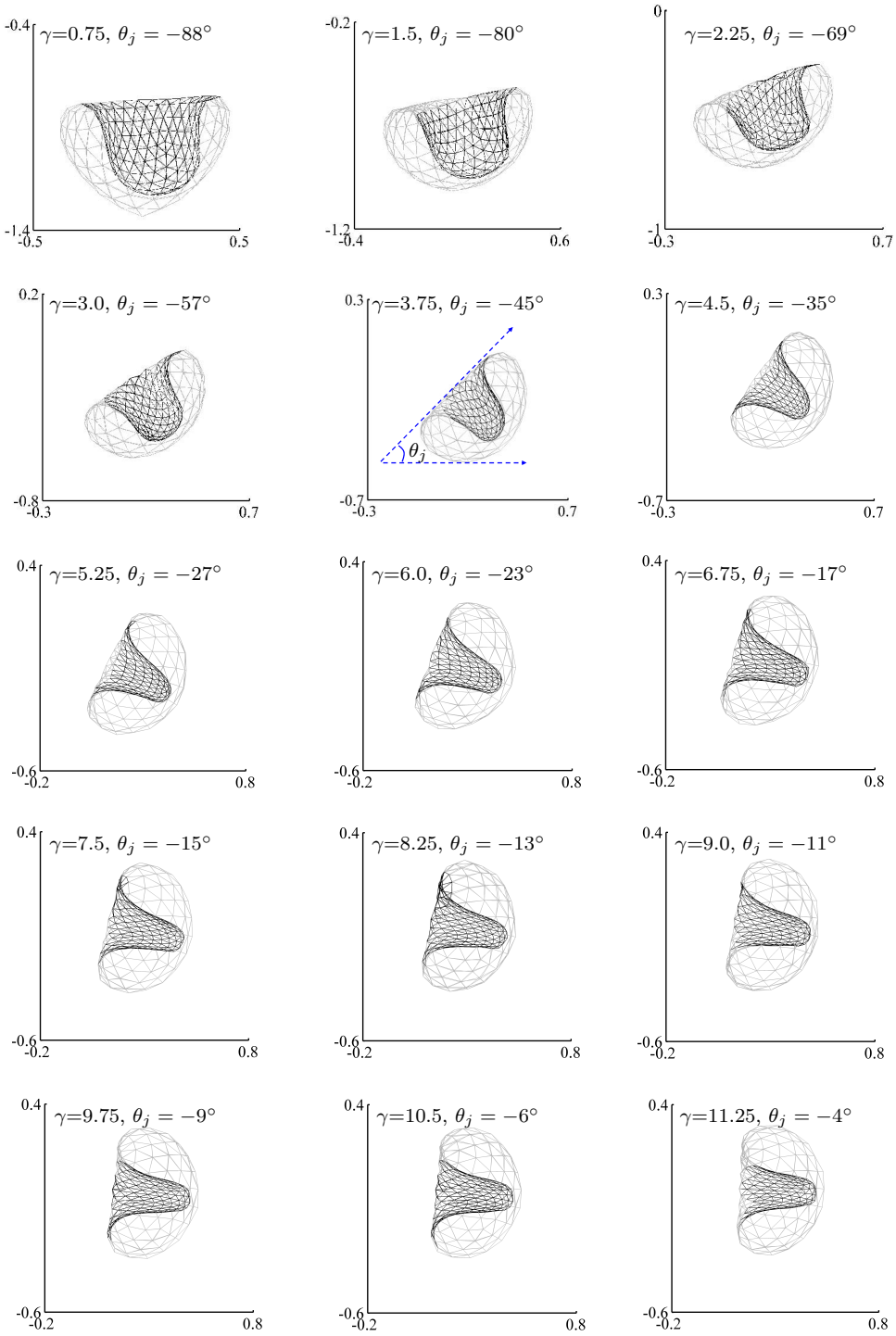

Figure 2.10: The jet direction at the end of the bubble lifetime at various standoff distances in the range of $0.75 \leq \gamma \leq 11.25$. The rest of the parameters are the same as in the case shown in figure 2.3.

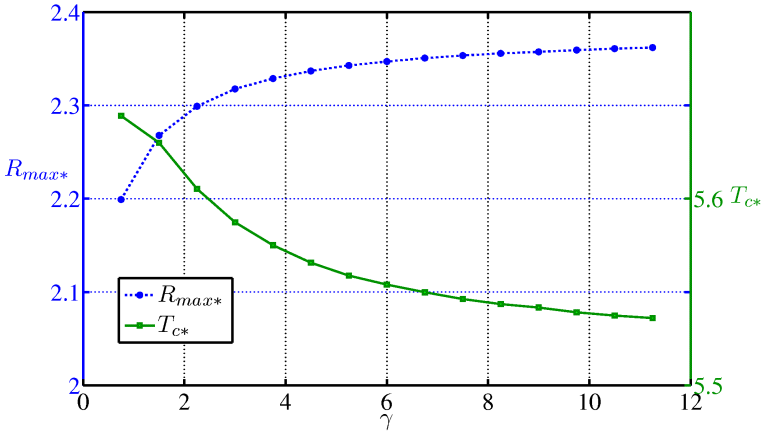

Figure 2.11: The bubble lifetime T_{c*} and maximum equivalent radius $R_{\max*}$ versus the standoff distance γ for the cases shown in figure 2.10.

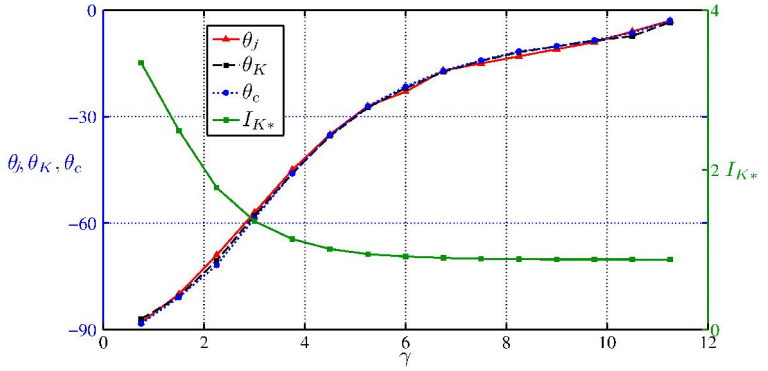

Figure 2.12: The direction θ_j of the bubble jet, the direction θ_c of migration the bubble centroid, the direction θ_K and the amplitude I_{K*} of the Kelvin impulse versus the standoff distance γ for the cases shown in figure 2.10.

2.4.2 Effects of the ultrasound amplitude

To consider the effects of the ultrasound amplitude, we repeat the cases at $\gamma = 0.75$, 3.75, 11.25 (figures 2.7, 2.8, 2.9) at various pressure amplitudes p_{a*} =1.5, 1.6, 1.7, 1.8, with the rest of the parameters kept as the same. The bubble and jet shapes at the end of the collapse phase for the cases are shown in figure 2.13. Table 2.2 provides the maximum equivalent bubble radius $R_{\max*}$, bubble lifetime T_{c*}, jet direction θ_j, direction θ_K and magnitude I_{K*} of the Kelvin impulse.

	$\gamma = 0.75$					$\gamma = 3.75$					$\gamma = 11.25$				
p_{a*}	$R_{\max*}$	T_{c*}	θ_j	θ_K	I_{K*}	$R_{\max*}$	T_{c*}	θ_j	θ_K	I_{K*}	$R_{\max*}$	T_{c*}	θ_j	θ_K	I_{K*}
1.5	2.08	5.53	$-88°$	$-87°$	2.7	2.20	5.50	$-47°$	$-48°$	0.82	2.23	5.41	$-3°$	$-2°$	0.64
1.6	2.20	5.65	$-88°$	$-87°$	3.34	2.33	5.58	$-45°$	$-46°$	1.13	2.37	5.53	$-4°$	$-3°$	0.88
1.7	2.32	5.75	$-86°$	$-86°$	3.83	2.46	5.70	$-45°$	$-44°$	1.40	2.50	5.65	$-4°$	$-3°$	1.12
1.8	2.44	5.85	$-85°$	$-86°$	4.02	2.60	5.80	$-43°$	$-43°$	1.70	2.65	5.76	$-3°$	$-3°$	1.40

Table 2.2: The maximum equivalent radius $R_{\max*}$, the bubble lifetime T_{c*}, the jet direction θ_j, the angle θ_K and amplitude I_{K*} of the Kelvin impulse at the end of the bubble lifetime for the cases shown in figure 2.13.

The jet direction does not change significantly with the ultrasound amplitude p_{a*}, as shown in figures 2.13 and table 2.2. This suggests that the Bjerknes force due to ultrasound and the second Bjerknes force due to the wall increase with the amplitude of ultrasound in a similar way. However, the jet width increases obviously with the ultrasound amplitude (figure 2.13). As shown in table 2.2, the maximum volume, the lifetime and the Kelvin impulse of the bubble all increase with the amplitude of ultrasound. The jet direction θ_j is approximately the same as the direction θ_K of the Kelvin impulse for all the cases considered.

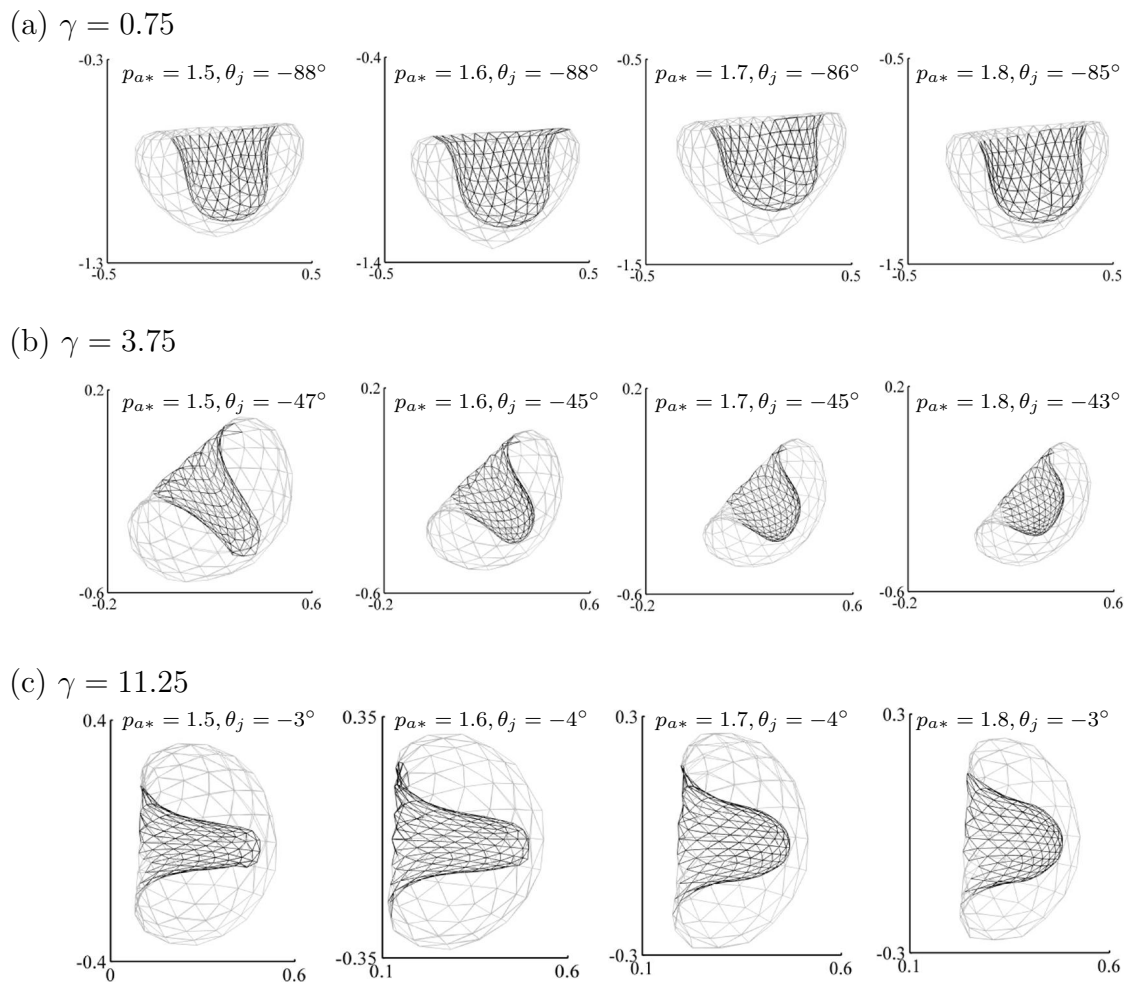

Figure 2.13: The bubble shapes at the end of the bubble lifetime at γ=0.75, 3.75, 11.25 and p_{a*}=1.5, 1.6, 1.7, 1.8, respectively. The rest of the parameters are the same as in the case shown in figure 2.3.

Figure 2.14 shows the histories of the bubble centroid x_{c*}, z_{c*} for the cases shown in figure 2.13. The bubble moves slightly in the contrary direction to the wave during the early expansion phase, moves in the direction of the wave since the later expansion phase and moves rapidly towards the end of the collapse phase. The migration along the wave direction increases as the bubble initiates further away from the wall.

The bubble moves away from the wall slightly during the expansion phase, moves back to the wall during the collapse phase and moves rapidly towards the end of the collapse

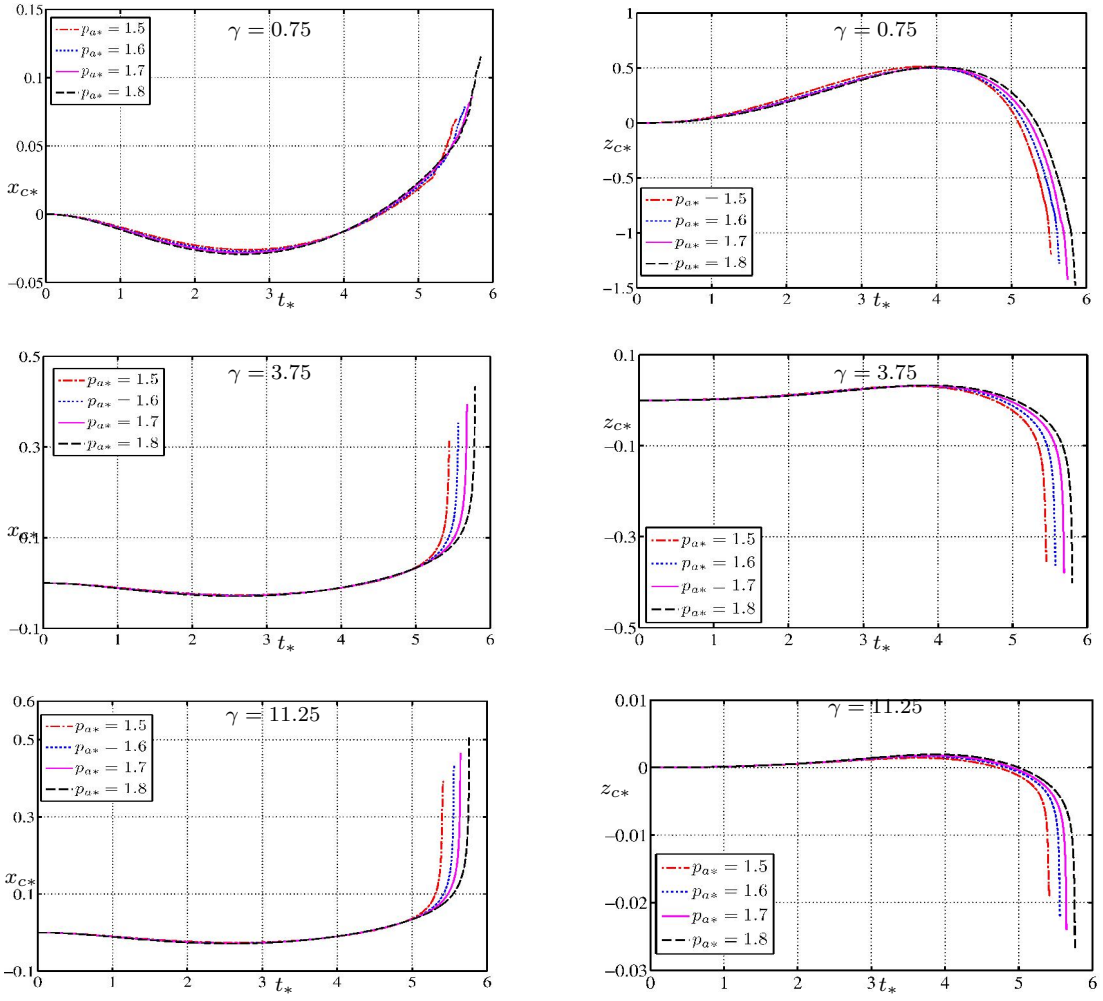

Figure 2.14: The histories of the bubble centroid x_{c*}, z_{c*} for the cases shown in figure 2.13.

phase. The migration towards the wall reduces as the bubble initiates further away from the wall. At $\gamma = 11.25$, the bubble only migrates along the wave direction. The migration of the bubble is not sensitive to the variation of the amplitude p_{a*} of ultrasound during a large part of its lifetime but increases significantly with the amplitude p_{a*} towards the end of the collapse phase along both the x- and z-axes. Since the bubble is made up of tetrahedron elements, then the bubble centroid can be calculated as,

$$\boldsymbol{r}_{c*} = (x_{c*}, y_{c*}, x_{c*}) = \frac{1}{V}\int_V \boldsymbol{r}_* \, dV \approx \frac{\sum \boldsymbol{r}_{i*} V_i}{\sum V_i}, \tag{2.4.1}$$

where V_i is the volume of each tetrahedron, $\boldsymbol{r}_{i*}$ denotes the centroid position vector of a certain tetrahedron say i. $\sum$ is the summation of all the tetrahedrons.

Figure 2.15 shows the speed history of the bubble surface at the position of the jet tip. It represents the bubble wall speed before the jet forms, which is low as compared to the jet velocity. The jet velocity rises rapidly towards the end of the collapse phase. The maximum jet velocity increases with the amplitude p_{a*} of the ultrasound, since the Berjeknes force due to the ultrasound increases with p_{a*}. The jet velocity also increases significantly with the standoff distance γ of the bubble from the wall.

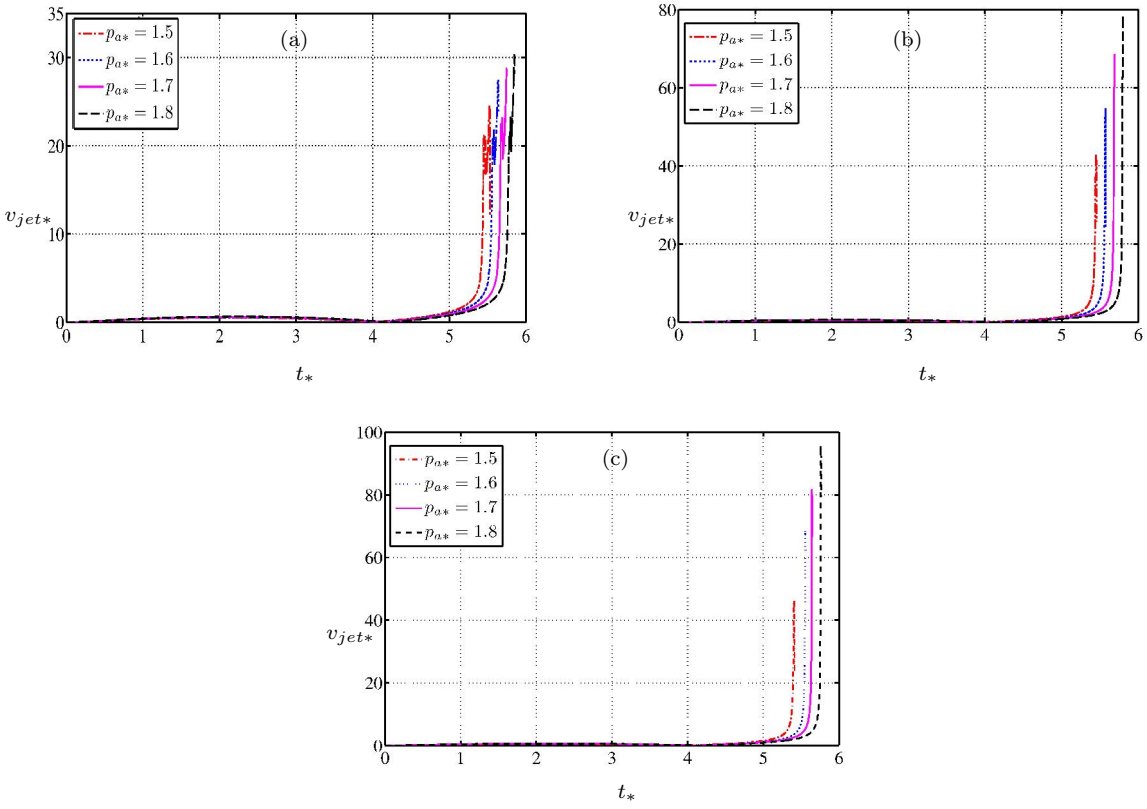

Figure 2.15: The histories of the jet velocity v_{jet*} at (a) γ=0.75, (b) γ=3.75 and (c) γ=11.25 resepectively for the cases shown in figure 2.13.

The jet velocity is about 250 m/s at $\gamma = 0.75$, p_{a*} =1.5 and 950 m/s at $\gamma = 11.25$, p_{a*}=1.8. The jet velocity of acoustic microbubbles observed here is significantly larger than the velocity of a boundary-induced jet of cavitation bubbles without the presence

of ultrasound. The latter is lower than 200 m/s at normal ambient pressure as reported from many experiments in the literature [65, 105, 109, 91, 74, 128]. Bubble jets due to ultrasound are difficult to observe, although bubble wall velocities exceeding 700 m/s were observed experimentally [80].

2.4.3 Effects of the initial bubble radius R_0

We examine the bubble behavior at $R_0 = 3.5$, 4.5, 5.5 μm and $\gamma = 3.75$ with the rest of the parameters being the same as in the case shown in figure 2.3. Figure 2.16 shows the bubble shapes at the end of collapse. The jet direction does not change significantly with the initial radius R_0, while the jet is sharper at a larger initial radius.

Figure 2.17 shows that the bubble at smaller initial radius reacts more strongly with the acoustic wave. Both the oscillation amplitude of the equivalent bubble radius and the maximum jet velocity increase inversely with bubble initial radius.

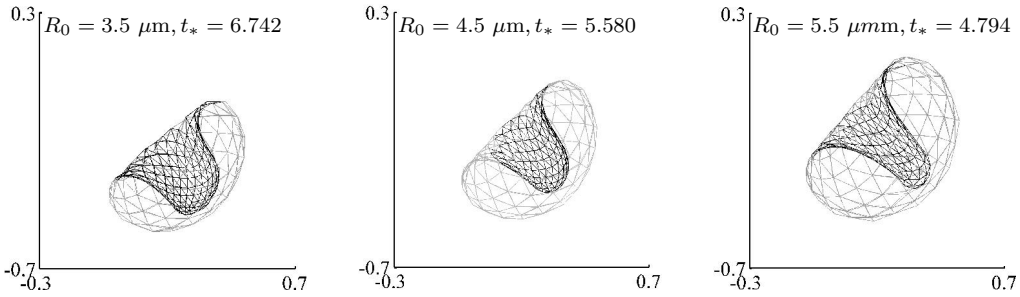

Figure 2.16: The bubble shapes at the end of the bubble lifetime at $\gamma = 3.75$, $R_0 = 3.5$, 4.5, 5.5 μm, and the rest of the parameters are the same as in the case shown in figure 2.3.

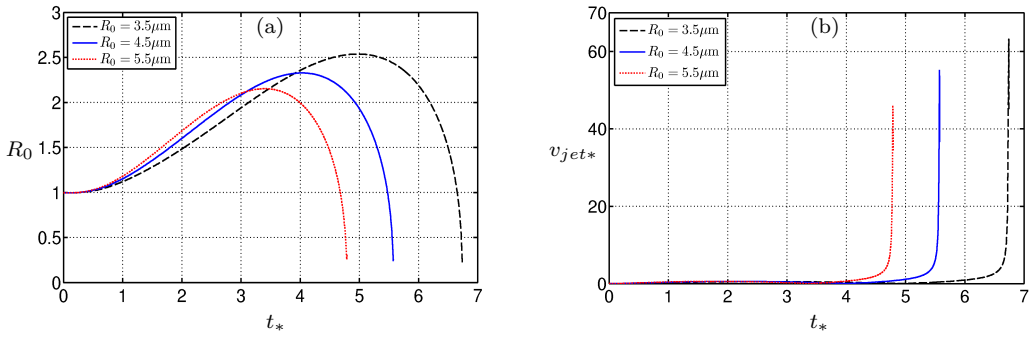

Figure 2.17: The bubble shapes at the end of the bubble lifetime at $\gamma = 3.75$, $R_0 = 3.5$, 4.5, 5.5 μm, and the rest of the parameters are the same as in the case shown in figure 2.3.

2.4.4 Effects of the wave frequency

Three different frequencies $f = 250$, 300, 350 kHz are considered at $\gamma = 3.75$ with the rest of the parameters are the same as in the case shown in figure 2.3. As shown in figure 2.18 the jet direction at the end of collapse doesn't change significantly with the frequency but the jet is sharper at a higher frequency. Figure 2.19 shows that the bubble reacts more weakly with the acoustic wave at a larger frequency; both the maximum dimensionless equivalent radius and the jet velocity reduce with the frequency.

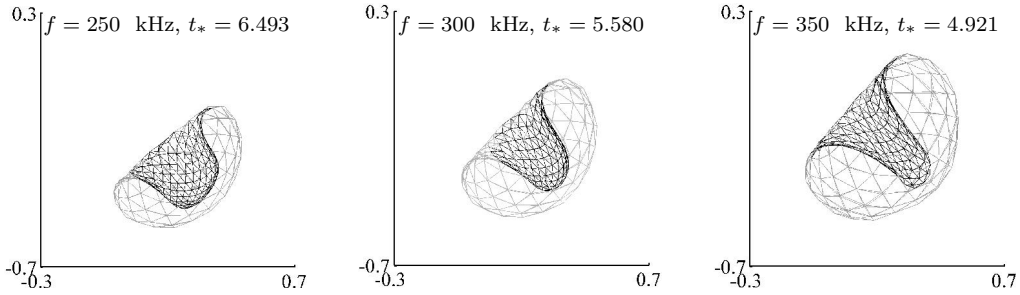

Figure 2.18: The bubble shapes at the end of the bubble lifetime at $\gamma = 3.75$, $f = 250$, 300, 350 kHz, and the rest of the parameters are the same as in the case shown in figure 2.3.

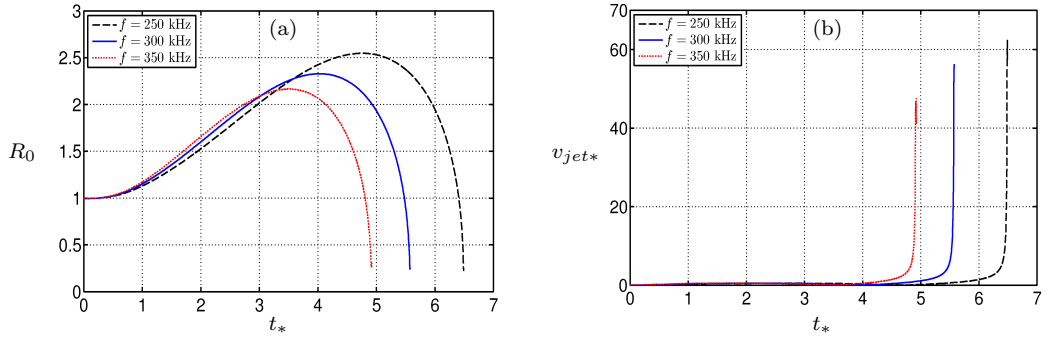

Figure 2.19: The histories of (a) the equivalent bubble radius R_* and (b) jet velocity v_{jet*} for the cases shown in figure 2.18.

2.4.5 Effects of the initial location ϕ_0 of the bubble in the acoustic field

Four different initial phases $\phi_0 = 0, \pi/2, \pi, 3\pi/2$ are investigated for the case shown in figure 2.8. At $\phi_0 = 3\pi/2$, a jet forms but disappears close the ends of the first and second collapses, and a wide jet forms at the end of the third collapse as shown in the figure 2.20. In the other three cases, the jet forms at the end of the first collapse phase. The jet direction does not change significantly with the initial phase.

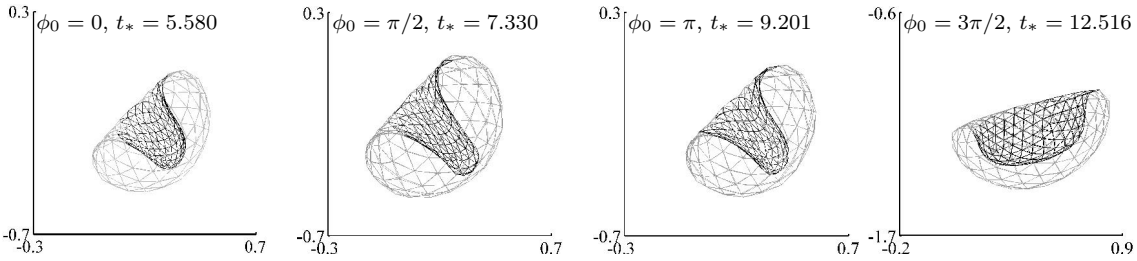

Figure 2.20: The bubble shapes at the end of the bubble lifetime at $\gamma = 3.75$ with the initial phase $\phi_0 = 0, \pi/2, \pi, 3\pi/2$, and the rest of the parameters are the same as in the case shown in figure 2.3.

2.5 Energy of the bubble system

The energy of a bubble system consists of the potential energy and kinetic energy, which remains as a constant when the surrounding liquid is incompressible and inviscid and the bubble system is not subject to an acoustic wave.

The potential energy in the liquid is equal to the work done on the liquid as the bubble with an constant vapour pressure p_v expands infinitely slowly against the ambient pressure p_∞ and the surface tension from zero volume (zero potential energy) to the volume V,

$$E_{pL} = \int_0^V (p_0 - p_v + \sigma \nabla \cdot \boldsymbol{n})\, dV. \tag{2.5.1}$$

The potential energy in the bubble gas is produced by infinitely slow, adiabatic compression from infinite volume (zero potential energy) to volume V,

$$E_{pG} = -\int_\infty^V p_g dV = -\int_\infty^V p_{g0} \left(\frac{V_0}{V}\right)^\kappa dV. \tag{2.5.2}$$

The total potential can be obtained as follows,

$$E_p = E_{pL} + E_{pG} = \frac{p_{g0} V_0}{\kappa - 1} \left(\frac{V_0}{V}\right)^{\kappa - 1} + \sigma S + V(p_0 - P_v), \tag{2.5.3}$$

where S is the bubble surface area. The potential energy can be added to an arbitrary constant, since only the variation of the potential has physical meaning. If we choose the initial potential energy as the value zero, we have

$$E_p = \frac{p_{g0} V_0}{\kappa - 1} \left(\left(\frac{V_0}{V}\right)^{\kappa - 1} - 1 \right) + \sigma \left(S - S_0\right) + \left(V - V_0\right) \left(p_0 - p_v\right), \tag{2.5.4}$$

where S_0 is the initial bubble surface area. The dimensionless form of the potential energy

is,

$$E_{p*} = \frac{\varepsilon V_{0*}}{\kappa - 1}\left(\left(\frac{V_{0*}}{V_*}\right)^{\kappa-1} - 1\right) + \sigma_*\left(S_* - S_{0*}\right) + \left(V_* - V_{0*}\right). \tag{2.5.5}$$

The kinetic energy for the liquid flow field is given as,

$$E_{k*} = \frac{1}{2}\int_{S_b} \varphi_* \frac{\partial \varphi_*}{\partial n} ds. \tag{2.5.6}$$

We have neglected the kinetic energy for the gas flow within the bubble, since the density of bubble gases is usually three orders of magnitude smaller than the liquid.

Figure 2.21 shows the history of the energy of the bubble system versus the equivalent bubble radius history for the acoustic bubble shown in figures 2.7-2.9. The bubble energy varies with time unlike being constant when not subject to an acoustic wave; this is due to the energy transfer between the bubble system and the acoustic wave. The bubble system absorbs the energy from the ultrasound and tranforms the uniform momentum of the ultrasound parallel to the wall to the highly concentrated momentum of a high-speed liquid jet pointing to the wall. This mechanism is assocated with applications to ultrasonic cleaning, sonochemistry and ultrasound therapeutics as illustrated in the introduction.

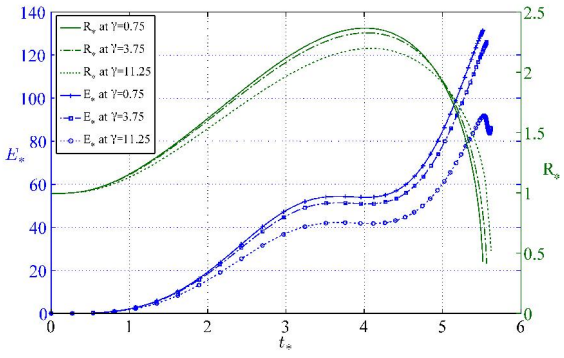

Figure 2.21: The histories of the energy E_* of the bubble system and the equivalent bubble radius R_* for the bubble near rigid wall for the case shown in figures 2.7-2.9 for a bubble at at $\gamma = 0.75$, 3.75, 11.25 respectively.

2.6 Chapter summary

Dynamics of cavitation microbubbles due to high intensity ultrasound are associated with important applications in biomedical ultrasound, ultrasonic cleaning, and sonochemistry. Previous numerical studies on this phenomenon were for an axisymmetric configuration. In this chapter, a computational model is developed to simulate the three dimensional dynamics of acoustic bubbles by using the boundary integral method. A bubble collapses much more violently subjected to high intensity ultrasound than when under normal constant ambient pressure. A few techniques are thus implemented to address the associated numerical challenge. In particular, a high quality mesh of the bubble surface is maintained by implementing a new hybrid approach of the Lagrangian method and elastic mesh technique. It avoids the numerical instabilities which occur at a sharp jet surface as well as generates a fine mesh needed at the jet surface. The model is validated against the Rayleigh-Plesset equation and an axisymmetric model. We then explore microbubble dynamics near a wall subjected to high intensity ultrasound propagating parallel to the wall, where the Bjerknes forces due to the ultrasound and the wall are perpendicular to each other. The bubble system absorbs the energy from the ultrasound and transforms the uniform momentum of the ultrasound parallel to the wall to the highly concentrated momentum of a high-speed liquid jet pointing to the wall. The liquid jet forms towards the end of the collapse phase with a significantly higher speed than without the presence of ultrasound. The jet direction depends mainly on the dimensionless standoff distance $\gamma = s/R_{\max}$ of the bubble from the wall, where s is the distance between the wall and the bubble centre at inception and $R_{\max}$ is the maximum bubble radius. The jet is approximately directed to the wall when γ is 1.5 or smaller and rotates to the direction of the ultrasound as γ increases. When γ is about 10 or larger, the wall effect is negligible and the jet is along the acoustic wave direction.

Chapter 3

Numerical modeling of the 3D dynamics of ultrasound contrast agent microbubbles using the boundary integral method

3.1 Physical and mathematical model

Consider the dynamics of UCAs near an infinite rigid plane wall subject to ultrasound, as shown in figure 3.1. A Cartesian coordinate system $O - xyz$ is adopted with the origin at the centre of the initial spherical UCA, the z-axis perpendicular to the wall and the x-axis along the wave direction. The far-field pressure p_∞ is thus modified to include a sinusoidal term,

$$p_\infty(x,t) = p_0 + p_a \sin(kx - \omega t) \tag{3.1.1}$$

where p_0 is the hydrostatic pressure, x is the coordinate along the propagation direction of the wave, t is time, and p_a, k and ω are the pressure amplitude, wave number and angular

frequency, respectively, of the acoustic wave.

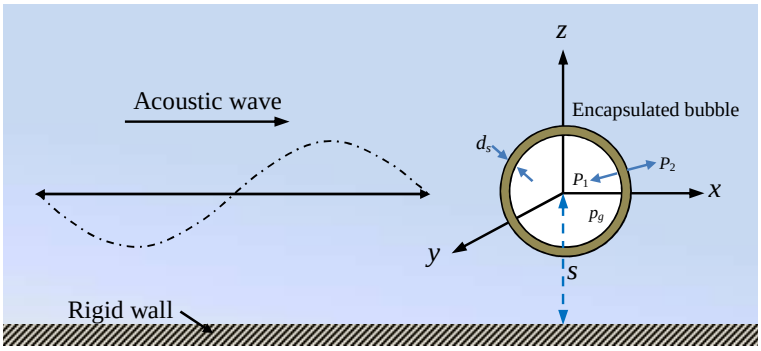

Figure 3.1: The configuration and coordinate system for an encapsulated microbubble near a rigid wall subject to ultrasound propagating parallel to the wall.

The UCA is assumed to be filled with a noncondensible filling gas and diffusion across the UCA surface is regarded as slow relative to the bubble dynamics and, thus, may be neglected. From the ideal gas law, we can assume that the gas pressure inside the UCA obeys a polytropic law, according to

$$p_g = p_{g0}\left(\frac{V_0}{V}\right)^{\alpha}, \tag{3.1.2}$$

where p_g and p_{g0} are the instantaneous and initial gas pressure inside the UCA, respectively, V and V_0 are the instantaneous and initial bubble volumes, respectively, and α is the polytropic coefficient. For isothermal behavior, $\alpha = 1$, and for adiabatic behavior, $\alpha = \kappa$, where κ is the ratio of specific heats of the interior gas. Unless otherwise noted, we set κ = 1.67 (argon) for the simulations presented here. The effects of κ on the dynamics are investigated in Section 3.4.5. The bubble is assumed to be in a state of equilibrium prior to the onset of the acoustic wave, which is applied instantly and continuously.

We assume that the fluid surrounding the bubble is inviscid, incompressible and the liquid flow is irrotational. The fluid velocity $\boldsymbol{v}$ thus has a potential φ, $\boldsymbol{v} = \nabla\varphi$ which satisfies Laplace's equation, $\nabla^2\varphi = 0$. Using Green's second identity, the potential φ may be

represented as a surface integral over the bubble surface S_b as follows,

$$c(\boldsymbol{r})\varphi(\boldsymbol{r}) = \int_{S_b} \left(\frac{\partial \varphi(\boldsymbol{q})}{\partial n} G(\boldsymbol{r}, \boldsymbol{q}) - \varphi(\boldsymbol{q}) \frac{\partial G(\boldsymbol{r}, \boldsymbol{q})}{\partial n} \right) dS(\boldsymbol{q}), \tag{3.1.3}$$

where $\boldsymbol{r}$ is the field point and $\boldsymbol{q}$ is the source point, $c(\boldsymbol{r})$ is the solid angle and $\boldsymbol{n}$ is the unit outward normal of the bubble surface S_b.

To satisfy the impermeable boundary condition on the wall, Green's function is given as follows,

$$G(\boldsymbol{r}, \boldsymbol{q}) = \frac{1}{|\boldsymbol{r} - \boldsymbol{q}|} + \frac{1}{|\boldsymbol{r} - \acute{\boldsymbol{q}}|}, \tag{3.1.4}$$

where $\acute{\boldsymbol{q}}$ is the image of $\boldsymbol{q}$ reflected about the wall.

Hoff's model [44] provides a normal stress difference $\Delta P = P_2 - P_1$ (see figure 3.1) across the shell for spherical coated bubbles, assuming the shell is a linear, incompressible, viscoelastic solid,

$$\Delta P = 12 G_s \frac{d_s R_{10}^2}{R_2^3} \left(1 - \frac{R_{10}}{R_1} \right) + 12 \mu_s \frac{d_s R_{10}^2}{R_2^3} \frac{\dot{R}_1}{R_1} \tag{3.1.5}$$

where R_1 and R_2 refer to the inner and outer radii of the spherical bubble, respectively, the subscript 0 refers to the initial state, d_s is the equilibrium shell thickness, and G_s and μ_s are the shear modulus and shear viscosity of the shell, respectively. The overdot denotes differentiation with respect to time. The shell is incompressible and the shell thickness varies to keep the shell volume constant. The constraint of incompressibility is built into the derivation of equation (3.1.5). For a thin shell, as assumed in this work, this constraint is approximated by $d_{si} R^2 = d_s R_0^2$, where d_{si} is the instantaneous shell thickness.

The UCA radius is about $O(1 - 10)$ μm and the coating thickness is in the range of

O(1-100) nm. We thus assume that the shell thickness d_s is much less than the bubble radius R ($d_s << R$). The shell is assumed to be infinitesimally thin, thus, $R = R_1 = R_2$, and (3.1.5) becomes,

$$\Delta P = 12\frac{d_s}{R_0^2}\left(\frac{R_0}{R}\right)^4\left[G_s(R - R_0) + \mu_s\dot{R}\right], \tag{3.1.6}$$

where R and R_0 are the instantaneous and initial bubble radii, respectively.

To adapt the Hoff model [44] to nonspherical bubbles, we treat ΔP as a local quantity that varies along the bubble surface and replace the radius R with $1/(\nabla \cdot \boldsymbol{n}) = R_c$, where $\nabla \cdot \boldsymbol{n}$ is the local mean curvature and R_c is the radius of the curvature. To incorporate the influence of ΔP on the bubble dynamics, we include it in the dynamic boundary condition as follows,

$$p_L = p_g - \sigma\nabla \cdot \boldsymbol{n} - \Delta P, \tag{3.1.7}$$

where p_L is the pressure of the flow on the bubble surface and σ is the surface tension. Using Bernoulli's equation along with the far-field pressure term in 3.1.1 and gas pressure in the bubble 3.1.2, 3.1.7 can be written as,

$$\frac{D\varphi}{Dt} = \frac{1}{2}\left|\nabla\varphi\right|^2 + \frac{1}{\rho}\left(-p_g + p_\infty(x,t) + \frac{2\sigma}{R_c} + \Delta P\right), \tag{3.1.8}$$

where ρ is the liquid density. Equation (3.1.8) is applied locally at every node of the bubble surface. We argue this simplified model can be used to approximate the essential effects of the coating for the following reasons. An encapsulated bubble is usually approximately spherical during most of its lifetime except for a very short period during the end of collapse when the bubble becomes nonspherical. This model thus provides a good estimate for the influence of the shell on the bubble, the asymmetric flow and pressure fields prior to jet development. When liquid jetting starts, the large asymmetric momentum of the

liquid flow and high pressure of the bubble gas are dominant effects; the elastic and viscous effects of the thin coating should be secondary effects.

Several models aside from that of Hoff have been developed to describe the dynamics of spherical, encapsulated microbubbles, perhaps most notably those by de Jong et al. [27, 26, 23, 24], Church [19], and Sarkar et al. [100]. The Church model was derived for shells of arbitrary thickness, whereas those by de Jong et al. and Sarkar et al. were developed for shells of infinitesimal thickness. The Hoff model obtains from that of Church when the shell thickness is much less than the outer radius, i.e., $d_s << R_{20}$. Both the Hoff and Church models use properties of the bulk material, e.g., shear modulus and shear viscosity, whereas those by de Jong et al. and Sarkar et al. use surface rheological properties that include the surface dilatational viscosity and dilatational elasticity. Our main interest is in describing the dynamics of thin-shell microbubbles due to their wider applicability in diagnostic imaging and therapeutic applications. We choose the Hoff model over that of Church due to its simplicity for the case of a thin shell. The Hoff model is more applicable for polymer-coated microbubbles, whereas the de Jong et al. and Sarkar et al. models are more applicable to lipid or surfactant coated microbubbles. However, the elastic term in the de Jong et al. and Sarkar et al. models is only valid for small oscillations [31]; the Hoff model is applicable to oscillations of arbitrary amplitude. Furthermore, unlike the de Jong et al. and Sarkar et al. models, the Hoff model incorporates shell softening, which reduces the influence of the shell as the bubble expands.

We choose the reference length R_0 (initial radius of the bubble) and the reference pressure p_0 to introduce the following dimensionless quantities denoted by an asterisk (*),

$$\boldsymbol{r}_* = \frac{\boldsymbol{r}}{R_0}, \quad t_* = \frac{t}{R_0}\sqrt{\frac{p_0}{\rho}}, \quad \varphi_* = \frac{\varphi}{R_0}\sqrt{\frac{\rho}{p_0}}, \tag{3.1.9a}$$

$$\varepsilon = \frac{p_{g0}}{p_0}, \quad \sigma_* = \frac{\sigma}{R_0 p_0}, \tag{3.1.9b}$$

$$p_{a*} = \frac{p_a}{p_0}, \quad \omega_* = \omega R_0 \sqrt{\frac{\rho}{p_0}}, \quad k_* = R_0 k, \tag{3.1.9c}$$

$$G_{s*} = \frac{G_s}{p_0}, \quad \mu_{s*} = \frac{\mu_s}{R_0\sqrt{\rho p_0}}, \quad d_{s*} = \frac{d_s}{R_0} \tag{3.1.9d}$$

The nondimensionalized kinematic and dynamic boundary conditions on the bubble surface are,

$$\frac{D\boldsymbol{r}_*}{Dt_*} = \nabla\varphi, \tag{3.1.10a}$$

$$\frac{D\varphi_*}{Dt_*} = 1 + \frac{1}{2}\left|\nabla\varphi_*\right|^2 - \varepsilon\left(\frac{V_0}{V}\right)^{\kappa} + \frac{2\sigma_*}{R_c} + p_{a*}\sin\left(k_* x_* - \omega_* t_*\right) + \Delta P_*. \tag{3.1.10b}$$

This equation incorporates the essential physics of the problem.

Following convention, the standoff distance is nondimensionalized with respect to the maximum equivalent bubble radius,

$$\gamma = \frac{s}{R_{\max}}, \tag{3.1.11}$$

where s is the distance between the wall and the bubble centre at inception (see figure 3.1), and $R_{\max}$ is the maximum radius a bubble initially in equilibrium would attain in an infinite ambient fluid subject to the imposed ultrasound.

We assume the flow is inviscid potential based on the following reasons: (i) a coated microbubble is approximately spherical during most of lifetime due to surface tension and the elastic stress of the coating. It may become nonspherical during a very short period at the end of collapse when the inertial effects are dominant and the viscous effects are negligible. (ii) The Reynolds number R_e for the liquid flow associated with microbubble dynamics appears large [76, 106]. As R_e is high we assume that the flow is dominated by inertia in the bulk with viscous effects being non-negligible only within a thin viscous boundary layer near the bubble [10, 72]. (iii) The fluid viscous shear stress on the coating

at $O(\mu_l\ \omega) = O(10^2 - 10^4)$ Pa is small compared to the elastic stress of the coating in the tangent plane at $O(G_s\delta^{-1}\varepsilon) = O(10^6 - 10^7)$ Pa, as fluid viscosity $\mu_l = 10^{-3}$ Pa s, $R_0 = 2$ - 10 μm, $\omega = O(10^5 - 10^7)$ and $G_s = 0.1$ - 0.9 N/m, assuming the strain of the coating ε is $O(10^{-1})$ [76, 106].

3.2 Validation for spherical oscillations

Properties of microbubbles, such as their radii, shell thickness and elasticity vary significantly among various types of UCAs. In this work, we consider coated microbubbles with initial radius R_0= 4.5 μm, a typical size of UCAs [102]. We fix the shear modulus G_s = 10 MPa, and use three different values of shell thickness and shell viscosity: d_s = 10, 15, 20 nm, and μ_s = 0.0, 0.2, 0.4 Pa s. As an example, thin-shell protein contrast agents (e.g., Albunex®) have a shell thickness of about 15 nm. For an experimental contrast agent with a polymer-coating from Nycomed (mean diameter ∼6 μm and shell thickness ∼5% of the particle radius), Hoff et al. [45] reported a shear modulus of 10.6 - 12.9 MPa and a shell viscosity of 0.39 - 0.49 Pa s. To validate this model for the restricted case of spherical oscillation of a coated bubble, the results were compared to the modified Rayleigh-Plesset equation used by [45] that accounts for the elastic and viscous effects of the shell. Using the present notation, this equation is given by,

$$\rho\left(R\ddot{R} + \frac{3}{2}\dot{R}\right) = p_{g0}\left(\frac{R_0}{R}\right)^{3\kappa} - p_\infty(x,t) - 12\mu_s\frac{d_sR_0^2}{R^3}\frac{\dot{R}}{R} - 12G_s\frac{d_sR_0^2}{R^3}\left(1 - \frac{R_0}{R}\right). \quad (3.2.1)$$

Note that the terms for the liquid viscosity and time derivative of the liquid pressure are neglected in the above equation, as we assume an inviscid and incompressible liquid.

Figure 3.2 shows comparisons of the bubble radius time history for a coated and uncoated bubble as determined from the 3D BIM model and modified Rayleigh-Plesset equation.

The parameters for the case are $R_0 = 4.5$ μm, $f = 300$ kHz, $p_{a*} = 0.8$, $G_s = 10.0$ MPa, $d_s = 15$ nm, and $\mu_s = 0$. We chose $M = 720$ elements on the bubble surface. The stiffening effects of the shell are evident and reduce the amplitude and period of the bubble oscillation. The BIM model agrees well with the Rayleigh-Plesset equation for both of the coated and uncoated bubbles for the first and second cycles of oscillation. After the second cycle, the uncoated BIM model starts to deviate obviously from the spherical bubble theory, since the bubble becomes nonspherical in the simulation.

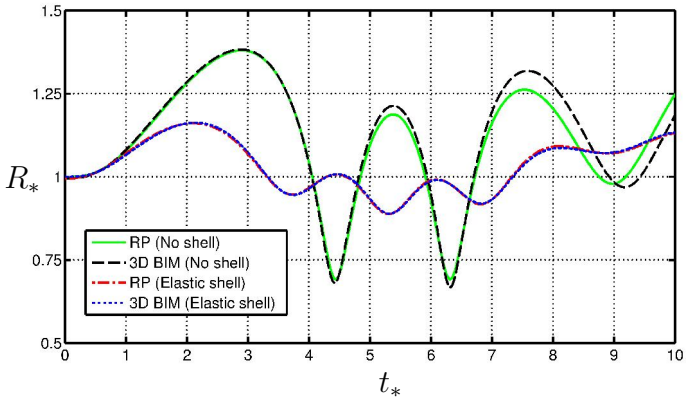

Figure 3.2: Comparisons of the bubble radius time history for a coated and uncoated bubble as determined from the BIM model and modified Rayleigh-Plesset equation. The parameters used for the both cases are $\kappa = 1.67$, $\sigma = 0.073$ N/m, $\varepsilon = 1 + 2\sigma_*$, $p_0 = 101.3$ kPa, $\rho = 999$ kg/m^3, $R_0 = 4.5$ μm, $f = 300$ kHz,and $p_{a*} = 0.8$. With shell $G_s = 10.0$ MPa, $d_s = 15$ nm, $\mu_s = 0$ and without shell d_s =0.

3.3 Coated bubble dynamics in an infinite fluid

Consider a coated bubble in an infinite fluid subject to ultrasound, with the pressure amplitudes $p_{a*} = 1.6$, 1.8, 2.0 and the remaining parameters the same as in figure 3.2. The coated bubble shapes for three cases are shown in figures 3.3, 3.4, and 3.5, respectively, in which the ultrasound propagates from left to right. In each case, the bubble expands spherically (figure 3.3a, 3.4a, 3.5a). The bubble surface distal from the source of the traveling wave becomes slightly flattened towards the end of collapse for $p_{a*} = 1.6$ (figures

3.3b, 3.3c). For p_{a*}=1.8, a jet develops on the proximal surface near the end of collapse (figure 3.4b), but disappears gradually during the subsequent rebound (figure 3.4c). For $p_{a*} = 2.0$, a high speed liquid jet forms along the direction of ultrasound propagation near the end of collapse (figure 3.5c), which subsequently impacts the opposite bubble surface.

The moment of jet impact is conventionally termed the end of collapse. In reality, the bubble continues to collapse in a toroidal form after jet impact, when the flow domain becomes doubly-connected. Toroidal bubbles are out of the scope of the present chapter. The doubly-connected domain can be made singly-connected by using a vortex sheet [134, 133] or a branch cut [2]. Wang, et al. [125, 126] developed a vortex ring model for the topological transition of a bubble and the subsequent toroidal bubble.

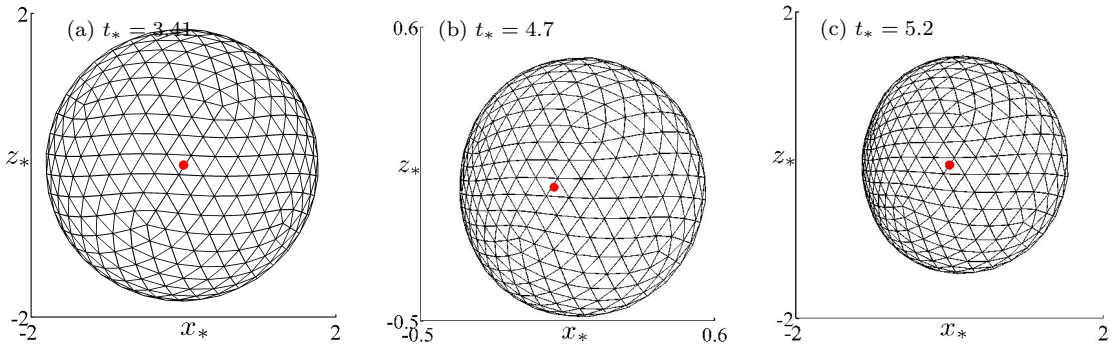

Figure 3.3: Coated bubble dynamics in an infinite fluid subject to an ultrasound pressure amplitude of $p_{a*} = 1.6$ with the remaining parameters the same as in figure 3.2. The direction of ultrasound propagation is from left to right. The bubble shapes are shown at (a) first maximum volume, (b) first minimum volume, and (c) second maximum volume.

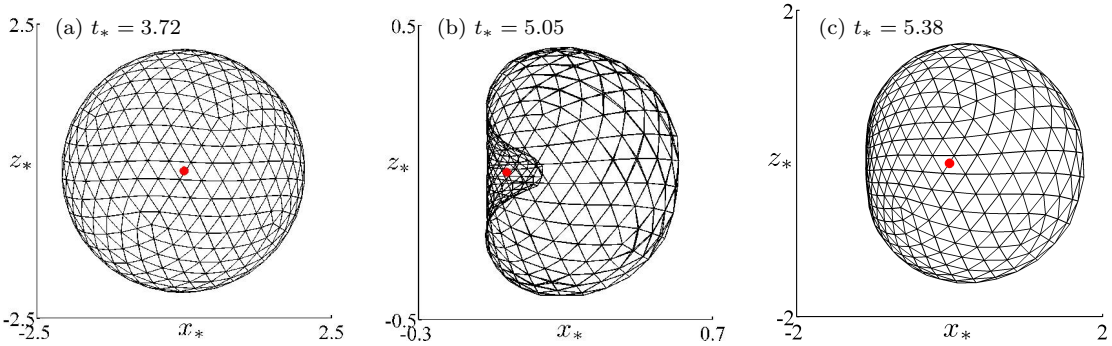

Figure 3.4: Coated bubble dynamics in an infinite fluid subject to an acoustic pressure amplitude of $p_{a*} = 1.8$ with the remaining parameters the same as in figure 3.2. The direction of ultrasound propagation is from left to right. The bubble shapes are shown at (a) first maximum volume, (b) first minimum volume and (c) second maximum volume.

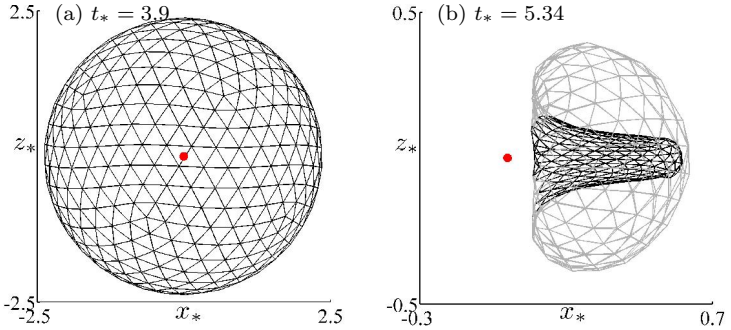

Figure 3.5: Coated bubble dynamics in an infinite fluid subject to an acoustic pressure amplitude of $p_{a*} = 2.0$ with the remaining parameters the same as in figure 3.2. The direction of ultrasound propagation is from left to right. The bubble shapes are shown at (a) maximum volume and (b) the end of collapse.

For bubbles in an infinite liquid, Figure 3.6 shows the corresponding uncoated bubble shapes at the end of collapse subject to ultrasound pressure amplitudes of p_{a*}= 1.6, 1.8, 2.0 with the remaining parameters the same as in figures 3.3, 3.4, and 3.5. For all three uncoated bubble cases, a bubble jet forms at the end of collapse. The threshold of acoustic pressure amplitude necessary for bubble jetting increases with the bubble coating. A comparison of figures 3.5b and 3.6c shows that the bubble jet is much sharper for a coated bubble.

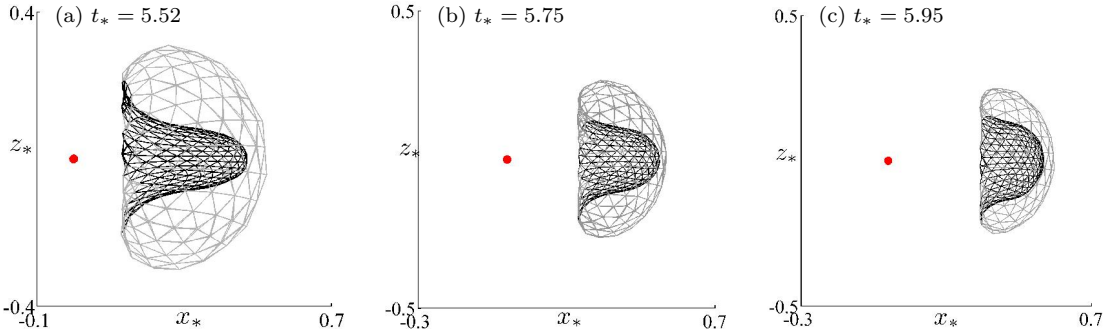

Figure 3.6: Uncoated bubble shapes at the end of collapse in an infinite fluid subject to ultrasound for acoustic pressure amplitudes of (a) $p_{a*} = 1.6$, (b) $p_{a*} = 1.8$, and (c) $p_{a*} = 2.0$. The remaining parameters are the same as in figure 3.2 except that $G_s = 0$ and $d_s = 0$ to negate the effect of the shell. The direction of ultrasound propagation is from left to right.

3.4 Coated bubble dynamics near a wall subject to an acoustic wave parallel to the wall

3.4.1 The effect of standoff distance

In this section, we study microbubble dynamics near a rigid wall subject to ultrasound propagating parallel to the wall. To study the effects of the standoff distance of the bubble from the wall, we consider three cases at $\gamma = 0.75$, 3.75 and 11.25, respectively, for $p_{a*} = 2.0$, with the remaining parameters the same as in figure 3.2. For the case $\gamma = 11.25$, the bubble remains spherical for most of its lifetime, however, a high-speed liquid jet develops in the direction of the wave at the last stage of the collapse, as shown in figure 3.7. This case is similar to that of a bubble in an infinite fluid (figure 3.5).

Figure 3.8 shows the bubble shapes at typical times for the case $\gamma = 3.75$. The bubble again remains approximately spherical during the expansion and collapse phases except for a high-speed liquid jet that develops rapidly towards the end of the collapse phase. However, the jet is along the bisector of the angle between the perpendicular primary and

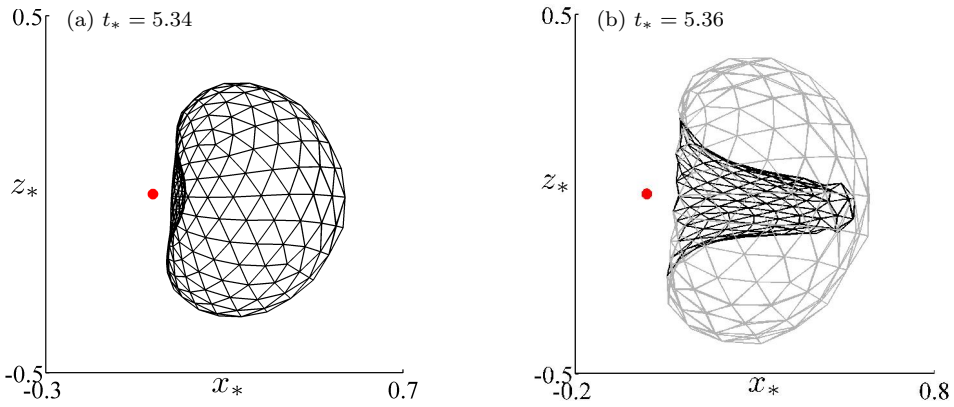

Figure 3.7: Jet development of a coated bubble far from a wall subject to ultrasound propagating parallel to the wall for $\gamma = 11.25$, $p_{a*} = 2.0$ with the remaining parameters the same as in figure 3.2.

secondary Bjerknes forces that are due to the acoustic wave and the wall, respectively (figures 3.8c, d).

The bubble shapes for $\gamma = 0.75$ at typical times are shown in figure 3.9. The bubble surface proximal to the wall is slightly flattened due to the wall, causing a nonspherical shape during the last stage of the expansion (figure 3.9b). The bubble collapses nonspherically and a large liquid jet develops on the distal side of the bubble directed towards the wall. The jet development time is only 0.4% of the oscillation period for the cases $\gamma = 3.75$ and 11.25, but is 0.9% for the case $\gamma = 0.75$.

Figures 3.10a, 3.10b and 3.10c show the bubble shapes at the end of collapse for a corresponding uncoated bubble with the same parameters as the previous cases shown in figures 3.7, 3.8 and 3.9 respectively. The jets are flatter and wider relative to the bubble size, and the bubble volumes at the end of collapse are smaller for uncoated bubbles compared to coated bubbles.

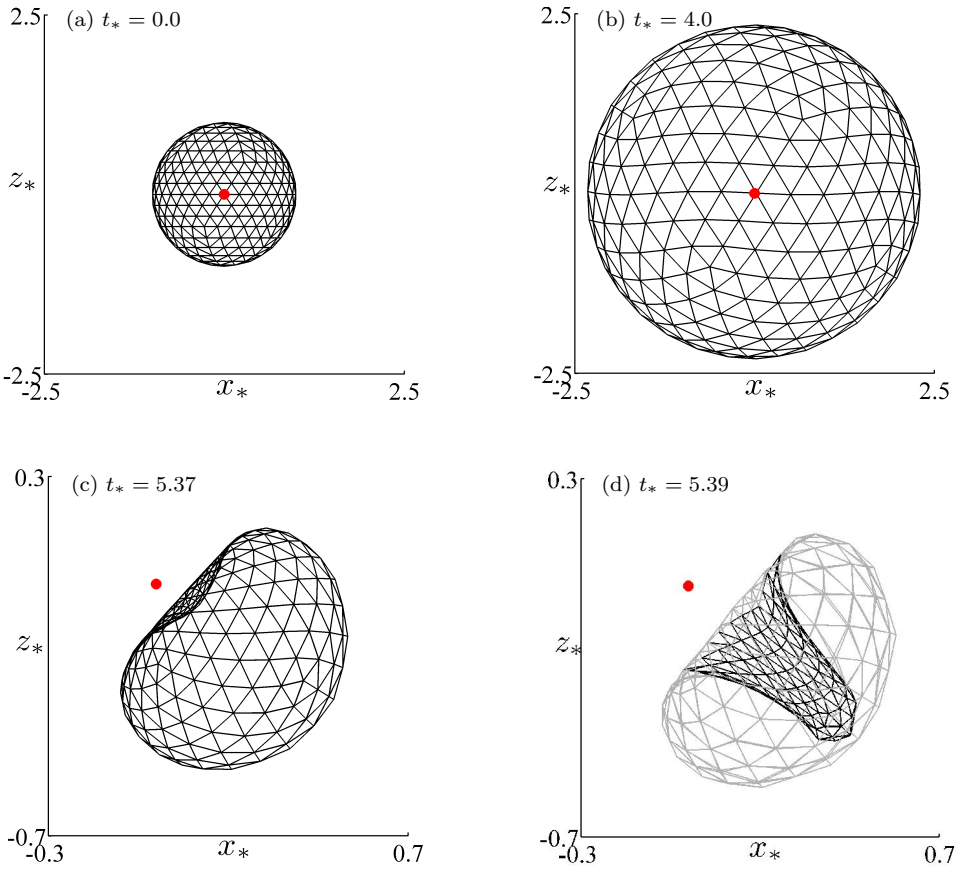

Figure 3.8: Coated bubble dynamics near a wall subject to ultrasound propagating parallel to the wall for $\gamma = 3.75$, $p_{a*} = 2.0$ with the remaining parameters the same as in figure 3.2. The bubble shapes are shown during the expansion phase (a-b) and collapse phase (b-d).

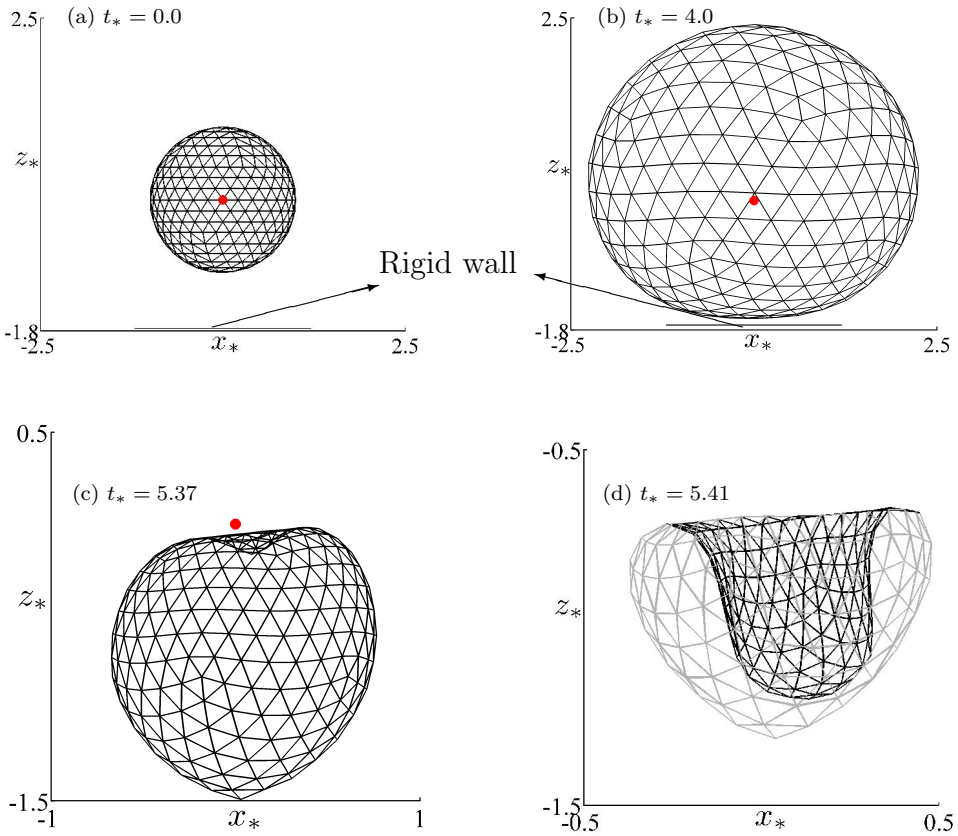

Figure 3.9: Coated bubble dynamics near a wall subject to ultrasound propagating parallel to the wall for $\gamma = 0.75$, $p_{a*} = 2.0$ with the remaining parameters the same as in figure 3.2. The bubble shapes are shown during the expansion phase (a-b) and collapse phase (b-d).

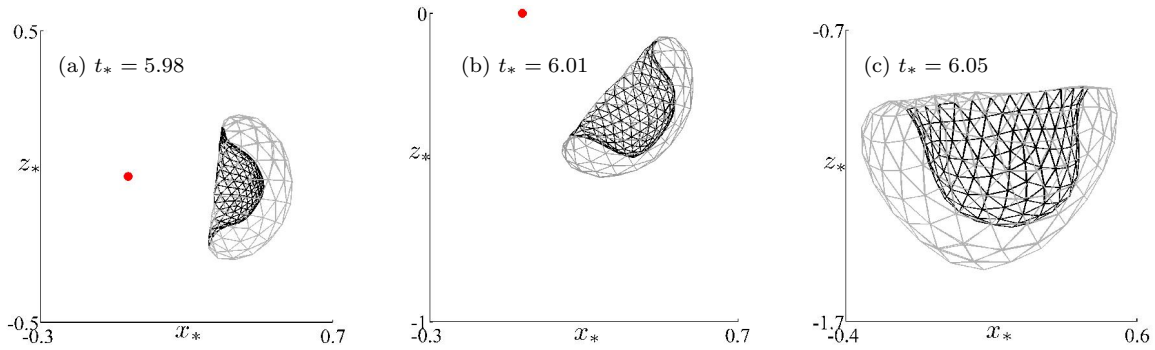

Figure 3.10: Jet shapes at jet impact for an uncoated bubble near a wall for (a) $\gamma = 11.25$, (b) $\gamma = 3.75$ and (c) $\gamma = 0.75$, corresponding to the cases shown in figures 3.7, 3.8 and 3.9, respectively

Some global dimensionless quantities are compared in table 3.1 for the coated and uncoated bubble cases shown in figures 3.7 - 3.10 including the maximum value $R_{\max *}$ of the equivalent bubble radius $R_{eq*} = \sqrt[3]{\frac{3}{4\pi}V_*}$, the oscillation period T_{c*}, the jet angle θ_j, and the angle θ_K and amplitude I_{K*} of the Kelvin impulse at jet impact. Here θ_j and θ_K are measured relative to the horizontal x-axis in the counterclockwise (positive) direction. For both coated and uncoated bubbles, the maximum equivalent radius $R_{\max *}$ increases with the dimensionless standoff distance γ, while the oscillation period T_{c*} and Kelvin impulse amplitude I_{K*} decrease with γ. The Kelvin impulse angles at jet impact are about the same as the jet directions for all the cases.

The jet direction does not change significantly due to the existence of a bubble coating. For the bubble with and without a coating, the jet is directed approximately towards the wall at $\gamma = 0.75$ ($\theta_j \approx -86°$), rotates counterclockwise towards the direction of ultrasound propagation with increasing dimensionless standoff distance γ, and is approximately along the ultrasound direction ($\theta_j \approx -4°$) for $\gamma = 11.25$.

Figure 3.11a, compares the jet velocities history v_{jet*} for bubbles with and without a coating near a rigid wall for the cases shown in figures 3.7 - 3.10 at various values of γ. For both cases, the jet velocity increases with γ, but increases more significantly for an uncoated bubble. The jet velocity, however, reduces significantly due to the existence of a coating. The maximum Mach number at the jet tip reaches 0.8 and is larger than 0.1

γ	Coated					Uncoated				
	$R_{\max *}$	T_{c*}	θ_j	θ_K	I_{K*}	$R_{\max *}$	T_{c*}	θ_j	θ_K	I_{K*}
0.75	2.17	5.42	$-86°$	$-86°$	3.4	2.68	6.05	$-86°$	$-86°$	5.7
3.75	2.31	5.39	$-40°$	$-40°$	1.2	2.86	6.01	$-42°$	$-43°$	2.35
11.25	2.35	5.36	$-4°$	$-5°$	0.98	2.91	5.98	$-7°$	$-6°$	1.92

Table 3.1: The maximum equivalent radius $R_{\max *}$, bubble lifetime T_{c*}, jet direction θ_j, and angle θ_K and amplitude I_{K*} of the Kelvin impulse at jet impact for the cases shown in figures 3.7 - 3.10. Here θ_j and θ_K are measured relative to the horizontal x-axis in the counterclockwise (positive) direction.

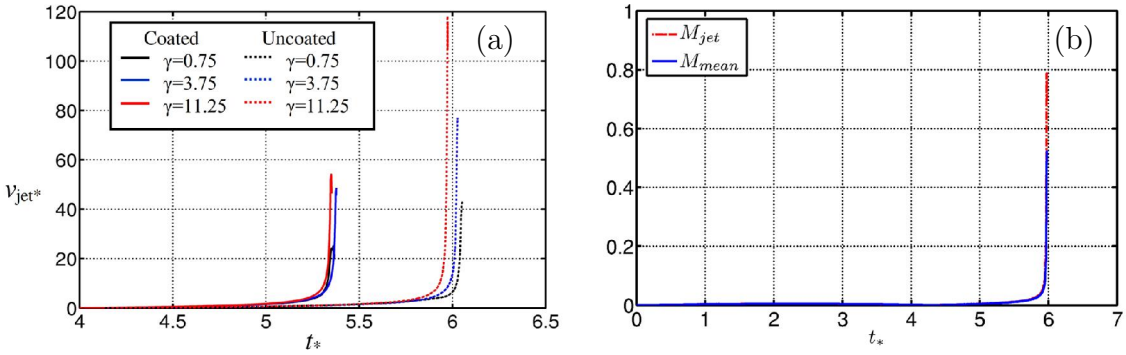

Figure 3.11: (a) Jet velocity v_{jet*} versus time t_* for bubbles with and without a coating for the cases shown in figures 3.7 - 3.10 with dimensionless standoff distances $\gamma = 0.75$, 3.75, and 11.25. (b) The histories of the average Mach number M_{mean} and the Mach number of the jet M_{jet} for the uncoated case at $\gamma = 11.25$.

for about 0.07% of the oscillation period (figure 3.11b), assume the speed of sound in water is 1500 ms^{-1}. The average Mach number over the bubble surface is small for bubble dynamics subject to ultrasound [121]. Consequently, the compressible effects should be insignificant.

3.4.2 The effect of shell thickness

Three different shell thicknesses, $d_s = 10$, 15, and 20 nm, are examined for two initial standoff distances, $\gamma = 3.75$ and 0.75, under ultrasonic forcing with amplitude $p_{a*} = 2.2$ and the remaining parameters the same as in figure 3.2.

Figure 3.12 shows the jet shapes at the end of collapse for the coated bubble near a rigid wall for $\gamma = 3.75$, p_{a*}= 2.2 and various shell thicknesses. As the shell thickness increases, the jet direction does not change appreciably but the jet becomes sharper and the bubble volume at the end of the collapse increases. The direction of the Kelvin impulse θ_K is very similar to the jet direction θ_j at jet impact.

Figure 3.13 shows the time history of the equivalent bubble radius R_{eq*}, jet velocity and centroid motion for the cases shown in figure 3.12. The expansion phase takes more than

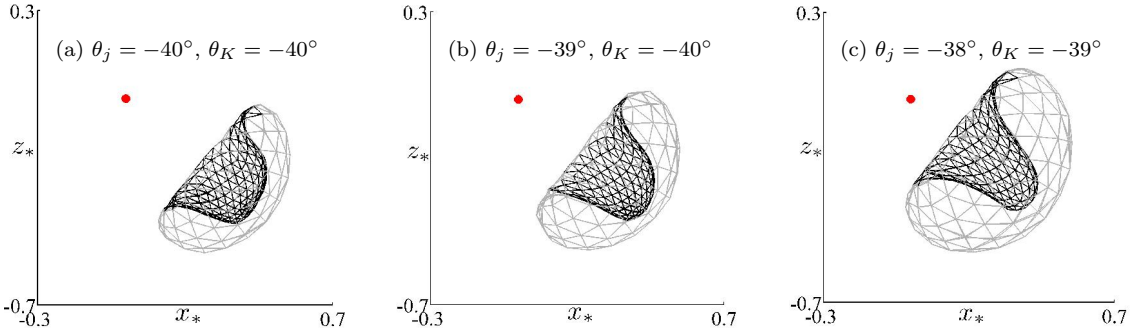

Figure 3.12: Jet shapes at jet impact for a coated bubble near a rigid wall for $\gamma = 3.75$, $p_{a*} = 2.2$ and shell thickness (a) $d_s = 10$ nm, (b) $d_s = 15$ nm, and (c) $d_s = 20$ nm. The remaining parameters are the same as in figure 3.2.

two thirds of the oscillation period and the maximum volume reduces about 13% as d_s is increased from 10 nm to 20 nm (figure 3.13a). The bubble wall velocity does not exceed 6 m s^{-1} until a high-speed liquid jet forms, at which time it increases rapidly. The maximum jet velocities are 920, 830, and 640 m s^{-1} for $d_s = 10$, 15, and 20 nm, respectively, so that the maximum jet velocity is reduced about 30% as d_s is increased from 10 to 20 nm (figure 3.13b). The x- and z-components of the centroid movement are approximately equal in quantity since the primary and secondary Bjerknes forces due to the acoustic wave and wall, respectively, are comparable in amplitude for this case (figures 3.13c, d). There is no centroid movement along the y-axis as the bubble is symmetric with respect to the zx-plane. In the expansion phase, the bubble moves slightly away from the wall and in the direction opposite the wave propagation direction, but it moves rapidly towards the rigid wall and along the wave propagation direction during the collapse phase. The bubble migration along both axes decreases with the shell thickness d_s.

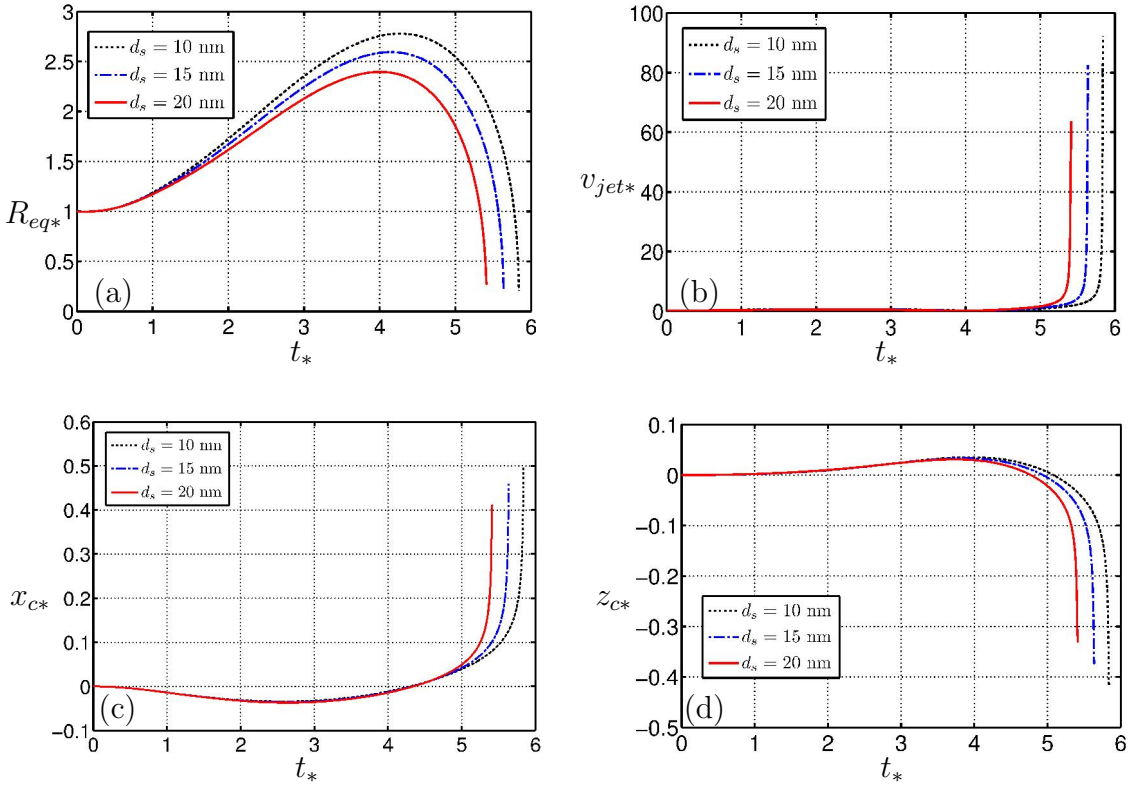

Figure 3.13: Time histories of (a) equivalent bubble radius R_{eq*}, (b) jet velocity v_{jet*}, (c) x-component of the centroid x_{c*}, and (d) z-component of the centroid z_{c*}, for the cases shown in figure 3.12.

The corresponding results for various thicknesses for $\gamma = 0.75$ are shown in figures 3.14 and 3.15. The jet direction and bubble shape do not change appreciably with d_s but the jet becomes slightly sharper with increasing d_s (figure 3.14). The expansion phase again takes more than two-thirds of the oscillation period and the maximum volume reduces with d_s in a similar manner as the case for $\gamma = 3.75$ (figure 3.15a). The bubble wall velocity does not exceed 2 m s^{-1} until a high-speed liquid jet forms that achieves a maximum velocity of $\sim$330 m s^{-1} (figure 3.15b). The maximum jet velocities are 337, 329, and 315, m s^{-1} for d_s = 10, 15, and 20 nm, respectively, which represents a $\sim$7% decrease as d_s is increased from 10 nm to 20 nm (figure 3.15b). The centroid movement along the z-axis is much larger than along the x-axis due to the strong wall attraction in this case (figures 3.15c, d). In the expansion phase, the bubble moves slightly away from the wall and in the direction

opposite the wave propagation direction, but it moves rapidly towards the rigid wall and along the wave propagation direction during the collapse phase.

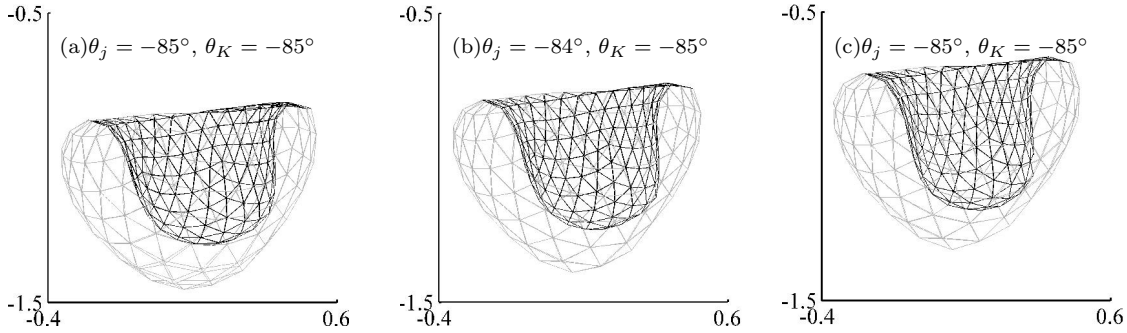

Figure 3.14: Jet shapes at jet impact for a coated bubble near a wall for γ= 0.75, $p_{a*} = 2.2$ and shell thickness (a) $d_s = 10$ nm, (b) $d_s = 15$ nm, and (c) $d_s = 20$ nm. The remaining parameters are the same as in 3.2

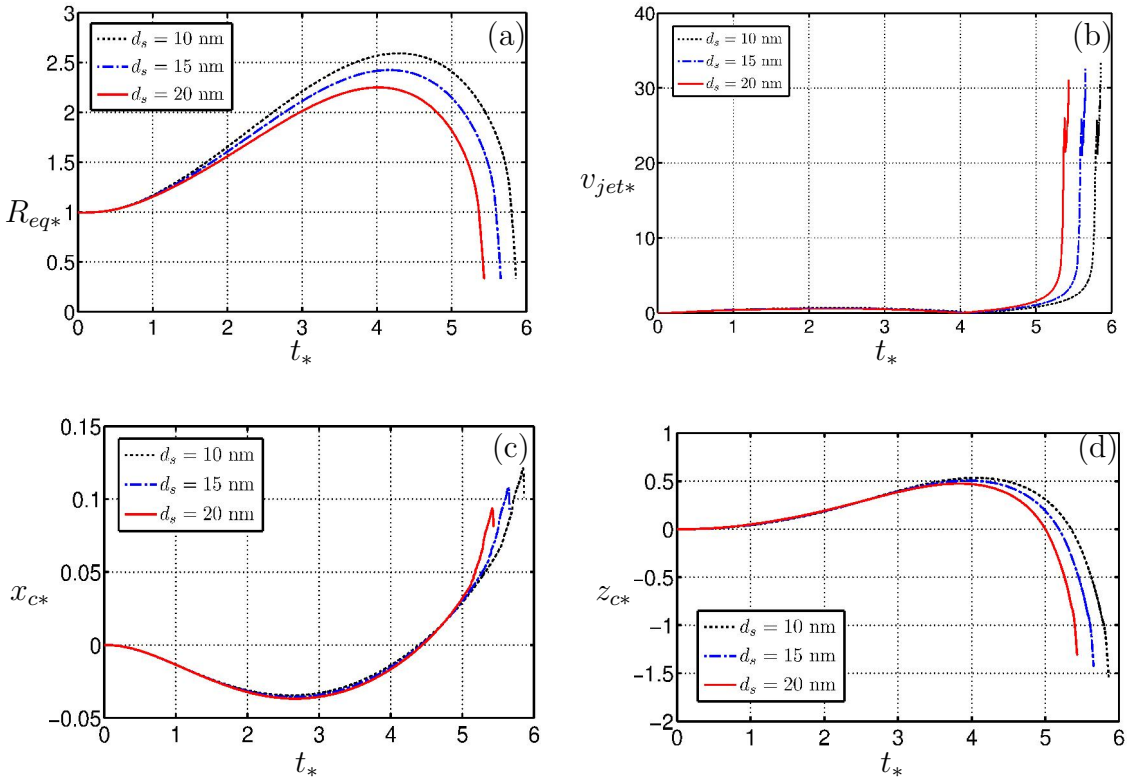

Figure 3.15: Time histories of (a) equivalent bubble radius R_{eq*}, (b) jet velocity v_{jet*}, (c) x-component of the centroid x_{c*}, and (d) z-component of the centroid z_{c*}, for the cases shown in figure 3.14.

3.4.3 The effect of shell viscosity

Figures 3.16 and 3.17 show the bubble shapes at the end of collapse for the cases $\gamma = 3.75$ and 0.75, respectively, and various shell viscosities, $\mu_s = 0.0$, 0.2, and 0.4 Pa $\cdot$ s, subject to ultrasound with $p_{a*} = 2.2$. The remaining parameters are the same as in figure 3.2. The jet direction does not change significantly with increasing μ_s while the jet becomes sharper. At jet impact, the jet direction θ_j is approximately along the Kelvin impulse direction θ_K and the bubble volume increases with μ_s for γ= 3.75 (figure 3.16). However, when the bubble is very near the wall with γ= 0.75, the jet shape and direction, and the bubble shape at the end of collapse do not change significantly with μ_s (figure 3.17).

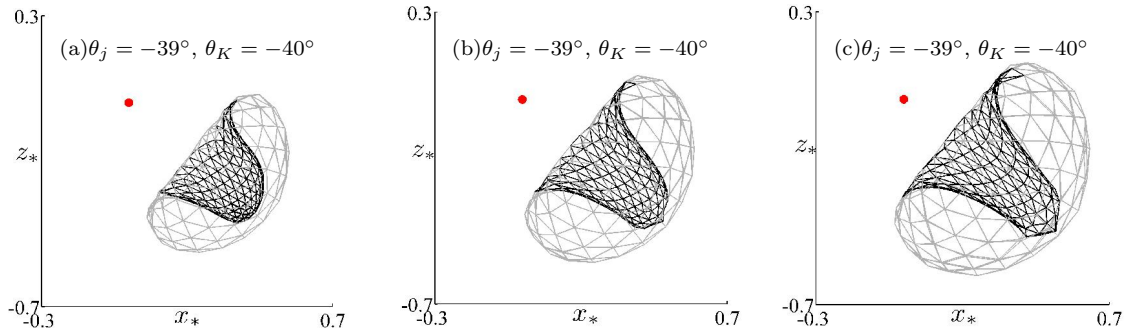

Figure 3.16: Jet shapes at jet impact for a coated bubble near a rigid wall for $\gamma = 3.75$, $p_{a*} = 2.2$ and shell viscosity (a) $\mu_s = 0.0$ Pa $\cdot$ s, (b) $\mu_s = 0.2$ Pa $\cdot$ s, and (c) $\mu_s = 0.4$ Pa $\cdot$ s. The remaining parameters are the same as in figure 3.2.

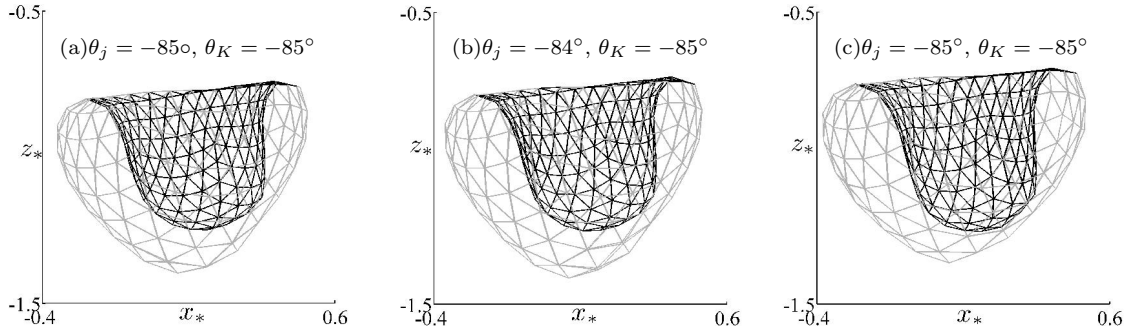

Figure 3.17: Jet shapes at jet impact for a coated bubble near a rigid wall for $\gamma = 0.75$, $p_{a*} = 2.2$ and shell viscosity (a) $\mu_s = 0.0$ Pa $\cdot$ s, (b) $\mu_s = 0.2$ Pa $\cdot$ s, and (c) $\mu_s = 0.4$ Pa $\cdot$ s. The remaining parameters are the same as in figure 3.2.

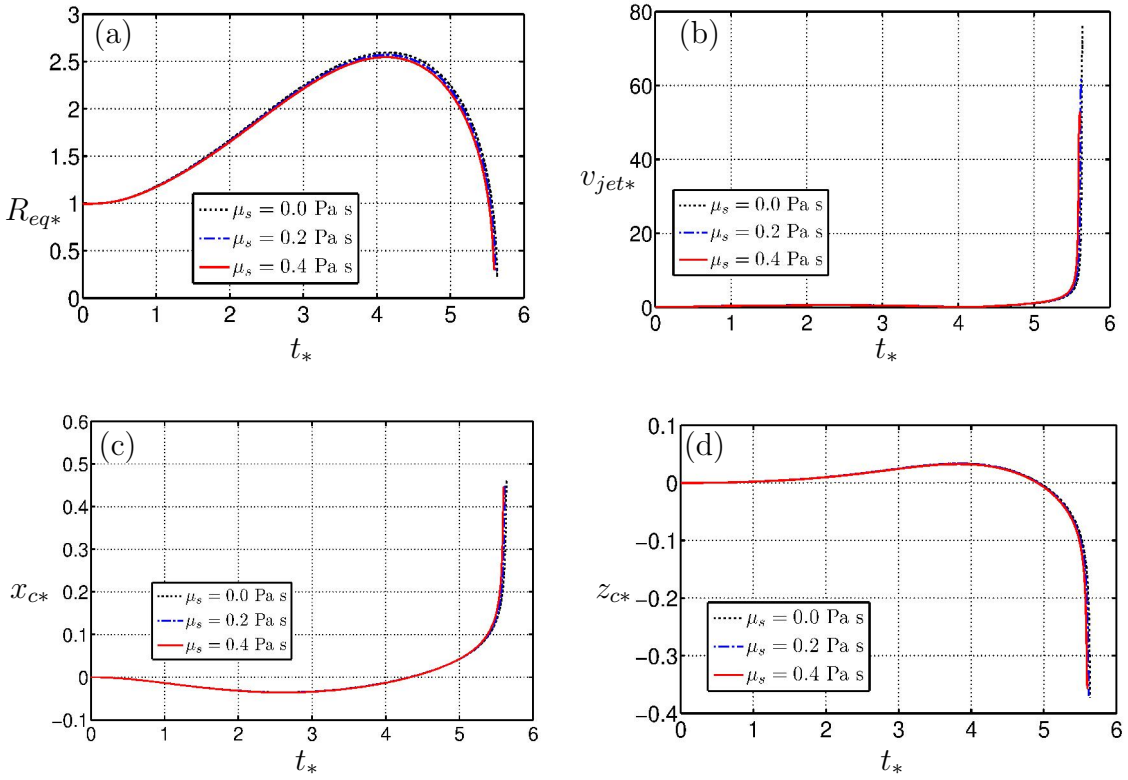

Figure 3.18: Time histories of (a) equivalent bubble radius R_{eq*}, (b) jet velocity v_{jet*}, (c) x-component of the centroid x_{c*}, and (d) z-component of the centroid z_{c*}, for the cases shown in figure 3.16.

Figures 3.18 and 3.19 show the time histories of the equivalent bubble radius, jet velocity, and centroid movement of the bubble for the cases shown in figures 3.16 and 3.17, respectively. In both cases, the bubble volume and centroid movement are not sensitive to the shell viscosity μ_s. The jet velocity does not change considerably for $\gamma = 0.75$ (figure 3.19b), but decreases $\sim$30% as μ_s is increased from 0 to 0.4 Pa s for $\gamma = 3.75$ (figure 3.18b).

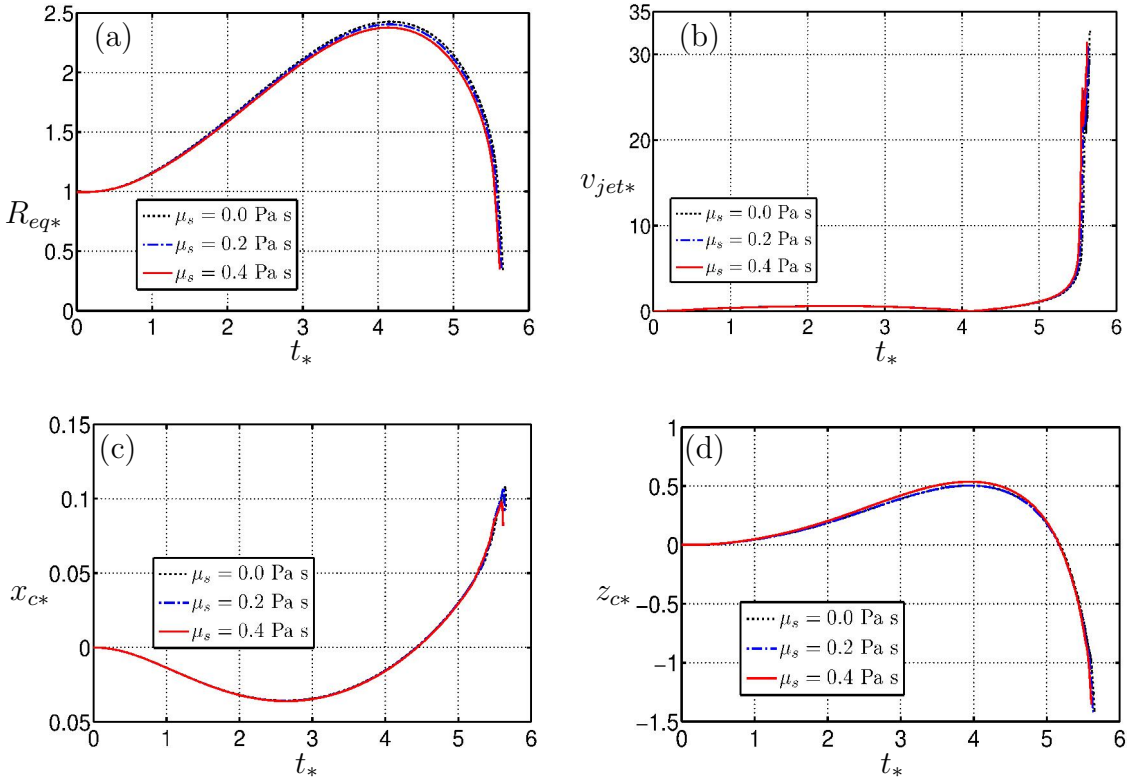

Figure 3.19: Time histories of (a) equivalent bubble radius R_{eq*}, (b) jet velocity v_{jet*}, (c) x-component of the centroid x_{c*}, and (d) z-component of the centroid z_{c*}, for the cases shown in figure 3.17.

3.4.4 The liquid viscosity effects in the coated bubble

In the theory of viscous potential flow (VPF) [51, 131], viscous effects are calculated by including the viscous stresses on irrotational flows. The normal stress balance on the bubble surface (3.1.7), considering the surface tension and normal viscous stress, is given as follows:

$$p_L = p_g - \sigma \nabla \cdot \boldsymbol{n} + 2\mu \frac{\partial^2 \varphi}{\partial n^2} - \Delta P. \tag{3.4.1}$$

The dimensionless dynamic boundary condition on the bubble surface in 3.1.10b is written as follows:

$$\begin{aligned} \frac{D\varphi_*}{Dt_*} = 1 + \frac{1}{2}\left|\nabla \varphi_*\right|^2 - \varepsilon \left(\frac{V_0}{V}\right)^{\kappa} + \frac{2\sigma_*}{R_c} \\ - \frac{2}{R_e}\frac{\partial^2 \varphi_*}{\partial n^2} + p_{a*} \sin\left(k_* x_* - \omega_* t_*\right) + \Delta P_*, \end{aligned} \tag{3.4.2}$$

where $R_e = R_0\sqrt{p_0 \rho}/\mu_l$. The term $\frac{\partial^2 \varphi}{\partial n^2}$ can be calculated as follows:

$$\frac{\partial^2 \varphi}{\partial n^2} = \boldsymbol{n} \cdot \nabla \varphi_n = \boldsymbol{n} \cdot \frac{\partial}{\partial n} \nabla \varphi = n_x \frac{\partial \varphi_x}{\partial n} + n_y \frac{\partial \varphi_y}{\partial n} + n_z \frac{\partial \varphi_z}{\partial n}, \tag{3.4.3}$$

where (n_x, n_y, n_z) are the components of the unit normal vector. φ_x, φ_y, and φ_z satisfy Laplace's equation since φ satisfies Laplace's equation. They thus satisfy the boundary integral equation (3.1.3). As a result, we can replace φ in (3.1.3) by φ_x, φ_y, and φ_z to formulate the boundary integral equations to find the terms $\partial\varphi_x/\partial n$, $\partial\varphi_y/\partial n$ and $\partial\varphi_z/\partial n$, respectively. Subsequently, $\partial\varphi^2/\partial n^2$ is calculated from (3.4.3).

Figure 3.20a and 3.20b compares the bubble shapes at the moment of jet impact at R_e=45, ∞, i.e., with and without viscous effects respectively. The bubble jet becomes sharper with the viscous effects however the jet direction does not change significantly. Figure

3.21 compares the time histories of the corresponding jet velocities for the two cases. The maximum jet velocity reduces about 18% due to the viscous effects and the oscillation period reduces about 5%.

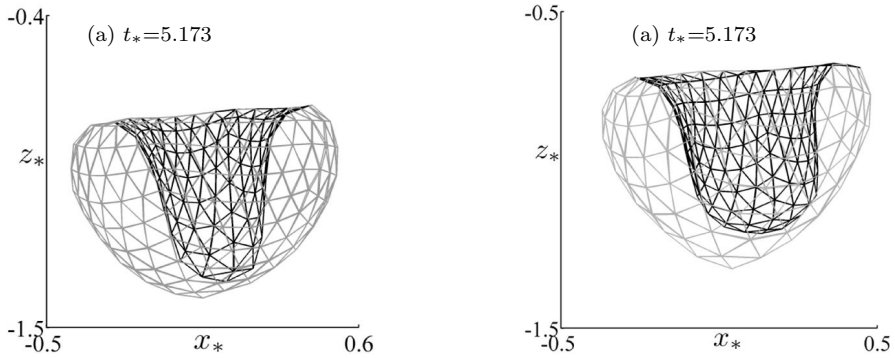

Figure 3.20: Coated bubble dynamics near a wall subject to ultrasound propagating parallel to the wall for $\gamma = 0.75$, $p_{a*} = 2.0$ with the remaining parameters the same as in figure 3.2. The bubble shapes are shown at the end of the collapse phase by considering fluid viscosity with (a) R_e=45, (b) $R_e = \infty$.

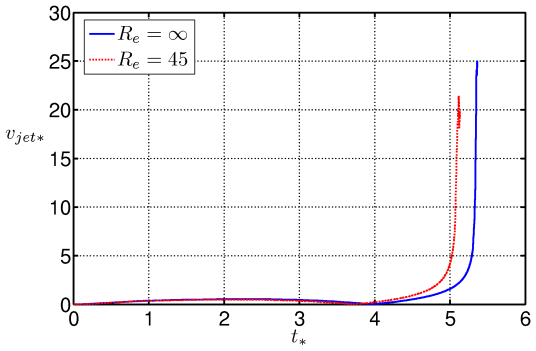

Figure 3.21: Jet velocity v_{jet*} versus time t_* for the cases shown in figures 3.20.

3.4.5 The effect of the Heat Capacity Ratio, κ

In this section, we explore the effect of varying the heat capacity ratio, κ, of the noncondensable interior gas. All prior simulations assumed $\kappa = 1.667$, the value for argon. Here, we examine three additional values, $\kappa = 1.4$, 1.25, and 1.08, which correspond respectively to air, TNT [20], and tetrafluorocarbon, a gas used in some UCAs.

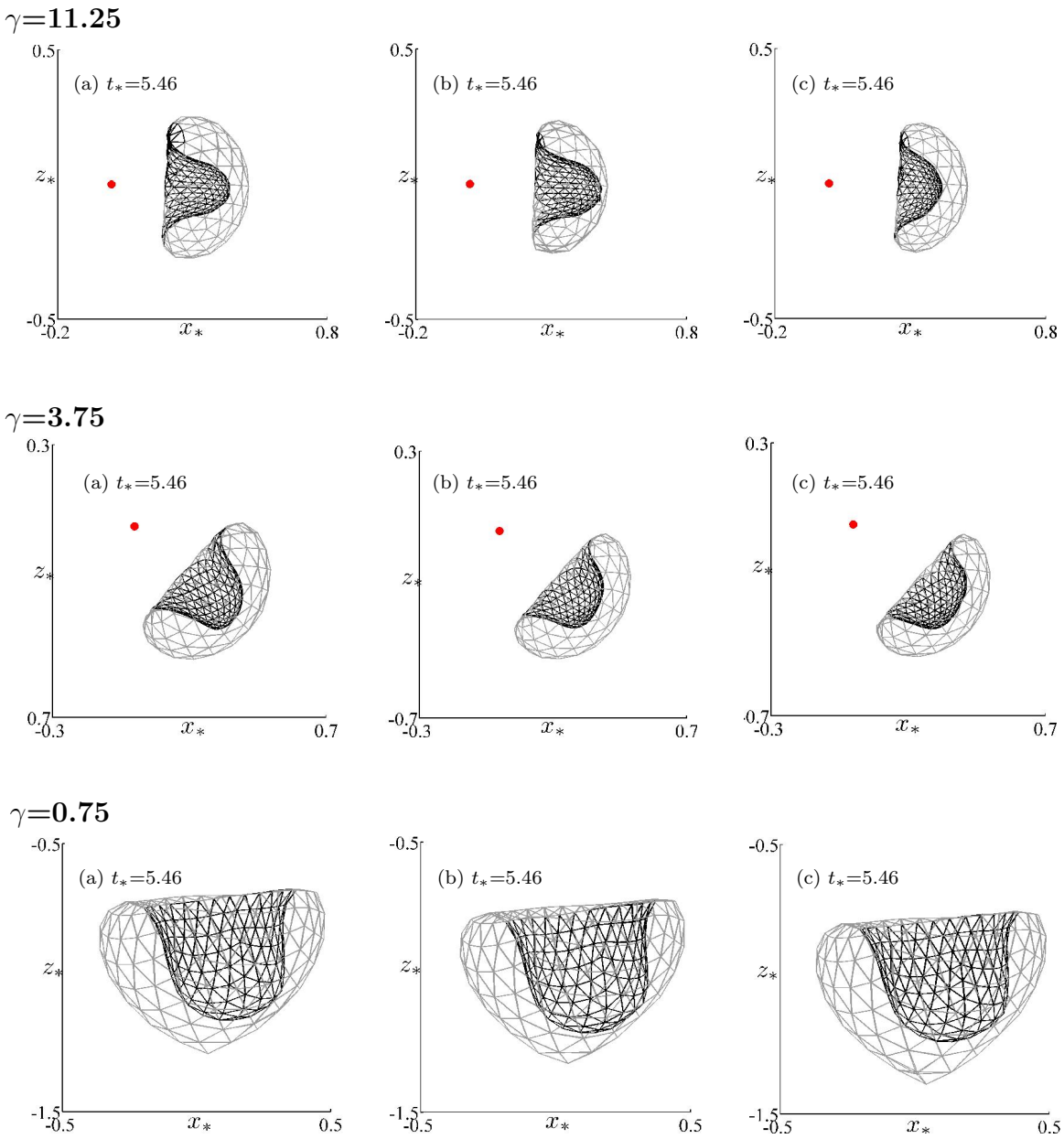

Figure 3.22: Jet shapes for the bubble near a rigid wall for $\gamma = 0.75$, 3.75, and 11.25 and ratio of specific heats (a) $\kappa = 1.4$, (b) $\kappa = 1.25$, and (c) $\kappa = 1.08$. The remaining parameters are the same as in figure 3.7, 3.8 and 3.9.

Figure 3.22 depicts bubble shapes at the end of the collapse phase for three heat capacity ratios, $\kappa = 1.4$, 1.25, and 1.08, and for different values of γ corresponding to the cases in figures 3.7, 3.8, and 3.9. The jet direction and bubble shapes do not change appreciably with κ, but the jet becomes stronger and wider as κ is reduced, particularly for the cases γ

= 3.75 and 11.25. In some cases, the code breaks down before the jet impacts the opposite side of the bubble as the jet is strong and highly unstable.

Figure 3.23, shows the maximum equivalent bubble radius, $R_{\max*}$, and maximum jet velocity, M_{vjet*}, for the cases shown in figure 3.7, 3.8, 3.9 and 3.22. In all cases, these quantities decrease with increasing κ. The decrease in $R_{\max*}$ is approximately constant and about 10% over the range of κ considered, for all γ. However, the decrease in M_{vjet*} over this range increases significantly with γ.

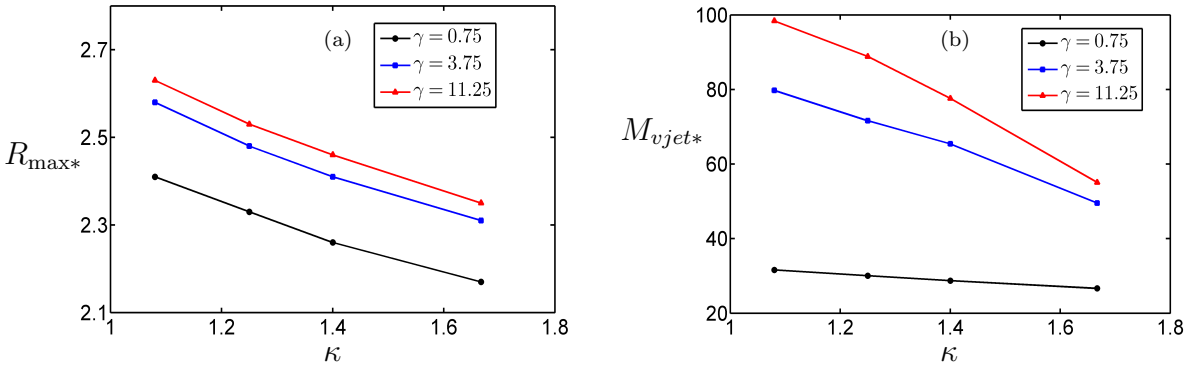

Figure 3.23: The ratio of specific heat κ versus, (a) Maximum equivalent bubble radius $R_{\max*}$, (b) Maximum jet velocity M_{vjet*} for the γ=0.75, 3.75 and 11.25.

3.5 Coated bubble dynamics near a wall subject to an acoustic wave perpendicular to the wall

When the wave propagates perpendicular to a wall, a standing wave is generated if all of the acoustic energy is reflected from the wall, as assumed here for convenience. A standing wave oriented perpendicular to the rigid wall (along the z-axis) is described as,

$$p_\infty(z_*, t_*) = 1 + p_{a*} \cos\left(k_*(z_* + \gamma)\right) \sin(w_* t_* + \phi_0) \tag{3.5.1}$$

Here, we choose $p_{a*} = 2.2$ for calculations in this section. Parametric studies are carried out in terms of the dimensionless standoff distance from a rigid boundary γ, membrane thickness d_s and shell viscosity μ_s.

3.5.1 Effect of standoff distance γ

Figure 3.24 shows the shapes for a coated bubbles with $\mu_s = 0.2$ Pa s, $d_s = 15$ nm, $G_s = 10$ MPa, $\phi_0 = \pi$, and $p_{a*} = 2.2$, at various standoff distance $\gamma = 0.75$, 1.5 and 3.0, respectively. The rest parameters are the same as in the case shown in figure reffigch2.3. As the bubble collapses nearer to the boundary, the jet forms early and is wider, because of the stronger Bjerknes force involved. As a result, the bubble volume at the time of liquid jet impact decreases with the standoff distance.

Figure 3.25 shows time histories of the global quantities for the above three cases. As shown in figure 3.25a, the expansion phase takes more than two thirds of the oscillation period. The maximum value of the equivalent bubble radius R_{eq*} increases with the standoff distance (figure 3.25a). As a result, more energy is absorbed from the acoustic wave as the bubble collapses further from the boundary (figure 3.25b). The maximum jet

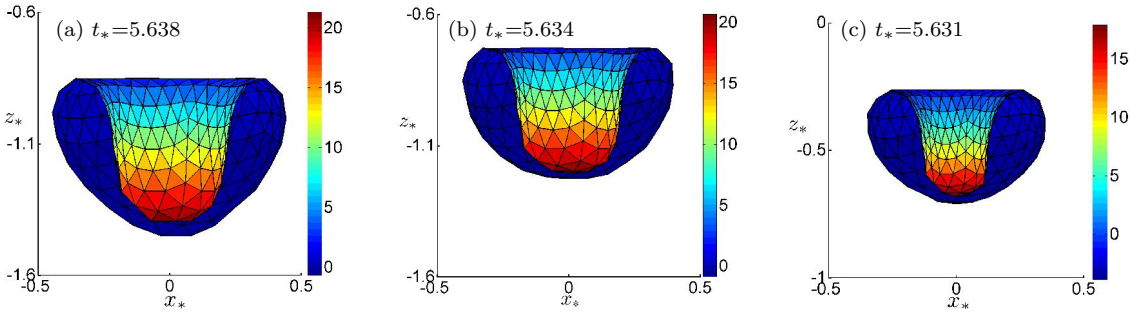

Figure 3.24: Bubble shapes at jet impact for a coated bubble near a wall in a standing wave for (a) $\gamma = 0.75$, (b) $\gamma = 1.5$, and (c) $\gamma = 3.0$. The parameters for these cases are $p_{a*} = 2.2$, $G_s = 10$ MPa, $d_s = 15$ nm, $\mu_s = 0.2$ Pa-s, and $\phi = \pi$.

velocity also increases with the standoff distance (figure 3.25d). However, the centroid movement along the z-axis z_{c*} (figure 3.25c) increases as the bubble collapses nearer to the wall.

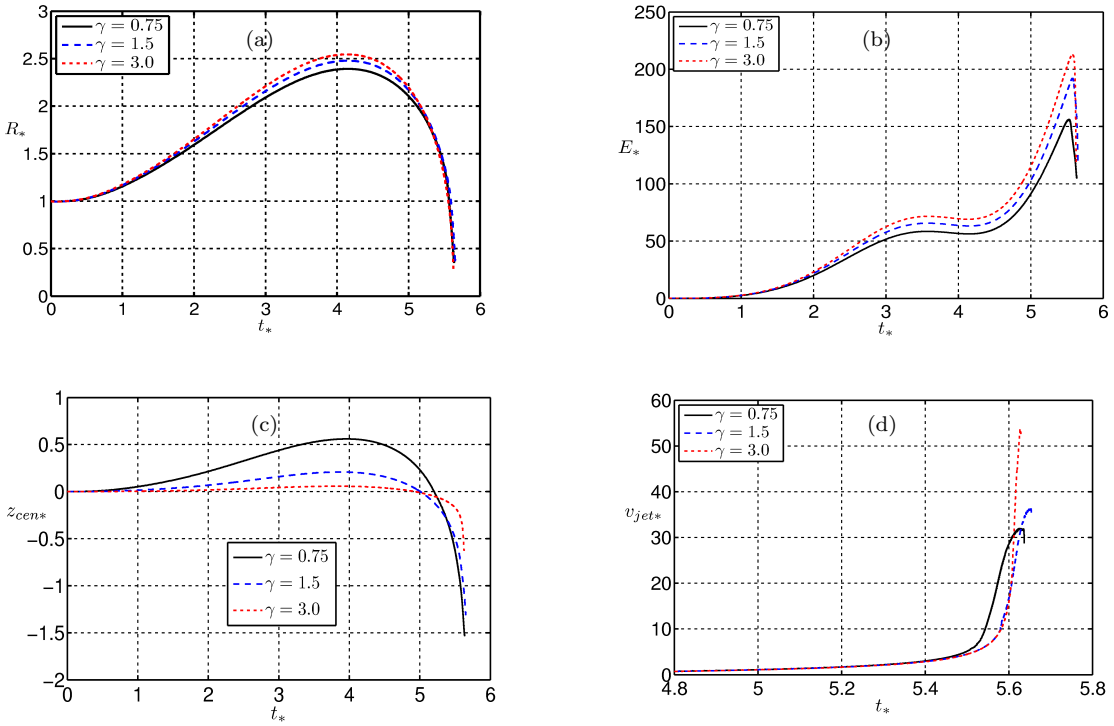

Figure 3.25: Time histories of (a) equivalent bubble radius R_{eq*}, (b) energy of the bubble system E_*, (c) z-component of the centroid z_{c*}, and (d) jet velocity v_{jet*} for the cases shown in figure 3.24.

3.5.2 Effect of shell thickness

Figure 3.26 shows bubble shapes at the time of jet impact for a bubble initiated at $\gamma = 3.0$ for three different shell thicknesses, $d_s = 0.0$, 5.0, and 10.0 nm, and the remaining parameters the same as in figure 3.24. (Note that a bubble with zero shell thickness is equivalent to a bubble without a shell.) The jet is wider for the smaller coating thickness.

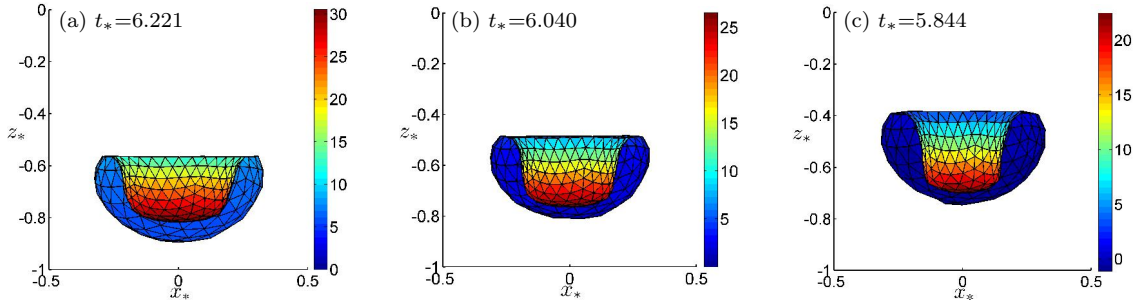

Figure 3.26: Bubble shapes at jet impact for a coated bubble near a wall in a standing wave for $\gamma = 3.0$ and shell thickness (a) $d_s = 0.0$ nm, (b) $d_s = 5.0$ nm, and (c) $d_s = 10.0$ nm, and the remaining parameters the same as in figure 3.24.

Figure 3.27 shows time histories of the global quantities for the cases shown in figure 3.26 and figure 3.24c. The maximum equivalent bubble radius decreases about 17% as shell thickness is increased from 0.0 to 15 nm (figure 3.27a). As shell thickness is increased, the oscillation amplitude reduces and the bubble absorbs less energy from the acoustic wave (figure 3.27b), migrates less to the boundary (figure 3.27c), and lower jet velocity (figure 3.27d).

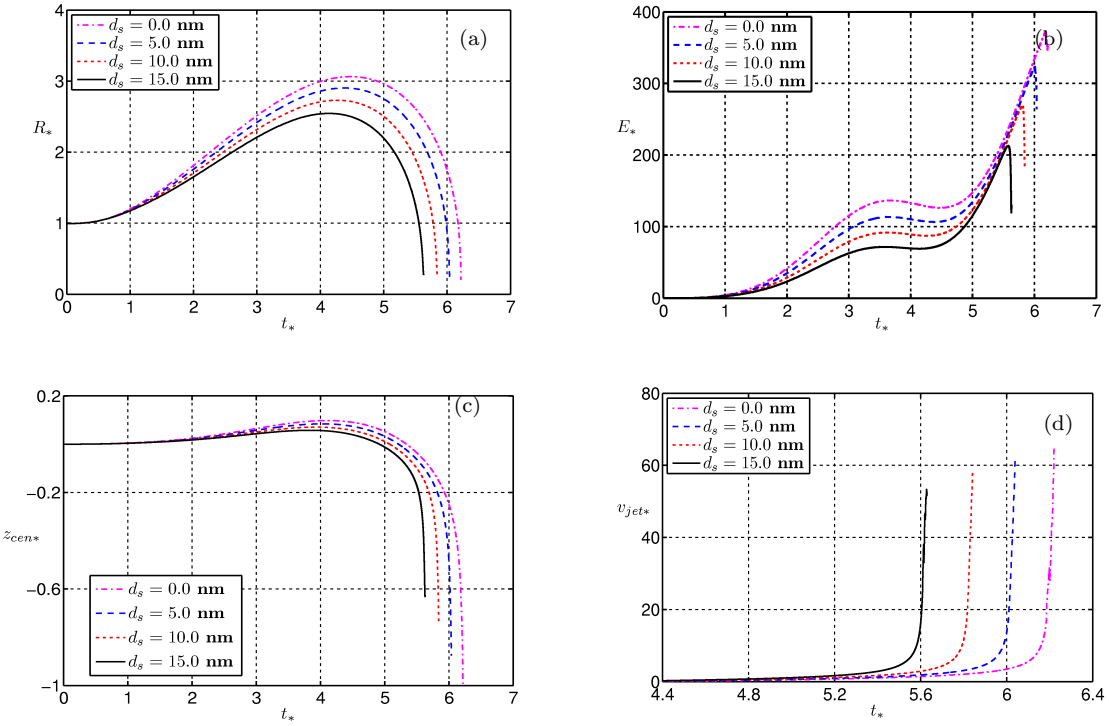

Figure 3.27: Time histories of (a) equivalent bubble radius R_{eq*}, (b) energy of the bubble system E_*, (c)z-component of the centroid z_{c*}, and (d)jet velocity v_{jet*}, for the cases shown in figure 3.26 and 3.24c.

3.5.3 Effect of shell viscosity

Figure 3.28 shows bubble shapes at the time of jet impact for a bubble initiated at $\gamma = 3.0$ for two different shell viscosities, $\mu_s = 0.0$ and 0.4 Pa s, and the remaining parameters the same as in figure 3.24. The bubble volume at the time of jet impact increases with shell viscosity while the jet becomes sharper.

Figure 3.29 shows time histories of the energy of the bubble system and the jet velocity for the cases shown in figures 3.28 and 3.24c. The results show that the maximum energy of the bubble system decreases about 10% and the jet velocity at the impact time decreases about 23%, when the shell viscosity increases from 0.0 to 0.4 Pa s. Our results (not included here) also show that the equivalent bubble radius, the centroid movement along the z-axis and the Kelvin impulse do not change significantly with the shell viscosity.

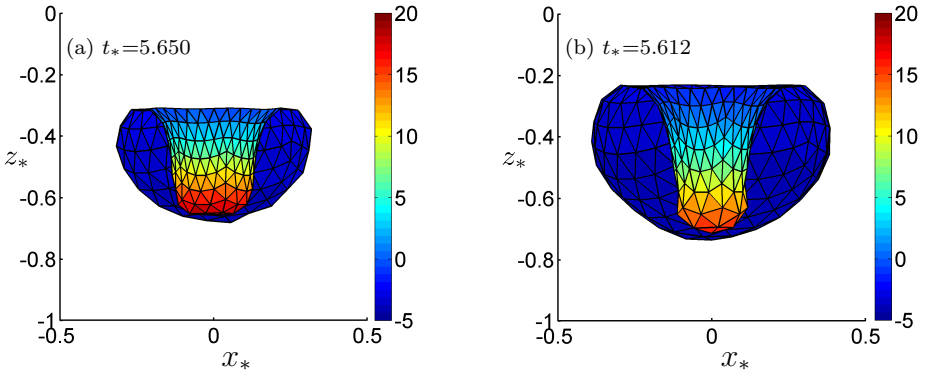

Figure 3.28: Bubble shapes at jet impact for a coated bubble near a wall in a standing wave for γ= 3.0 and shell viscosity (a) μ_s = 0.0 Pa-s and (b) μ_s = 0.4 Pa-s, and the remaining parameters the same as in figure 3.24.

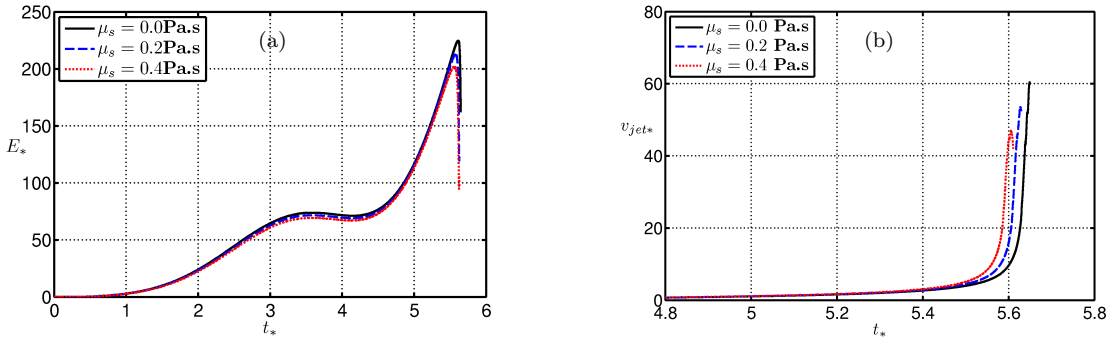

Figure 3.29: Time histories of (a) the energy of the bubble system E_*, and (b) the jet velocity v_{jet*}, for the cases shown in figures 3.28 and 3.24c.

3.6 Chapter summary

Ultrasound contrast agents (UCAs) are microbubbles stabilized with a shell typically of lipid, polymer or protein and are emerging as a unique tool for noninvasive therapies ranging from gene delivery to tumor ablation. While various models have been developed to describe the spherical oscillations of contrast agents, the treatment of nonspherical behavior has received less attention. However, the nonspherical dynamics of contrast agents are thought to play an important role in therapeutic applications, for example, enhancing the uptake of therapeutic agents across cell membranes and tissue interfaces, and causing tissue ablation. In this chapter, a model for contrast agent dynamics based

on the boundary integral method is described. The effects of the encapsulating shell are approximated by adapting Hoff's model for thin-shell contrast agents. A high-quality mesh of the bubble surface is maintained by implementing a hybrid approach of the Lagrangian method and elastic mesh technique. The numerical model agrees well with a modified Rayleigh-Plesset equation for coated spherical bubbles. Numerical analyses for the dynamics of UCAs in an infinite liquid and near a rigid wall are performed in parameter regimes of clinical relevance. The oscillation amplitude and period reduce significantly due to the coating. A bubble jet forms when the amplitude of ultrasound is sufficiently large, as occurs for bubbles without a coating; however, the threshold amplitude required to incite jetting increases due to the coating. When a UCA is near a rigid boundary subject to acoustic forcing, the jet is directed towards the wall if the acoustic wave propagates perpendicular to the boundary. When the acoustic wave propagates parallel to the rigid boundary, the jet direction has components both along the wave direction and towards the boundary that depend mainly on the dimensionless standoff distance of the bubble from the boundary. The jet directions for the coated and uncoated bubble are similar but the jet width and jet velocity are smaller for a coated bubble. The effects of shell thickness and viscosity are analyzed and determined to affect the bubble dynamics, including jet development.

Chapter 4

Three dimensional acoustic microbubble dynamics with viscous effects

4.1 Physical and mathematical model

Consider the dynamics of a microbubble near an infinite rigid plane wall subject to ultrasound, as shown in figure 2.1. A Cartesian coordinate system $o-xyz$ is adopted with the origin at the centre of the initial spherical bubble, the z-axis perpendicular to the wall and the x-axis along the wave direction. The far-field pressure p_∞ is thus modified to include a sinusoidal term,

$$p_\infty(x,t) = p_0 + p_a \sin(kx - \omega t), \tag{4.1.1}$$

where p_0 is the hydrostatic pressure, x is the coordinate along the propagation direction of the wave, t is time, and p_a, k and ω are the pressure amplitude, wavenumber and angular frequency of the acoustic wave, respectively.

We assume that the pressure p_b within the microbubble consists of the vapour pressure p_v which assumes it is fixed and small, and non-condensing gas pressure p_g:

$$p_b = p_v + p_g = p_v + p_{g0}\left(\frac{V_0}{V}\right)^{\kappa}, \tag{4.1.2}$$

where p_{g0} is the initial gas pressure of the bubble, V_0 is the initial bubble volume and κ is the ratio of specific heats of the gas.

We assume that the fluid surrounding the bubble is incompressible and the flow is irrotational. The fluid velocity $\boldsymbol{v}$ thus has a potential φ, $\boldsymbol{v} = \nabla\varphi$, which satisfies Laplace's equation, $\nabla^2\varphi = 0$. Using Green's second identity the potential φ may be represented as a surface integral over the bubble surface S as follows:

$$c(\boldsymbol{r})\varphi(\boldsymbol{r}) = \int_S \left(\frac{\partial\varphi(\boldsymbol{q})}{\partial n}G(\boldsymbol{r},\boldsymbol{q}) - \varphi(\boldsymbol{q})\frac{\partial G(\boldsymbol{r},\boldsymbol{q})}{\partial n}\right) dS(\boldsymbol{q}), \tag{4.1.3}$$

where $\boldsymbol{r}$ is the field point and $\boldsymbol{q}$ is the source point, $c(\boldsymbol{r})$ is the solid angle and $\boldsymbol{n}$ is the unit outward normal of the bubble surface S_b directed from liquid to gas. To satisfy the impermeable boundary condition on the wall, the Green function is given as follows,

$$G(\boldsymbol{r},\boldsymbol{q}) = \frac{1}{|\boldsymbol{r}-\boldsymbol{q}|} + \frac{1}{|\boldsymbol{r}-\acute{\boldsymbol{q}}|}, \tag{4.1.4}$$

where $\acute{\boldsymbol{q}}$ is the image of $\boldsymbol{q}$ reflected to the wall.

In the theory of viscous potential flow (VPF), viscous effects are calculated by including the viscous stresses on irrotational flows. The normal stress balance on the bubble surface, considering the surface tension and normal viscous stress, is given as follows:

$$p_L + 2\sigma\nabla\cdot\boldsymbol{n} - 2\mu\frac{\partial^2\varphi}{\partial n^2} = p_b, \tag{4.1.5}$$

where μ is viscosity of the liquid, p_L is the liquid pressure on the bubble surface, σ is the surface tension coefficient and $\nabla \cdot \boldsymbol{n}$ is the local mean curvature of the bubble surface. This is called the viscous potential flow solution (VPF) [51].

The tangential stress at the bubble surface should be zero as a result of the relatively low viscosity of the gas inside the bubble. However, the shear stress due to the irrotational velocity is non-zero. To resolve the above discrepancy a viscous pressure correction is introduced at the free surface by [51], which perform the equal power between the liquid to the gas. The power done by the liquid to the gas on a surface element dS on the free surface due to the irrotational shear stress is $dW = \boldsymbol{v}_\tau \cdot \boldsymbol{\tau}_s \, dS$ and the power done by the pressure correction P_{vc} is $dW = -v_n \, P_{vc} \, dS$. Thus we have,

$$-v_n \, P_{vc} = \boldsymbol{v}_\tau \cdot \boldsymbol{\tau}_s. \tag{4.1.6}$$

Joseph & Wang [51] introduced the pressure correction globally as follows,

$$\int_S -v_n \, P_{vc} \, dS = \int_S \boldsymbol{v}_\tau \cdot \boldsymbol{\tau}_s \, dS. \tag{4.1.7}$$

This model is called the viscous correction of VPF (VCVPF) [51]. The computation results in this chapter are based on VCVPF unless stated otherwise.

The relation (4.1.7) is not sufficient to calculate the viscous pressure correction P_{vc} at any point on the bubble surface. Joseph & Wang [51] assumed that the viscous correction pressure P_{vc} is proportional to the normal stress τ_n induced by the irrotational velocity,

$$P_{vc} = -C\tau_n = -2\mu C \frac{\partial^2 \varphi}{\partial n^2}, \tag{4.1.8}$$

where the constant C is unknown constant.

To calculate normal stress τ_n, $\frac{\partial^2\varphi}{\partial n^2}$ needed can be calculated as follows:

$$\frac{\partial^2\varphi}{\partial n^2} = \boldsymbol{n}\cdot\nabla\varphi_n = n_x\frac{\partial\varphi_x}{\partial n} + n_y\frac{\partial\varphi_y}{\partial n} + n_z\frac{\partial\varphi_z}{\partial n}, \tag{4.1.9}$$

where (n_x, n_y, n_z) are the components of the unit normal vector. φ_x, φ_y, and φ_z satisfy Laplace's equation since φ satisfies Laplace's equation. They thus satisfy the boundary integration equation (4.1.3). As a result, we can replace φ in (4.1.3) by φ_x, φ_y, and φ_z to formulate the boundary integral equations to find the terms $\partial\varphi_x/\partial n$, $\partial\varphi_y/\partial n$, and $\partial\varphi_z/\partial n$ respectively. Subsequently, $\frac{\partial^2\varphi}{\partial n^2}$ is calculated from (4.1.9).

It is inconvenient to calculate $\boldsymbol{\tau}_s$ directly in a three dimensional problem to obtain P_{vc} or C using (4.1.6) or (4.1.7). This is achieved indirectly by introducing that the rate of energy dissipation D in the irrotational flow is equal to the power on the bubble surface [131]

$$D = \int_S \boldsymbol{v}\cdot\boldsymbol{\sigma}\cdot\boldsymbol{n}\ dS = \int_S v_n\ \tau_n dS + \int_S \boldsymbol{v}_\tau\cdot\boldsymbol{\tau}_s\ dS = p_1 + p_2 = p_{total}, \tag{4.1.10}$$

where $\boldsymbol{\sigma}$ is stress tensor and p_1, p_2 and p_{total} are the powers of normal stress, shear stress and total power on the bubble surface respectively. Substituting (4.1.7) in (4.1.10)

$$D = \int_S v_n\ \tau_n dS + \int_S -v_n\ P_{vc}\ dS = p_{total}. \tag{4.1.11}$$

Substituting (4.1.8) in (4.1.11) yields,

$$D = (1+C)\int_S v_n\ \tau_n\ dS = 2\mu(1+C)\int_S \frac{\partial\varphi}{\partial n}\frac{\partial^2\varphi}{\partial n^2}dS, \tag{4.1.12}$$

where $\tau_n = 2\mu\ \partial^2\varphi/\partial n^2$ is the normal viscous stress.

On the other hand, the dissipation rate D can be approximated accurately in the surface integral for the irrotational flow [63],

$$\begin{aligned} D &\approx \mu \int_S \frac{\partial}{\partial n} |\boldsymbol{u}|^2 \, dS \\ &= 2\mu \int_S \left(\varphi_x \frac{\partial \varphi_x}{\partial n} + \varphi_y \frac{\partial \varphi_y}{\partial n} + \varphi_z \frac{\partial \varphi_z}{\partial n} \right) dS \end{aligned} \tag{4.1.13}$$

Using (4.1.12) and (4.1.13), one can have the unknown C as follows:

$$C = \frac{\displaystyle\int_S \left(\varphi_x \frac{\partial \varphi_x}{\partial n} + \varphi_y \frac{\partial \varphi_y}{\partial n} + \varphi_z \frac{\partial \varphi_z}{\partial n} \right) dS}{\displaystyle\int_S \frac{\partial \varphi}{\partial n} \frac{\partial^2 \varphi}{\partial n^2} dS} - 1. \tag{4.1.14}$$

The surface integrals of (4.1.14) are calculated by using the linear interpolation of φ_x, φ_y, φ_z,$\partial\varphi_x/\partial n$, $\partial\varphi_y/\partial n$, $\partial\varphi_n/\partial n$ and $\partial^2\varphi/\partial n^2$ on each triangular element on the bubble surface S.

With the pressure correction P_{vc} introduced, the normal stress balance on the bubble surface in VCVPF becomes,

$$p_L + P_{vc} + 2\sigma\kappa - 2\mu \frac{\partial^2 \varphi}{\partial n^2} = p_b, \tag{4.1.15}$$

We choose the reference length R_0 (initial radius of the bubble) and the reference pressure $\Delta p = p_0 - p_v$. The dimensionless kinematic and dynamic boundary conditions on the

bubble surface are as follows:

$$\frac{d\boldsymbol{r}_*}{dt_*} = \nabla\varphi_* \tag{4.1.16a}$$

$$\frac{d\varphi_*}{dt_*} = 1 + \frac{1}{2}\left|\nabla\varphi_*\right|^2 - \varepsilon\left(\frac{V_0}{V}\right)^{\kappa} - 2\frac{\nabla\cdot\boldsymbol{n}}{W_e} - \frac{2(1+C)}{R_e}\frac{\partial^2\varphi_*}{\partial n^2} + p_{a*}\sin(k_*x_* - \omega_*t_*), \tag{4.1.16b}$$

where the dimensionless variables are denoted with the subscript '*', the Reynolds number R_e and weber number W_e are defined as $R_e = R_0\sqrt{\Delta p\ \rho}/\mu$, $W_e = \Delta p R_0/\sigma$, where ρ and μ are density and viscosity of the liquid.

Following the convention the standoff distance is nondimensionalized with respect to the maximum equivalent bubble radius $R_{\max}$,

$$\gamma = \frac{s}{R_{\max}}, \tag{4.1.17}$$

where s is the distance from the bubble centre at inception to the wall (see figure 2.1).

4.2 Validations of the numerical model

4.2.1 Comparison with the Gilmore equation

We compare firstly with the spherical bubble theory for a spherical bubble oscillating in an infinite fluid. The parameters for the case are chosen as $R_0 = 4.5$ μm, $\varepsilon = 100$, $p_0 = 101.3$ kPa, $\rho = 999$ kg/m^3, $\kappa = 1.67$, $\sigma = 0.073$ N/m, and p_{a*}=0. A relatively small value of R_e=10 is chosen to see the viscous effects in terms of radial oscillation. Figure 4.1 compares the bubble radius time histories as determined from the BIM model and

Gilmore equation (GE). The BIM model agrees excellently with the GE for the first six cycles of oscillation. The amplitude and period of the oscillations decreases obviously due to the viscous damping effects. The maximum radius decreases with cycles and the minimum radius increase with cycles. The accumulation viscous effects are significant for microbubbles in multiple cycles of oscillation.

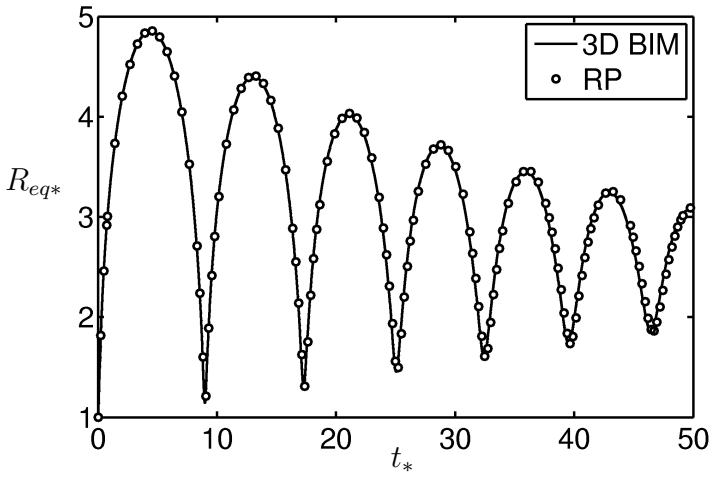

Figure 4.1: Comparison of the time histories of the bubble radius as determined from the 3D BIM model and Gilmore equation. The parameters used for the case are $R_0 = 4.5$ μm, $\varepsilon = 100$, $p_0 = 101.3$ kPa, $\rho = 999$ kg/m^3, $\kappa = 1.67$, $\sigma = 0.073$ N/m, p_{a*}=0 and $R_e = 10$.

4.2.2 Comparison with the experiment and the Navier-Stokes model

Ohl et al. [86] carried out carefully controlled experiments for laser-induced cavitation gas bubble dynamics near a rigid boundary in water at $\gamma = 1$ and $R_{\max}$=1 mm, capturing the detailed behaviour with a high-speed camera. Minsier et al. [83] simulated this case using the axisymmetric model for the Navier-Stokes equations, with the initial conditions of R_0 = 0.2 mm and $p_{g0} = 42$ bar, T_{amb}=300 K and T_{c0} =1998 K, where T_{amb} is the ambient temperature in the liquid and T_{c0} is the difference between the temperature at the centre of the bubble and the ambient temperature. The initial pressure inside the bubble is

determined such that the bubble reaches a maximum radius of 1 mm. We will compare the BIM with the experiment [86] and axisymmetric model based on the Navier-Stokes equation [83].

In the 3D BIM, the same initial pressure as [83] is chosen however a slightly bigger initial radius $R_0 = 0.224$ mm is used in order the maximum bubble radius reach 1 mm. This difference is due to the fact that some thermodynamic energy is set in the model by [83]. The ratio of specific κ in cavitation bubble was empirically determined in the literature [4] κ=1.4 and the rest of parameters are $p_0 = 101.3$ kpa, $\rho = 998$ kg m^{-1}, and $\mu_{\text{water}} = 0.001$ kg m^{-1} s^{-1}.

The experimentally bubble images were accurately reproduced by both the two numerical models during the expansion phase, collapse phase and jet formation as shown in figure 4.2. The rigid boundary at $\gamma = 1.0$ is located at the lower borders of the frames. The bubble first expands in a spherical shape except the lower part of the bubble surface is flattened by the rigid boundary at the end of expansion (figure 4.2A). It then collapses, with the lower part kept attached to the rigid boundary and the rest of the bubble surface collapses approximately spherically (figure 4.2B). A liquid jet forms and develops rapidly at the top of the bubble surface pointing to the rigid wall near the end of collapse (figure 4.2C). The oscillation periods of the two computational models are close to each other but both are slightly larger than the experimental data.

A. Expansion phase

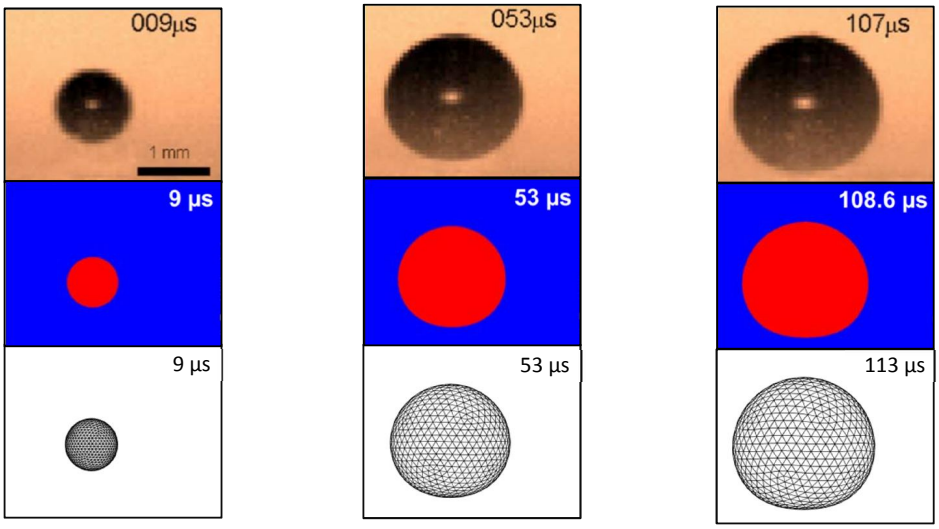

B. Collapse phase

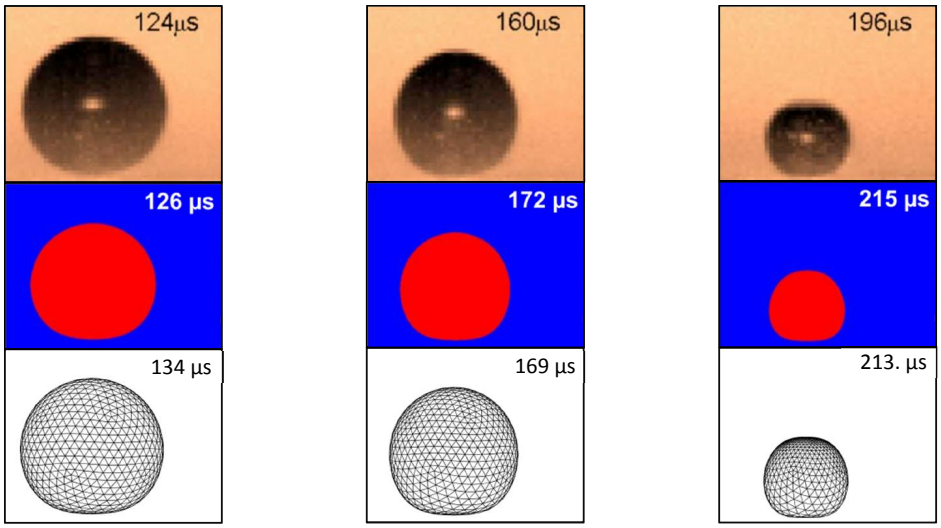

C. Collapse phase: jet formation

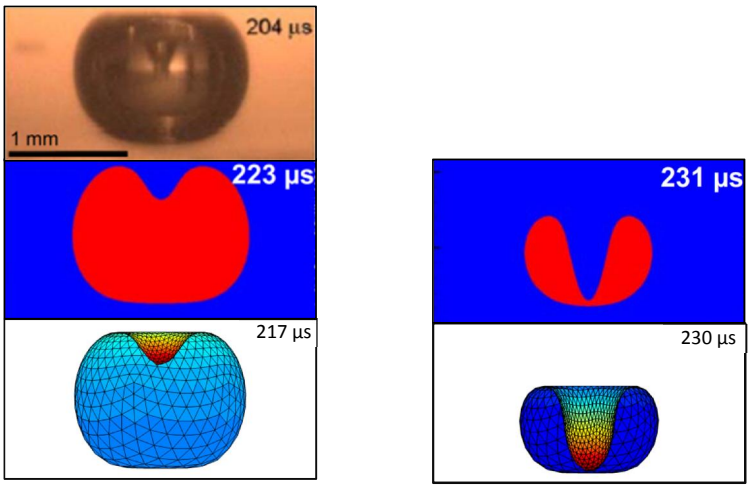

Figure 4.2: Comparison of the bubble shapes as obtained from the experiment ([86], in the first row of each phase), an axisymmetric model based on the Navier-Stokes equation ([83], in the second row) and the 3D BIM (in the third-row). The bubble shapes are shown during (A) the expansion phase, (B) the collapse phase and (C) the jet formation. The rigid boundary is located at the lower borders of frames. The parameters in the 3D BIM model are chosen as $R_0 = 0.224$ mm, p_{g0}=42 bar, $\gamma = 1.0$, $\mu_{\text{water}} = 0.001$ kg/(m s), $p_0 = 101.3$ Kpa, $\rho = 998$ kg m^{-1}, and $\kappa = 1.4$.

We next compare the 3D BIM based on the VCVPF with the axisymmetric model based on the Navier-Stokes equation [83] for bubble collapses in water with viscosity $\mu_{\text{water}} = 0.001$ kg/(m s) and in an oil with viscosity $\mu_{\text{oil}} = 0.05$ kg/(m s), respectively at very close to the rigid wall at $\gamma = 0.6$. Figures 4.3A, 4.3B show the bubble shapes in the collapse phase at typical time in water and oil, respectively. The two models are in good agreement in terms of timing, bubble shape and bubble volume in both liquids. The impact time and jet size and shape of the 3D BIM model agree well with the axisymmetric model based on the Navier-Stokes equation for both of the two cases.

A. Numerical results in water

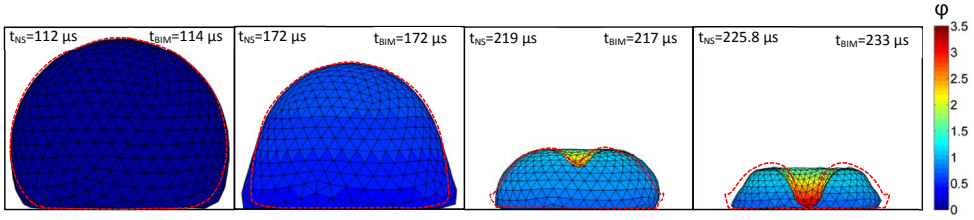

B. Numerical results in oil

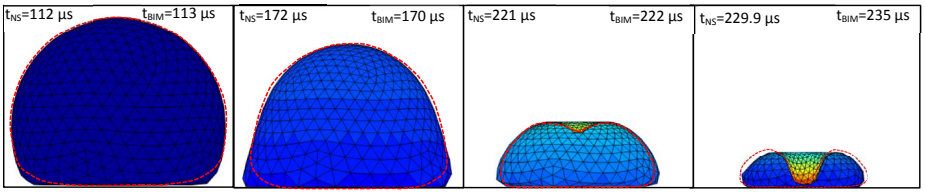

Figure 4.3: The comparison of the bubble shapes near a rigid boundary at $\gamma = 0.6$ calculated using the 3D BIM and axisymmetric model based on the Navier-Stokes equations [83], dash line) in the liquid with viscosity, (A)$\mu_{\text{water}} = 0.001$ kg/ (m s) and (B)$\mu_{\text{oil}} = 0.05$ kg/ (m s) respectively. The rigid boundary is located at the bottoms of the frames.

Figure 4.4 shows the comparison of the maximum jet velocities versus the dimensionless initial standoff distance γ of the bubble in oil from the rigid boundary, obtained using the axisymmetric model of the Navier-Stokes equation [83] and the 3D BIM model. We have consider three 3D BIMs based on the classical potential flow theory (PF), the viscous potential flow theory (VPF), considering the normal viscous stress of the potential flow,

and the viscous correction of VPF (VCVPF). The results of all the three BIM models agree with the Navier-Stokes equation in magnitude and trend in general. The maximum jet velocity reduces due to the normal viscous stress and reduces further due to the viscous pressure correction. The results of VCVPF are most closer to the results of the Navier-Stokes equation among the three BIM models.

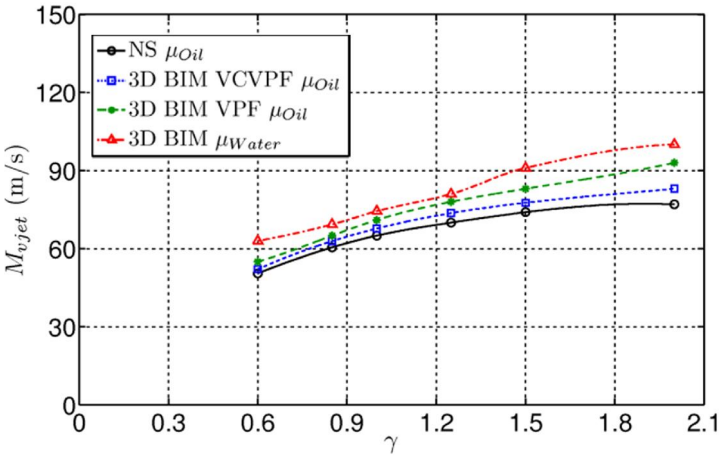

Figure 4.4: Comparison of the maximum jet velocities versus the dimensionless stand-off distance γ for a bubble in oil from a rigid wall, obtained using the axisymmetric model based on the Navier-Stokes equation [83] , 3D BIM models based on the potential flow theory (PF), the viscous potential flow theory (VPF) and the viscous correction of VPF (VCVPF).

4.3 Microbubble dynamics near a wall subject to ultrasound parallel to the wall

We analyze the dynamics of a microbubble near a rigid boundary subject to ultrasound propagating parallel to the boundary. The bubble is assumed at the equilibrium pressure $\varepsilon = 1 + 2/W_e$ initially and the acoustic parameters are chosen as $p_{a*} = 1.6$ and $f = 300$ kHz. The standoff distance of the bubble from the boundary is chosen as $\gamma = 12.0$, 4.0 and 1.0, respectively. The parameters used are $\kappa = 1.4$, $\sigma = 0.055$ N/m, $p_0 = 100$ kPa, ρ

= 1000 kg/m^3, $R_0 = 4.5$ μm. The parameters are chosen for blood relevant to biomedical applications. The corresponding Reynolds number is $R_e = 13$. Two other values of the Reynolds number $R_e = 50$ and ∞ have been examined, to investigate the influence of viscous effects.

A high-speed liquid jet develops towards the end of collapse as shown in figure 4.5. The bubble is subject to the Bjerknes force due to the acoustic wave along the wave direction and the second Bjeknes force pointing to the boundary. The liquid jet is along the wave direction at $\gamma = 12$ (figure 4.5A), as the effect of the boundary is negligible in this case. The jet is along the bisector of the two Bjerknes forces at γ= 4.0 (figure 4.5B) when the two forces are comparable, and is pointing to the boundary at $\gamma = 1.0$ as the second Bjerknes force is predominant in this case (figure 4.5C).

In all cases of γ, the jet becomes thinner when the Reynolds number R_e decreases from 50 to 13, while it does not change significantly when R_e decreases from ∞ to 50. The jet becomes thinner due to the viscous effects, which are not significant as R_e is larger than 50. The oscillation period reduces slightly with the viscous effects.

Figure 4.6 depicts the time histories of the equivalent bubble radius, jet velocity, centroid movement along the x-axis and z-axis, energy E_* and magnitude of Kelvin impulse I_{K*} of the bubble, for the cases shown in figure 4.5B. The maximum bubble radius increases about only 6% when R_e increases from 13 to ∞ (figure 4.6a). The maximum jet velocity increases substantially from 930 m/s to 1310 m/s with R_e (figure 4.6b). The centroid movement, the energy and the Kelvin impulse of the bubble increase with R_e (Figures 4.6c-f). These trends are associated the strong viscous damping effects at a lower R_e number.

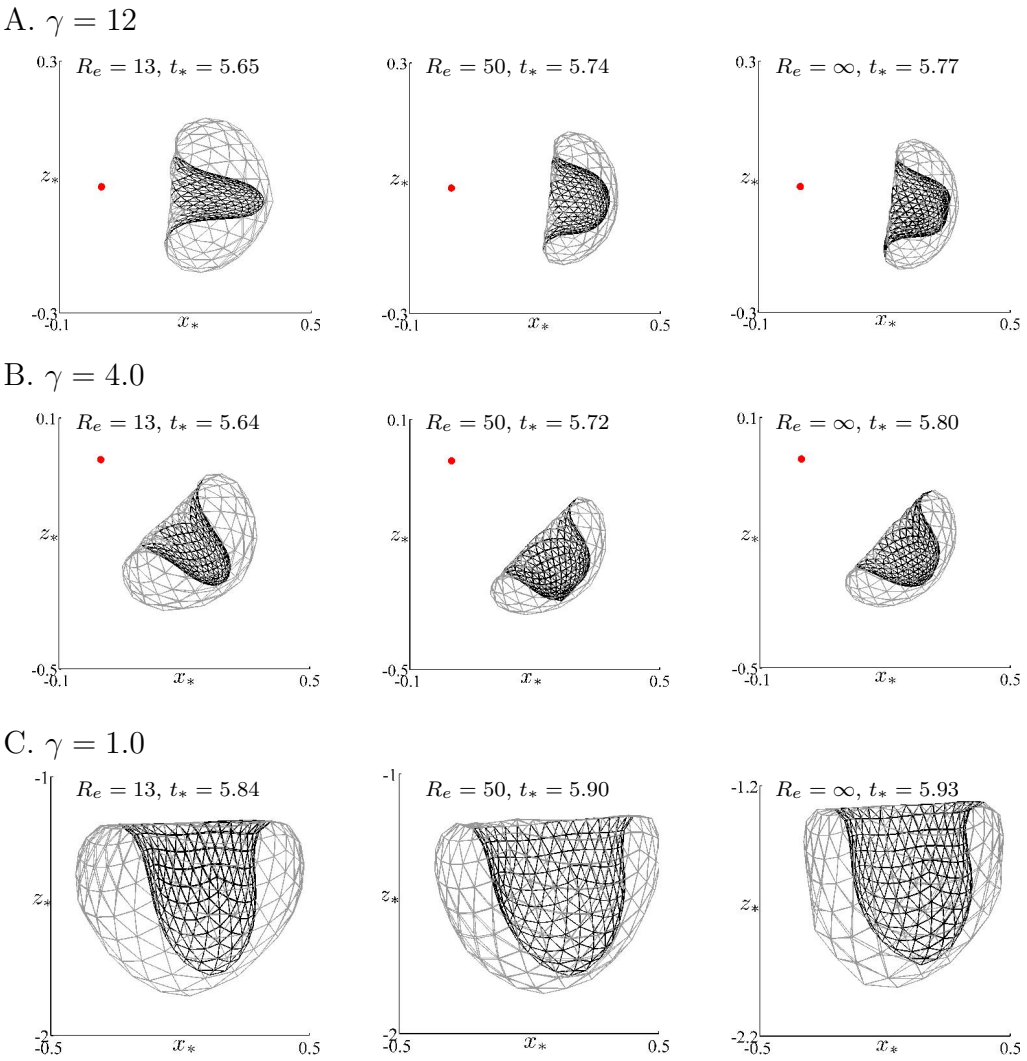

Figure 4.5: Bubble shapes at jet impact for a bubble near a wall at the dimensionless standoff distances (A) $\gamma = 12$, (B) $\gamma = 4.0$, (C) $\gamma = 1.0$, subject to ultrasound propagating parallel to the wall at $p_{a*} = 1.6$ and $f = 300$ kHz, at the Reynolds number $R_e = 13$, 50, and ∞. The remaining parameters are $c = 1540$ m/s, $\kappa = 1.4$, $\sigma = 0.055$ N/m, $p_0 = 100$ kPa, $= 1000$ kg/m^3, $R_0 = 4.5$ μm.

Similar trends have been observed at $\gamma = 12.0$ and 1.0 in table 4.1, where $R_{\max*}$, V_{jet*}, X_{c*}, Z_{c*}, I_{kmax*}, and E_{max*} are the maximum equivalent bubble radius, jet velocity, centroid movement along x-axis, centroid movement along z-axis, magnitude of the Kelvin impulse, and energy at jet impact, respectively. The maximum equivalent bubble radius $R_{\max*}$ reduce about 6% as R_e changes from ∞ to 13 at both γ due to the viscous effects. The central movement reduces with the viscous effects. I_{kmax*} reduces about 35% and 40%

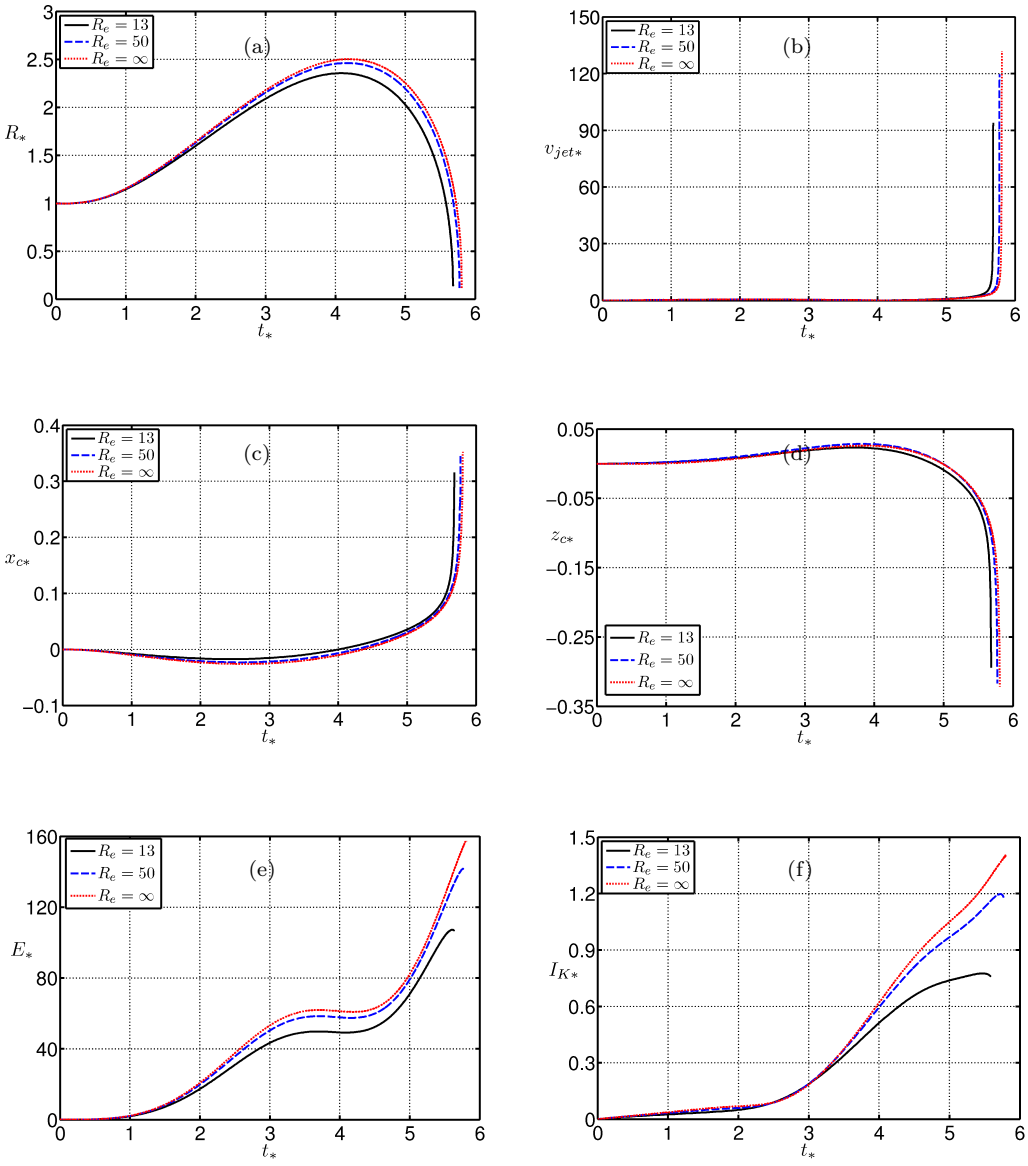

Figure 4.6: Time histories of (a) the equivalent bubble radius R_*, (b) jet velocity v_{jet*}, (c) x-component of the centroid x_{c*}, (d) z-component of the centroid z_{c*}, (e) energy E_*, and (f) magnitude of the Kelvin impulse I_{K*} of the bubble for the cases shown in figure 4.5B.

at γ=12 and γ=1 respectively with the change in R_e. E_{max*} also reduces about 38% and 25% with the change in R_e for both γ respectively. The changes for all the quantities are relatively large as R_e changes from 50 to 13, but much smaller R_e changes from ∞ to 50.

R_e	$\gamma = 12.0$						$\gamma = 1.0$					
	$R_{\max*}$	V_{jet*}	X_{c*}	Z_{c*}	I_{kmax*}	E_{max*}	$R_{\max*}$	V_{jet*}	X_{c*}	Z_{c*}	I_{kmax*}	E_{max*}
13	2.385	103.9	0.374	-0.036	0.71	102.0	2.253	26.3	0.071	-2.0315	4.38	92.1
50	2.496	138.2	0.398	-0.041	0.96	146.8	2.347	28.2	0.103	-2.1971	6.53	114.8
∞	2.537	146.5	0.426	-0.067	1.09	163.1	2.381	28.3	0.101	-2.0315	7.30	122.0

Table 4.1: The maximum equivalent bubble radius R_m, and jet velocity v_{jet*}, bubble centroid displacement z_{c*} along the z-axis, magnitude of Kelvin impulse I_{k*}, and bubble energy E_* at jet impact for the cases of shown in figure 4.5(A, C).

4.4 Microbubble dynamics near a wall subject to ultrasound perpendicular to the wall

When the wave propagates perpendicular to a wall, a standing wave is generated if all of the acoustic energy is reflected from the wall, as assumed here for convenience. A standing wave oriented perpendicular to the rigid wall (along the z-axis) is described as,

$$p_\infty(z_*, t_*) = 1 + p_{a*} \cos(k_*(z_* + \gamma)) \sin(\omega_* t_* + \phi_0). \tag{4.4.1}$$

Here, parametric studies are carried out in terms of the dimensionless standoff distance from a rigid boundary $\gamma = 2.0$, 1.0 and the Reynolds numbers $R_e = 13$, 50, ∞; with wave pressure amplitude p_{a*}=1.4. The rest parameters are the same as in the section 4.3.

Figure 4.7 shows bubble shapes at impact time at $\gamma = 2.0$, 1.0 with $R_e = 13$, 50 and ∞. In all cases the jet directed to the rigid boundary. The jet becomes sharper due to viscous effect at $\gamma = 2.0$ (figure 4.7A). In both cases the bubble migration to the wall is slowed down obviously due to the viscous effects.

Table 4.2 provides the maximum equivalent bubble radius $R_{\max*}$, and the jet velocity V_{jet*}, centroid movement along z-axis towards the rigid wall Z_{c*}, magnitude of Kelvin impulse

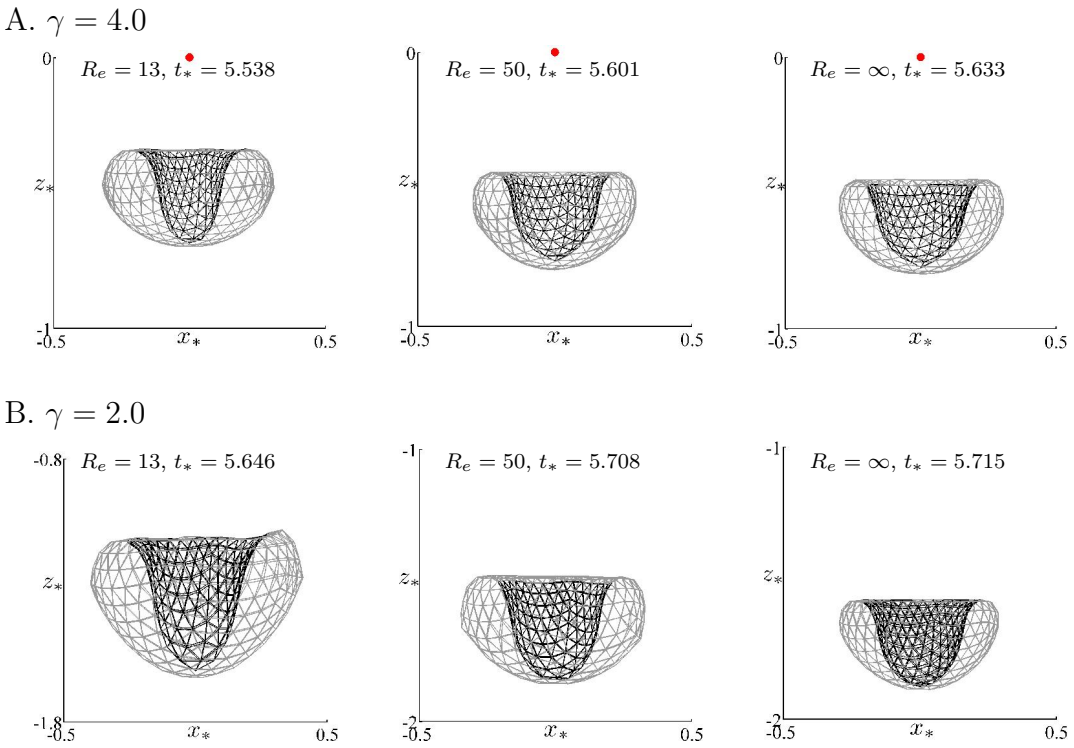

Figure 4.7: Bubble shapes at jet impact for a bubble near a wall at the dimensionless standoff distance subject to in a standing wave (A) $\gamma = 2$ and (B) γ =1, subject to ultrasound propagating perpendicular to the wall at the Reynolds number $R_e = 13$, 50 and ∞. The remaining parameters are the same as in figure 4.5.

I_{kmax*}, and bubble energy E_{max*} at jet impact for the cases of figure 4.7. The $R_{\max*}$ and V_{jet*} reduce about 6% and 17% respectively, as R_e changes from ∞ to 13 at both γ due to the viscous effects. The Z_{c*} is also about 18% and 22% decrease at γ=2.0 and 1.0 respectively. The rate is larger at γ=1 as the wall attraction is stronger. The magnitude of the Kelvin impulse I_{kmax*} and bubble energy E_{max*} at jet impact reduce also due to the viscous effects. The changes for all the quantities are relatively large as R_e changes from 50 to 13, but much smaller Re changes from ∞ to 50. This suggests the viscous effects are small as R_e is 50 or larger.

R_e	$\gamma = 2.0$					$\gamma = 1.0$				
	$R_{\max *}$	V_{jet*}	Z_{c*}	I_{kmax*}	E_{max*}	$R_{\max *}$	V_{jet*}	Z_{c*}	I_{kmax*}	E_{max*}
13	2.07	32.50	-0.70	1.05	61.35	2.02	22.61	-1.85	2.72	56.80
50	2.17	38.72	-0.83	1.83	82.32	2.11	27.56	-2.29	4.32	74.94
∞	2.20	39.17	-0.85	2.17	90.85	2.14	28.01	-2.37	4.92	85.05

Table 4.2: The maximum equivalent bubble radius R_m, and jet velocit v_{jet*}, bubble centroid displacement z_{c*} along the z-axis, magnitude of Kelvin impulse I_{k*}, and bubble energy E_* at jet impact for the cases of shown in figure 4.7.

4.5 Chapter summary

Microbubble dynamics subject to ultrasound are associated with important applications in biomedical ultrasonics, sonochemistry and cavitation cleaning. This chapter investigates the phenomenon using the boundary integral method based on the viscous potential flow theory. The viscous effects are incorporated into the model through including the normal viscous stress in the dynamic boundary condition at the bubble surface. The viscous correction pressure of Joseph (2004, 2007) is implemented to resolve the discrepancy between the non-zero shear stress of the irrotational flow at a free surface and the physical boundary condition of zero shear stress. The model agrees well with the Gilmore equation for a spherical bubble oscillating in a viscous liquid for several cycles. It agrees with both the experimental data and the axisymmetric simulation based on the Navier-Stokes equation for transient bubble dynamics near a rigid boundary. We further analyze microbubble dynamics near a rigid boundary subject to a ultrasound wave travelling perpendicular and parallel to the boundary, respectively, in parameter regimes of clinical relevance. The viscous effects in acoustic microbubble dynamics are analyzed in terms of the jet velocity, centroid movement, Kelvin impulse, bubble energy and bubble volume, etc.

Chapter 5

Simulation of three-dimensional toroidal bubble using vortex ring model

5.1 BIM modelling for singly connected bubbles

Consider the dynamics of a gas bubble adjacent an inclined wall, as shown in figure 5.1. A Cartesian coordinate system $O - xyz$ is adopted with the origin at the centre of the initial spherical bubble and the z-axis along buoyancy force. The separation of the centre of the initial spherical bubble from the wall is denoted as s. The angle between the wall with the x-axis is β.

We assume that the liquid surrounding the bubble is inviscid, incompressible and the liquid flow is irrotational. The fluid velocity $\boldsymbol{v}$ thus has a potential φ, $\boldsymbol{v} = \nabla\varphi$, which satisfies Laplace's equation, $\nabla^2\varphi = 0$. The potential φ may be represented as a surface integral over the bubble surface S_b as follows, using Green's second identity:

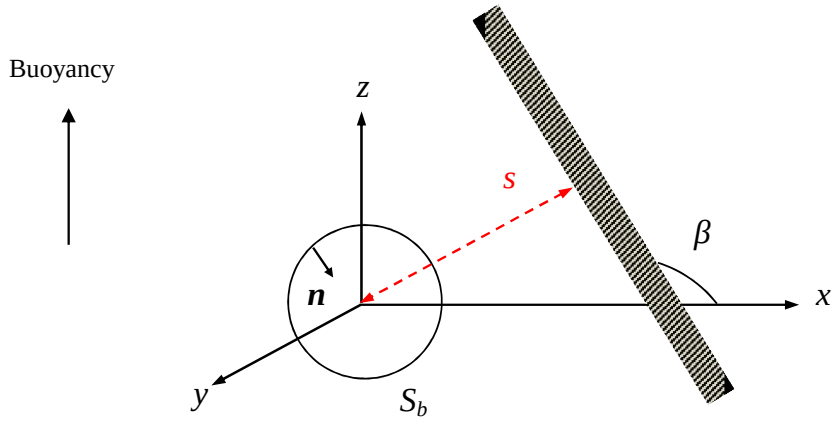

Figure 5.1: Configuration and coordinate system for the gas bubble near a rigid wall.

$$c(\boldsymbol{r})\varphi(\boldsymbol{r}) = \int_{S_b} \left(\frac{\partial \varphi(\boldsymbol{q})}{\partial n} G(\boldsymbol{r}, \boldsymbol{q}) - \varphi(\boldsymbol{q}) \frac{\partial G(\boldsymbol{r}, \boldsymbol{q})}{\partial n} \right) dS(\boldsymbol{q}), \tag{5.1.1}$$

where $\boldsymbol{r}$ is the field point and $\boldsymbol{q}$ is the source point, $c(\boldsymbol{r})$ is the solid angle and $\boldsymbol{n}$ is the unit outward normal of the bubble surface S_b.

To satisfy the impermeable boundary condition on the wall, the Green function is given as follows,

$$G(\boldsymbol{r}, \boldsymbol{q}) = \frac{1}{|\boldsymbol{r} - \boldsymbol{q}|} + \frac{1}{|\boldsymbol{r} - \acute{\boldsymbol{q}}|}, \tag{5.1.2}$$

where $\acute{\boldsymbol{q}}$ is the image of $\boldsymbol{q}$ reflected to the wall.

Assuming that the expansion and contraction of the bubble gas is adiabatic, the liquid pressure p_L on the bubble surface is given by,

$$p_L = p_v + p_{g0} \left(\frac{V_0}{V} \right)^{\kappa} \quad \text{on} \quad S_b \tag{5.1.3}$$

where p_v is vapour pressure, p_{g0} is the initial gas pressure of the bubble, V is the bubble volume and V_0 is its initial value, and κ is the ratio of specific heats of the gas. The the

surface tension coefficient is neglected in this study.

The kinematic and dynamic boundary conditions on the bubble surface S_b are as follows,

$$\frac{d\boldsymbol{r}}{dt} = \nabla\varphi \quad \text{on} \quad S_b, \tag{5.1.4}$$

$$\frac{d\varphi}{dt} = \frac{p_\infty - p_L}{\rho} + \frac{1}{2}\left|\nabla\varphi\right|^2 - gz \quad \text{on} \quad S_b \tag{5.1.5}$$

where p_∞ is the hydrostatic pressure, g is the gravitational acceleration, and d/dt the material derivative following particles on the bubble surface.

We choose the reference length R_m (maximum radius of the bubble) and the reference pressure $\Delta p = p_\infty - p_v$. The dimensionless dynamical boundary condition 5.1.5 becomes,

$$\frac{d\varphi}{dt} = 1 + \frac{1}{2}\left|\nabla\varphi\right|^2 - \delta^2 z - \varepsilon\left(\frac{V_0}{V}\right)^\kappa \quad \text{on} \quad S_b \tag{5.1.6}$$

where $\delta = \sqrt{\rho g R_{\max}/\Delta p}$ is the buoyancy parameter, $\varepsilon = p_{g0}/\Delta p$ is the normalized initial bubble pressure, and $\gamma = s/R_{\max}$ is the dimensionless separation distance of the bubble from the wall.

5.2 3D vortex ring model for toroidal bubbles

5.2.1 Impact modelling

When a bubble collapses nonspherically, a liquid-jet forms and impacts on the opposite bubble surface. Jet impact often occurs at a single point, since the curvature radius of the jet front is usually smaller than the curvature radius of the opposite bubble wall at the impact point. Although jet impact may be more complex in reality, we restrict it to this

idealized model. In fact jet impact may occur at a small area when the curvature radii of the jet and the opposite surface at the impact point are equal or at a ring when the jet front is flat.

A numerical cut is needed to transform a singly connected bubble to a toroidal bubble. We firstly sort two impact nodes, N on the jet tip and S on the opposite bubble face (as represented in white dot in figure 5.2a). To make this sorting automatically, the following two conditions are used: (i) the distance between the two nodes S and N are less than, say $0.5d_s$, where d_s is the average element size of the bubble surface. and (ii) the angle between the normal vectors at the two nodes is larger than $\pi/2$, to make sure that they are on the opposite sides of the bubble surface. In figure 5.2a only two ring of neighbour elements for the impact points N and S presented. The angle of view in figure 5.2a, b is 45° and the distance between impacts points in figure 5.2a exaggerated for clarification.

The nodes S and N and their surrounded elements (filled in red in figure 5.2a) will be deleted to create a hole (figure 5.2b). A local coordinate $O-XYZ$ is introduced with its origin at the node N, and its Z-axis passing the node S. Denote the surrounding node set to the node N as $N_1N_2\cdots N_m$ and the surrounding node set to the node S as $S_1S_2\cdots S_n$. If the numbers of the two grid sets do not match, say $m<n$, additional nodes are inserted along the longest line segments among $N_1N_2\cdots N_m$ to bring the numbers m and n to par. The two surrounding set of nodes are reordered according to the azimuth (angle θ), and named $n_1n_2\cdots n_n$ and $s_1s_2\cdots s_n$ respectively. A new set of nodes is then created to replace both of them as follows,

$$\boldsymbol{x}^k_{new} = \left(\boldsymbol{x}_{n_k} + \boldsymbol{x}_{s_k}\right)/2, \qquad k = 1, 2, \cdots, n \tag{5.2.1}$$

The liquid hole through the bubble is thin at the beginning of the toroidal phase. A much finer mesh is thus needed for toroidal bubble. We divide each triangular element of the

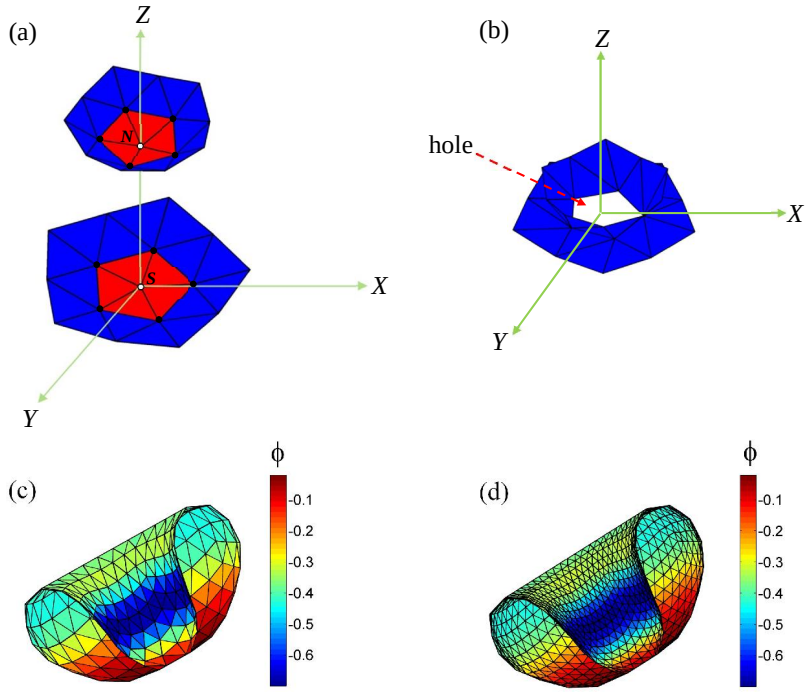

Figure 5.2: Illustration of the numerical transition of bubble shape and the vortex-ring model: (a) Before impact, two rings of the surrounding elements to the impact points N and S, (b) After impact, the surrounding elements of the hole, (c) the surface mesh of a toroidal bubble with remaining potential ϕ, and (d) the refined surface mesh of the toroidal bubble by splitting each elements into four elements.

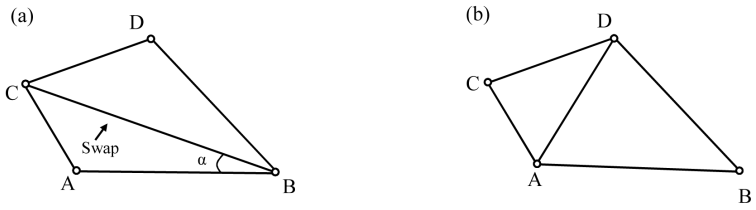

Figure 5.3: Swapping of two triangles ABC and CBD sharing an edge CB to two triangles ABD and ADC: (a) before edge swapping (b) after edge swapping.

mesh after jet impact into 4 smaller triangles as shown in figures (5.2c) and (5.2d). We use the edge swapping to improve the mesh, as shown in figure 5.3. It changes the shared edge of a pair of adjacent triangles without moving the nodes to improve the quality of the triangular element. The optimal shape of a triangular element is equilateral triangle.

Consider a triangular elements ABC with minimum angle α (figure 5.3a). Searching for a triangle say BCD, which shares edge BC with the triangle ABC . The new triangles ACD and ABD are created by swapping the edge BC by AD (figure 5.3b), if all angles in the new triangles greater than α. The number of connected nodes around considered node may be changed. In this study we restrict each node have 4 to 8 neighbour nodes.

5.2.2 Vortex ring model

After the jet impacts the opposite bubble surface the liquid domain becomes doubly-connected, so that the solution to Laplace's equation becomes non-unique. The doubly-connected domain can be made singly-connected by, for example, using a branch cut [2] or a vortex sheet [135, 134, 133]. Wang, et al. [124] developed a vortex ring model for toroidal bubbles, which avoids the treatment of the branch-cut.

In the vortex ring model, a vortex ring is put inside the toroidal bubble after jet impact and its strength Γ is equal to the jump of the potential φ across the contact point at the time of impact. Thus,

$$\Gamma = \int_c \nabla\varphi \cdot d\boldsymbol{r} = \varphi_N - \varphi_S, \tag{5.2.2}$$

where φ_N and φ_S are potentials at the impact point. The circulation Γ is invariant in time as the potential satisfies Laplace's equation. The potential φ is now decomposed as follows,

$$\varphi = \varphi_{vr} + \phi, \tag{5.2.3}$$

where φ_{vr} is the potential of the vortex-ring. With the potential jump being accounted by the vortex ring using (5.2.2), the remnant potential ϕ is continuous in the flow field. The induced velocity $\boldsymbol{v}_{vr}$ of the vortex ring can be obtained analytically using the Biot-Savart law, and the corresponding velocity potential is further obtained by the line integral of

the velocity from the far field, to let the potential of the vortex ring to vanish at infinity.

Using (5.1.4, 5.1.5,5.1.6) and 4.1.3, one can obtain the boundary value problem for the remnant potential ϕ as follow,

$$\nabla^2\phi = 0, \tag{5.2.4a}$$

$$\frac{d\boldsymbol{r}}{dt} = \boldsymbol{v}_{vr} + \nabla\phi, \quad \text{on} \quad S_b \tag{5.2.4b}$$

$$\frac{d\phi}{dt} = 1 - \boldsymbol{v}_{vr}\cdot(\boldsymbol{v}_{vr} + \nabla\phi) + \frac{1}{2}\left|\boldsymbol{v}_{vr} + \nabla\phi\right|^2 - \varepsilon\left(\frac{V_0}{V}\right)^{\kappa} - \delta^2 z. \quad \text{on} \quad S_b \tag{5.2.4c}$$

The above governing equations for the remnant potential ϕ are in the same form as the equations for the potential φ for the pre-toroidal bubble. ϕ thus can be solved using the BIM approach developed for φ.

5.2.3 Calculation of the potential due to a vortex ring

The velocity field induced by a vortex ring $\boldsymbol{v}_{vr}$ is given by the Biot-Savart law,

$$\boldsymbol{v}_{vr}(\boldsymbol{r}) = \nabla\varphi_{vr} = \frac{\Gamma}{4\pi}\oint_c \frac{d\boldsymbol{c}(\boldsymbol{q})\times(\boldsymbol{r}-\boldsymbol{q})}{|\boldsymbol{r}-\boldsymbol{q}|^3}, \tag{5.2.5}$$

where $d\boldsymbol{c}$ is along the vortex ring c, $\boldsymbol{r}$ is the field point.

Zhang et al. [135] calculate the potential due to a vortex ring based on the result in Milne and Thompson [82] using the solid angle formula,

$$\varphi_{vr}(\boldsymbol{r}) = \frac{\Gamma}{4\pi}\int_{S_c} \frac{\partial G(\boldsymbol{r},\boldsymbol{q})}{\partial n} dS(\boldsymbol{q}), \tag{5.2.6}$$

where Γ is the circulation of a vortex ring, S_c is any surface enclosed by the vortex ring. This integral has a discontinuity across the disk S_c, and so using this approach directly

leads to unacceptable errors at nodes close to or on the discontinuity.

The precise location of the vortex ring is immaterial in principle as long as it lies completely within the toroidal bubble. It is chosen at the mean position of the cross-section of the bubble surface at $\theta =$ constant. The vertex ring $\boldsymbol{C}(\theta)$ can be expressed as follows in the local cylindrical coordinate $OXYZ$:

$$\boldsymbol{C}(\theta) = (C_x(\theta), C_y(\theta), C_z(\theta)), \quad \theta \in [0, 2\pi]. \tag{5.2.7}$$

The potential velocity due vortex ring is calculated by integrating of the velocity of (5.2.5) in the local coordinate system $OXYZ$. The potential due to the vortex ring at any point $\boldsymbol{X} = (X, Y, Z)$ can be calculated from the line integration along the Z-axis from either (X, Y, ∞) or $(X, Y, -\infty)$ to (X, Y, Z),

$$\begin{aligned}
\varphi_{vr}(X, Y, Z) &= \int_{\pm\infty}^{Z} \boldsymbol{v}_{vr}(\boldsymbol{X}) \cdot \boldsymbol{K} dZ \\
&= \frac{\Gamma}{4\pi} \int_{\pm\infty}^{Z} \oint_{C(\theta)} \frac{d\boldsymbol{C}(\theta) \times (\boldsymbol{X} - \boldsymbol{C}(\theta))}{|\boldsymbol{X} - \boldsymbol{C}(\theta)|^3} \cdot \boldsymbol{K} dZ \\
&= \frac{\Gamma}{4\pi} \oint_{C(\theta)} \int_{\pm\infty}^{Z} \frac{d\boldsymbol{C}(\theta) \times (\boldsymbol{X} - \boldsymbol{C}(\theta))}{|\boldsymbol{X} - \boldsymbol{C}(\theta)|^3} \cdot \boldsymbol{K} dZ,
\end{aligned} \tag{5.2.8}$$

where the order of integration is changed since the curve $\boldsymbol{C}(\theta)$ for the line integral does not depends on Z and the integral limits for integration in Z does not depends on θ. The integrant function can be expressed as,

$$\frac{d\boldsymbol{C}(\theta) \times (\boldsymbol{X} - \boldsymbol{C}(\theta))}{|\boldsymbol{X} - \boldsymbol{C}(\theta)|^3} \cdot \boldsymbol{K} = \frac{dC_X R_Y - dC_Y R_X}{(R_X^2 + R_Y^2 + R_Z^2)^{3/2}}, \tag{5.2.9}$$

where $d\boldsymbol{C}(\theta) = (dC_X, dC_Y, dC_Z)$ on the curve $\boldsymbol{C}(\theta)$ does not depend on Z; $\boldsymbol{R} = \boldsymbol{X} - \boldsymbol{C}(\theta) = (R_X, R_Y, R_Z) = (X - C_X, Y - C_Y, Z - C_Z)$. R_X and R_Y do not depend on Z but $R_Z = Z - C_Z$ depends on Z. Thus we have,

$$
\begin{aligned}
&\int_{\pm\infty}^{Z} \frac{d\boldsymbol{C}(\theta) \times (\boldsymbol{X} - \boldsymbol{C}(\theta))}{|\boldsymbol{X} - \boldsymbol{C}(\theta)|^3} \cdot \boldsymbol{K}\, dZ \\
&= (dC_X R_Y - dC_Y R_X) \int_{\pm\infty}^{Z} \frac{dZ}{(R_X^2 + R_Y^2 + R_Z^2)^{3/2}} \\
&= (dC_X R_Y - dC_Y R_X) \int_{\pm\infty}^{R_Z} \frac{dR_Z}{(R_X^2 + R_Y^2 + R_Z^2)^{3/2}} \\
&= (dC_X R_Y - dC_Y R_X) \left(\frac{R_Z}{(R_X^2 + R_Y^2)\,(R_X^2 + R_Y^2 + R_Z^2)^{1/2}} \right) \Bigg|_{R_Z = \pm\infty}^{R_Z = R_Z} . \\
&= \left(\frac{dC_X R_Y - dC_Y R_X}{R_X^2 + R_Y^2} \right) \left(\frac{R_Z}{(R_X^2 + R_Y^2 + R_Z^2)^{1/2}} \mp 1 \right) .
\end{aligned}
\tag{5.2.10}
$$

This yields,

$$
\varphi_{vr}^{\pm}(\boldsymbol{X}) = \frac{\Gamma}{4\pi} \oint_{\boldsymbol{C}(\theta)} \left(\frac{dC_X R_Y - dC_Y R_X}{R_X^2 + R_Y^2} \right) \left(\frac{R_Z}{(R_X^2 + R_Y^2 + R_Z^2)^{1/2}} \mp 1 \right) , \tag{5.2.11}
$$

where "+" of "±" is corresponding for the line integration from $(X, Y, +\infty)$ to (X, Y, Z) and "-" the line integration from $(X, Y, -\infty)$ to (X, Y, Z). To determine the correct value of the potential, the bubble surface is divided in two sub surfaces named $\mathrm{S_U}$ and $\mathrm{S_L}$ as clarified in the figure 5.4. Therefore, in the equation 5.2.11 "-" of "±" is used for $X \in \mathrm{S_U}$ and "+" of "±" $X \in \mathrm{S_L}$.

Suppose that the simple closed curve $C = C_1 - C_2 + C_3$, where C_1, C_2, and C_3 are oriented

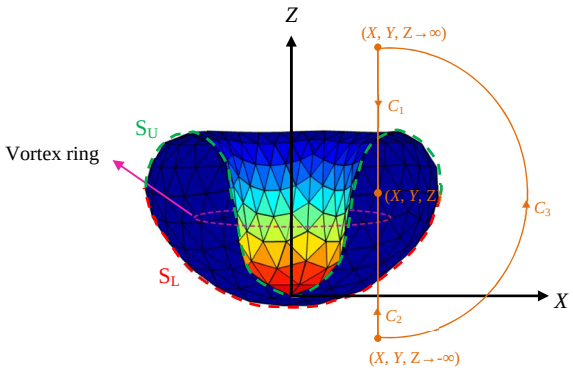

Figure 5.4: Illustration of calculation of the potential due vortex ring and position of vortex ring.

curves from $(X, Y, Z \to \infty)$ to (X, Y, Z), from $(X, Y, Z \to -\infty)$ to (X, Y, Z), and from $(X, Y, Z \to -\infty)$ to $(X, Y, \to \infty)$ respectively, and C_3 is half of a circle, as shown in figure 5.4. We have,

$$\int_{C_1} \nabla\varphi_{vr} \cdot d\boldsymbol{l} = \varphi_{vr}^{+}(\boldsymbol{X}), \quad \int_{C_2} \nabla\varphi_{vr} \cdot d\boldsymbol{l} = \varphi_{vr}^{-}(\boldsymbol{X}), \quad \text{and} \int_{C_3} \nabla\varphi_{vr} \cdot d\boldsymbol{l} = 0. \tag{5.2.12}$$

Thus,

$$\begin{aligned} \varphi_{vr}^{+}(\boldsymbol{X}) - \varphi_{vr}^{-}(\boldsymbol{X}) &= -\frac{\Gamma}{4\pi} \oint_{\boldsymbol{C}(\theta)} \left(\frac{dC_X R_Y - dC_Y R_X}{R_X^2 + R_Y^2} \right) \\ &= \begin{cases} 0 & \text{as} \quad \sqrt{X^2 + Y^2} \geq C(\theta) \\ \Gamma & \text{as} \quad \sqrt{X^2 + Y^2} < C(\theta) \end{cases} \end{aligned} \tag{5.2.13}$$

Suppose (C_X^k, C_Y^k, C_Z^k) $k = 1, 2, \cdots M$ are points along the vortex ring $\boldsymbol{C}$. Then, the line

integral in 5.2.11 may be calculated numerically as follows:

$$\varphi_{vr}^{\pm}(\boldsymbol{X}) = \frac{\Gamma}{4\pi}\sum_{k=1}^{M-1}\frac{(Y-C_X^k)(C_X^{k+1}-C_X^k)-(X-C_Y^k)(C_Y^{k+1}-C_Y^k)}{(X-C_X^k)^2+(Y-C_Y^k)^2}$$
$$\left(\frac{(Z-C_Z^k)}{\sqrt{(X-C_X^k)^2+(Y-C_Y^k)^2+(Z-C_Z^k)^2}}\mp 1\right) \quad (5.2.14)$$

5.3 Validations of the numerical model

5.3.1 Comparison with experiment

The first validation case is to compare the 3D BIM results with an experimental data of Lindau & Lauterborn [74] for a laser-generated bubble near a wall at the maximum radius $R_{\max} = 1.5$ mm and the dimensionless standoff distance $\gamma = 0.8$. Other computational parameters are chosen following Pearson et al. [89] as $\varepsilon = 600$, $\delta = 0.0$ and $\kappa = 1.4$.

Figure 5.5 shows the 3D BIM results for the motion of a cavitation bubble at typical times. The bubble is initially with a very high pressure and expands spherically, reaching its maximum volume at $t_* = 1.11$ (figure 5.5b), when the lower part of the bubble surface is flattened against the wall (figure 5.5c). Towards the last stage of collapse a liquid jet starts at $t_* = 2.06$ (figure 5.5d), which develops rapidly and impacts shortly at the opposite bubble surface at $t_* = 2.168$ (figure 5.5e). The bubble becomes toroidal after jet impact (figure 5.5e) and collapse continuously from figures 5.5f 5.5i. As the lower side of the bubble ring is in contact with the wall, the jet pushes out of the bubble ring after it impacts on the wall.

Figure 5.6 shows the experimental images of Lindau & Lauterborn [74] at the corresponding time steps, where jet impact is visible around frames 4-5. The bubble evolves to a circular

bubble ring with a circular cross section as noticed in the calculation.

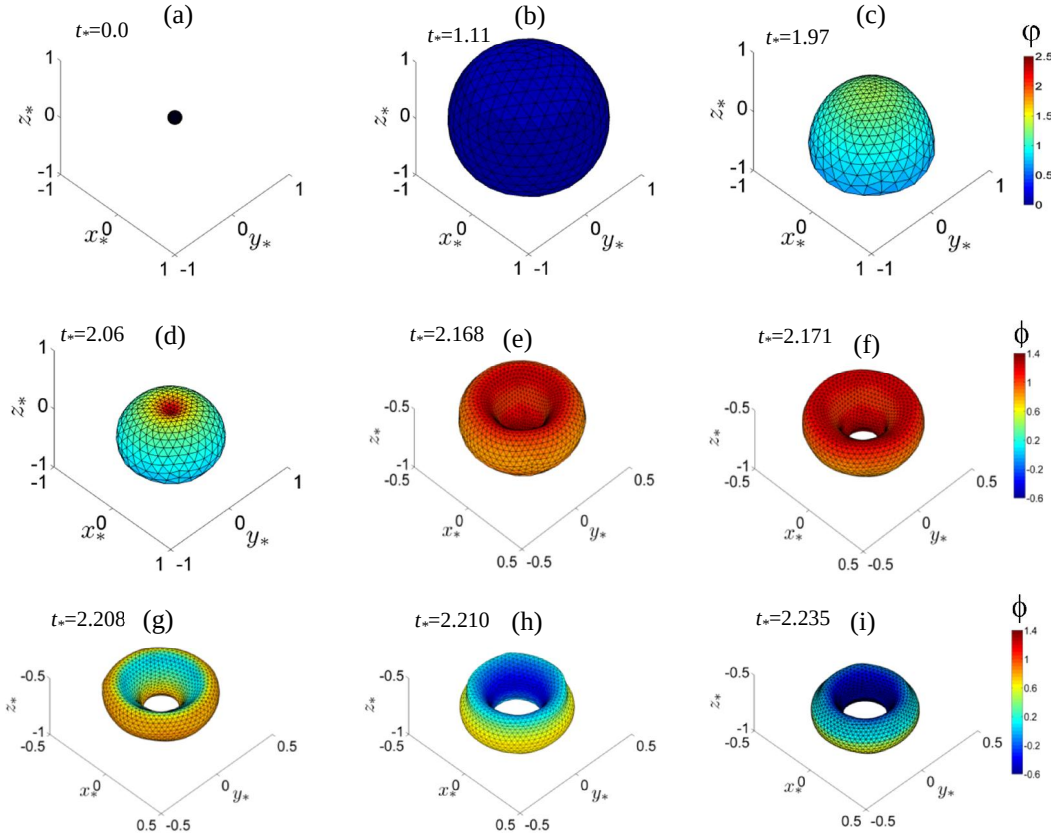

Figure 5.5: Evolution of a bubble near a rigid boundary characterized by $\varepsilon = 600$, $\kappa = 1.4$, $\delta = 0$, $\gamma = 0.8$ with the angle of elevation is 45°.

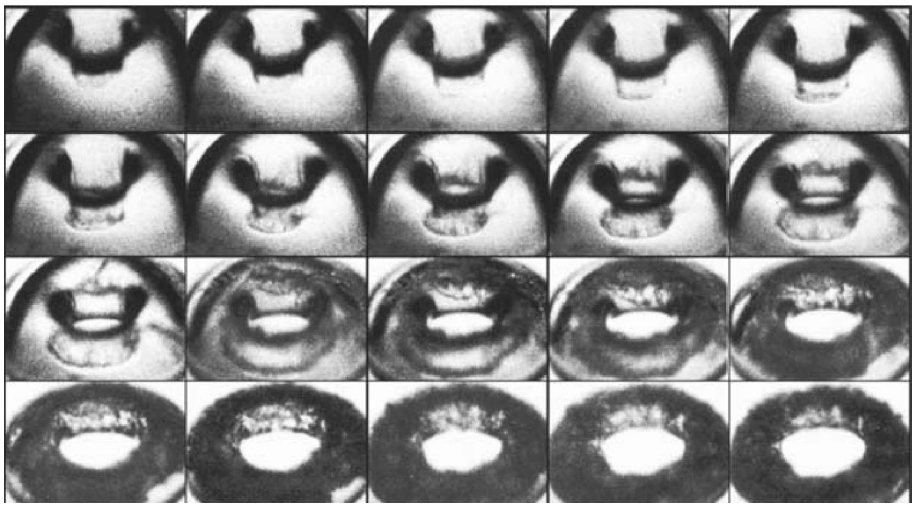

Figure 5.6: The final stages of collapse of a laser-generated bubble near a rigid boundary characterized by $R_{\max} = 1.5$ mm, and $\gamma = 0.$ 8 with the angle of elevation is 45° [74]. The fame size is 1.68 mm × 1.15 mm, interframe time 1 μs, exposure time 200 ns.

5.3.2 Comparison with axisymmetric model

We next compare the 3D BIM with the axisymmetric BIM (Wang et al. [126]) for a bubble near a rigid wall characterized by $\gamma = 2$, $\varepsilon = 100$ and $\delta = 0.0$. The jet impact occurs in 3D model at $t_* = 2.118$ with a circulation Γ = -4.1. The corresponding results obtained using the axisymmetric BIM code are $t_* = 2.126$ and Γ = -4.3. The small differences in the timing and the circulation should be due to the lower resolution used in the 3D model.

Figure 5.7 compares the bubble shapes at typical times between the two models, where the results of the axisymmetric BIM are shown in dash line. The bubble shapes of the 3D results agree well with the asymmetric BIM at jet impact (figure 5.7a), and during the early rebounding phase (figure 5.7b). Figure 5.7c shows the agreement between for the bubble radius history between the 3D BIM (dotted) and the axisymmetric BIM.

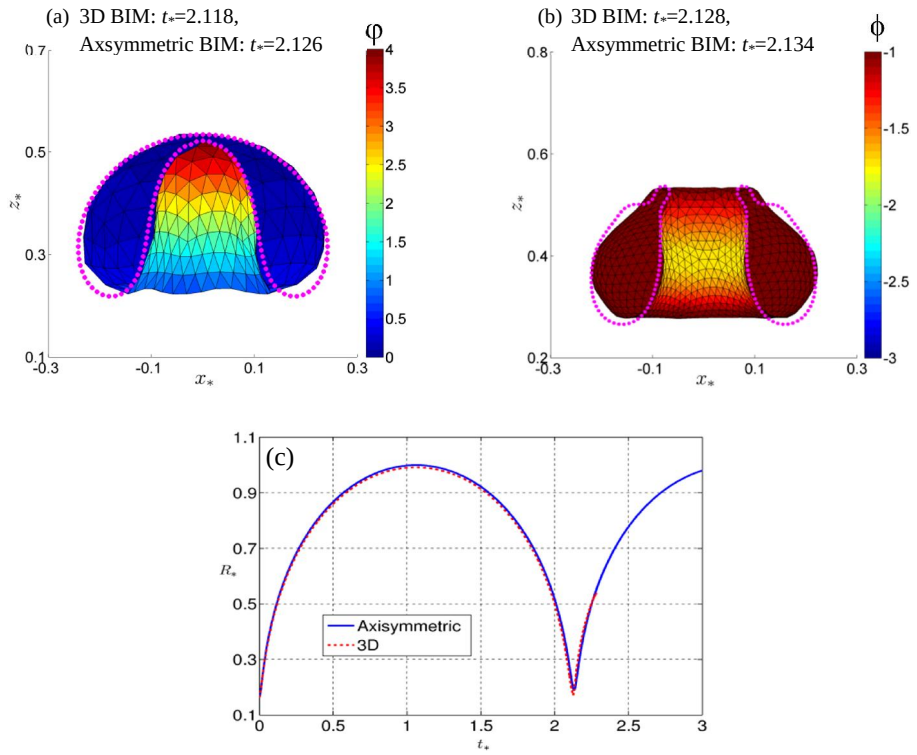

Figure 5.7: The comparison of the 3D bubble shapes and axisymmtric profile during (a) jet impact, (b) toroidal phase, at a typical times. (c) The comparesion of the bubble radius history between the two models. The case charecterised by ε=100, δ=0.0, and γ=2.0.

5.4 Computational results

Best & Blake [3] proposed a criterion for determining the directions of the jet and bubble migration for bubble dynamics near a rigid boundary using the Kelvin impulse theory. They observed that the buoyancy force and the Bjerknes attraction of the rigid boundary are comparable in magnitude when $\gamma\delta = 0.442$. We simulated bubble dynamics near a vertical rigid wall, for three cases at $\gamma = 3$ and $\varepsilon = 100$ with three different buoyancy parameters $\delta = 0.1$, 0.147, and 0.2. These three cases correspond to $\gamma\delta$= 0.3, 0.442 and 0.6, respectively.

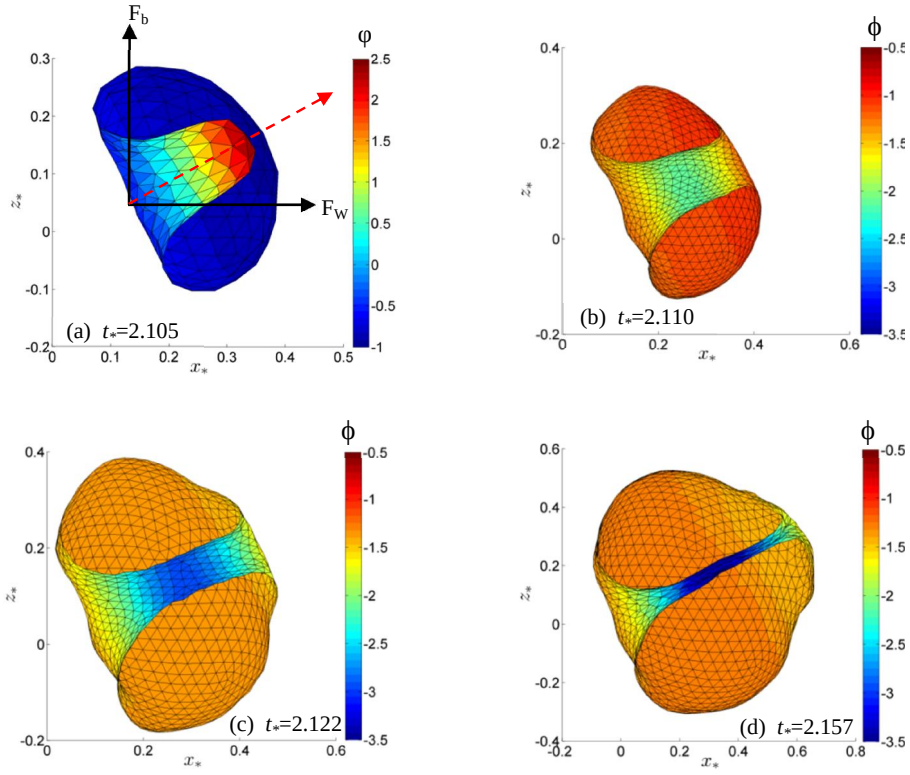

Figure 5.8: The toroidal bubble dynamics near a vertical wall characterised by $\gamma = 3.0$, $\delta = 0.1$, and $\varepsilon = 100$: (a) at jet impact, (b) at the minimum bubble volume, and during the rebounding phase from (b-d).

The bubble shapes at $\gamma\delta = 0.3(< 0.442)$ at a typical times steps are shown in figure 5.8. The jet impacts the opposite bubble surface at $t_* = 2.105$ (figure 5.8a). A vortex ring is

put in the bubble ring with the circulation of $\Gamma = 3.43$. The bubble continues collapsing for a short period, reaching the minimum volume at $t_* = 2.110$ (figure 5.8b). It then rebounds with the bubble jetting becomes narrow (figure 5.8c, 5.8d). The jet direction is about 30° to the horizontal plane, as shown in figure 5.8a.

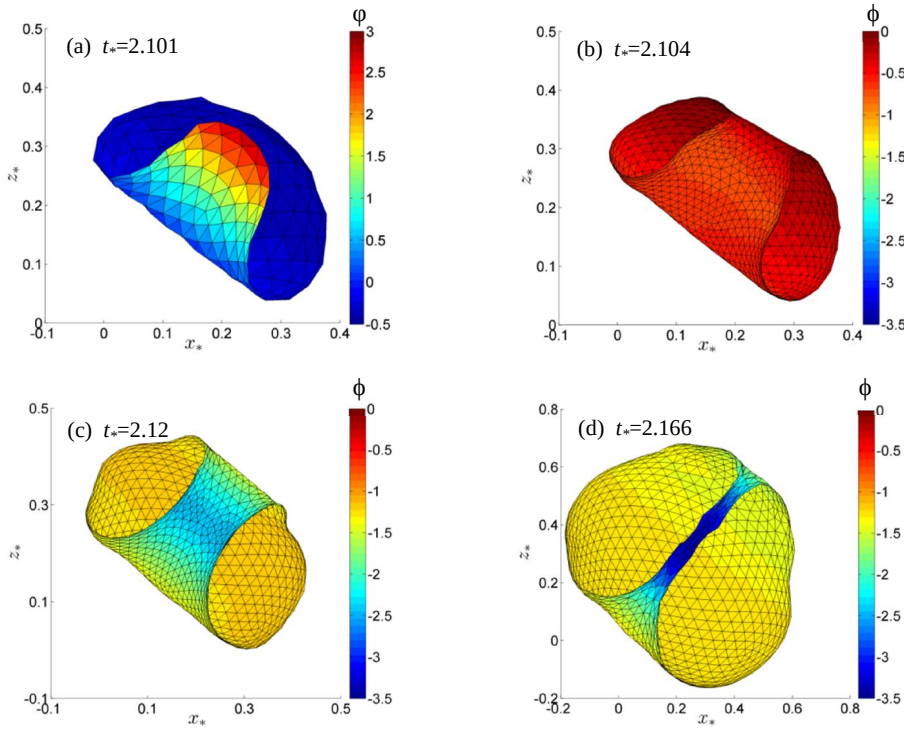

Figure 5.9: The toroidal bubble dynamics near a vertical wall characterised by $\gamma = 3.0$, $\delta = 0.147$, and $\varepsilon = 100$: (a) at jet impact and (b) at the minimum bubble volume, and during the rebounding phase from (b-d).

The bubble shapes at typical times for the case at $\gamma\delta \approx 0.442$ are shown in figure 5.9. The jet impacts the opposite bubble surface at $t_* = 2.101$ (figure 5.9a). The circulation of the vortex ring for this case is Γ=3.37. The bubble collapses continuously for a short period after jet impact, reaching minimum volume t_*=2.104 (figure 5.9b). The bubble then rebounds and the jet becomes thin (figures 5.9c, d). The jet direction is about 50° to the horizontal plane.

The bubble shapes at typical times for the case at $\gamma\delta = 0.6(> 0.442)$ are depicted in figure

5.10. A wide liquid jet impacts on the opposite bubble surface towards the end of collapse at t_*=2.100 (figure 5.10a). The circulation in this case is Γ=3.2. The jet direction is with the angle about 70° to the horizontal plane, since the stronger buoyancy force is associated with this case comparing with the last two cases. The bubble reaches minimum volume in very short period time after jet impact at t_*=2.122. The bubble then rebounds and jet becomes thin (figures 5.10c, d).

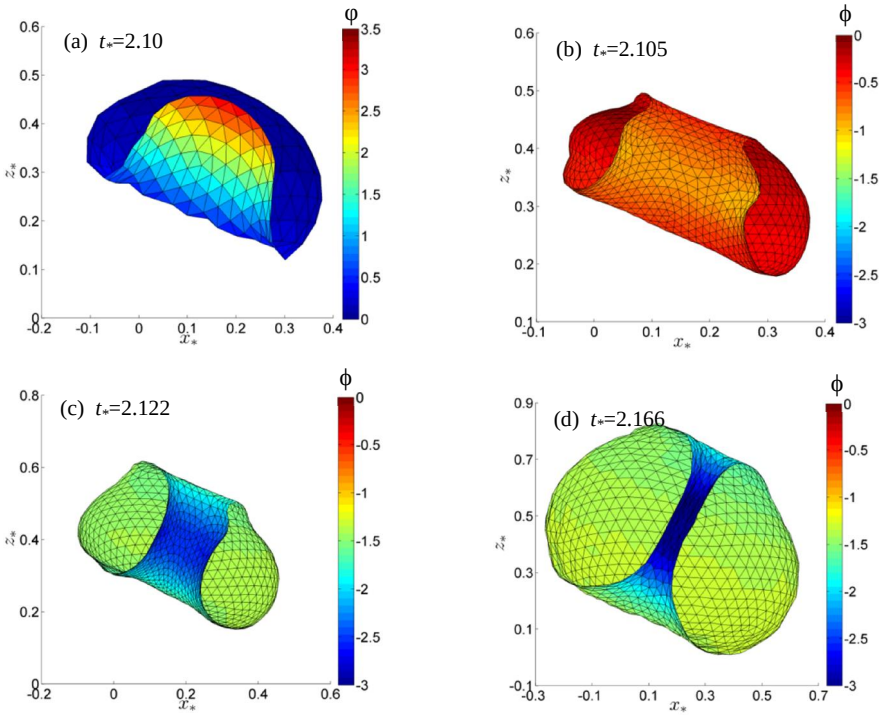

Figure 5.10: The toroidal bubble dynamics near a vertical wall characterised by $\gamma = 3.0$, $\delta = 0.2$, and $\varepsilon = 100$: (a) at jet impact, (b) at the minimum bubble volume, and during the rebounding phase from (b-d).

5.5 Chapter summary

It is challenging to simulate three dimensional toroidal bubble dynamics, which are associated with strong numerical instabilities due to jet impact, topological transition, and bubble rebound. A few of developments are described in this chapter to improve the vortex ring model for three dimensional toroidal bubbles. A high quality mesh of the bubble surface is maintained by implementing a new hybrid approach of the Lagrangian method and elastic mesh technique. The transform from a singly connected bubble to a toroidal bubble is performed automatically. A finer mesh is generated by splitting each of triangles into four triangles after jet impact, to describe the local geometry associated a hole through the bubble penetrated by the bubble. The potential due to a vortex ring is calculated by using the Biot-Savart law where the integral from the infinite to the point considered is performed analytically. We evaluate the numerical model by comparing with the axisymmetric BIM and the experiment result. We analyse toroidal bubble dynamics subject to buoyancy near a vertical wall, including jet impacting and rebounding toroidal bubbles with oblique jetting.

Chapter 6

Summaries, conclusions and future work

6.1 Summaries and conclusions

In this thesis, a robust computational model has been developed for simulation of three-dimensional microbubble dynamics near a rigid wall subjected to high intensity ultrasound based on the potential flow theory and the boundary integral method. A few techniques were implemented to model the associated violent collapse. The bubble surface and potential distribution on it were updated using the fourth order Runge-Kutta method. The bubble surface and potential distribution were interpolated using a polynomial scheme coupled with the moving least square method for calculating the surface curvature and tangential velocity on the surface. A high quality surface mesh was maintained by implementing a hybrid approach of the Lagrangian method and elastic mesh technique.

We have performed numerical studies with the above numerical model for (i) microbubble dynamics near a wall subject to high intensity ultrasound, (ii) dynamics of ultrasound contrast agents (UCAs) subject to high intensity ultrasound, (iii) microbubble dynamics

with viscous effect and (iv) toroidal bubble dynamics. In parts (ii-iv) the numerical model has been further developed for the phenomena considered.

(i) Microbubble dynamics near a wall subject to high intensity ultrasound

In chapter two, we explored microbubble dynamics near a wall subjected to ultrasound propagating parallel to the wall. The model agrees well with the Rayleigh-Plesset equation for spherical bubbles and the numerical results converge to that for an axisymmetric model for axisymmetric cases. Numerical analyses were carried out for the phenomenon for the dimensionless standoff distance of the bubble at inception from the wall in the range of, $0.75 \leq \gamma \leq 11.25$, and the dimensionless amplitude of pressure of the ultrasound in the range of, $1.5 \leq p_{a*} \leq 1.8$. Some interesting features were observed as follows:

1. The bubble system absorbs the energy from the ultrasound and transforms the uniform momentum of the ultrasound parallel to the wall to the highly concentrated momentum of a high-speed liquid jet pointing to the wall. As compared without the presence of ultrasound, the jet develops much faster and with a significantly higher speed. This mechanism is associated with applications to ultrasonic cleaning, sonochemistry and ultrasound therapeutics as illustrated in the introduction.

2. The direction of the jet depends mainly on the dimensionless standoff distance γ. It is directed towards the wall when the bubble is close to the wall as γ is about 1.5 or smaller, and rotates to the wave direction as γ increases. When γ is about 10 or larger, the wall effects are negligible and the jet is along the direction of the ultrasound. When γ is about 3.5, the Bjerknes forces due to the ultrasound and the wall respectively are comparable and the jet is directed along the bisector of the two directions.

3. The jet width decreases with the standoff distance γ while the jet velocity increases with γ.

4. The jet direction does not change significantly with the amplitude and frequency of the ultrasound, but its velocity increases with the amplitude and decreases with the frequency. The jet is relatively sharper for a larger bubble and/or subject to an ultrasound at a higher frequency.

5. The bubble centroid moves towards the wall and along the ultrasound direction. This motion increases with the amplitude of the ultrasound. When the bubble initiates nearer to the wall, its migration to the wall increases and its migration along the ultrasound decreases.

6. The bubble jet and the motion of the bubble centroid are roughly along the direction of the Kelvin impulse of the bubble. The Kelvin impulse increases with the amplitude of the ultrasound and the closeness of the bubble to the wall.

(ii) Dynamics of ultrasound contrast agents (UCAs) subject to high intensity ultrasound

In chapter three, Nonspherical deformation of ultrasound contrast agents and associated bubble jetting are important in biomedical applications because they can cause breakup and thereby shorten the residence time of contrast agents or facilitate drug release from carrier capsules. A three-dimensional model of ultrasound contrast agents (UCAs) subject to high intensity ultrasound has been developed based on the boundary integral method. The effects of a thin encapsulating shell are approximated by adapting Hoffs model. The model has been validated against a modified Rayleigh-Plesset equation for spherical oscillations of a coated bubble.

Numerous parametric studies were performed for a coated bubble in an infinite fluid as well as near a rigid wall subject to ultrasound propagating both parallel and perpendicular to the wall. In the latter case, a standing wave is generated due to the reflection of the acoustic wave from the rigid wall. Simulations of the dynamic response of a coated bubble

subject to ultrasound lead to the following observations:

1. For a coated bubble subject to ultrasound, some of the energy is absorbed by the coating while it deforms and the bubble dynamics are less violent compared to an uncoated bubble. The existence of a coating thus reduces the maximum volume and period of oscillation significantly, while increasing the minimum volume at the end of collapse. The coating also makes the jet shape sharper and decreases the Kelvin impulse and jet velocity.

2. When the amplitude of the ultrasound is sufficiently strong, a coated bubble deforms nonspherically at the end of the collapse and a jet develops along the acoustic wave direction when the bubble is in an infinite liquid. The threshold of the ultrasound amplitude required to excite jetting is increased due to the presence of a coating, again since some of the energy is absorbed by the coating.

3. When the bubble is near a wall and subject to ultrasound propagating parallel to the wall, the direction of the jet depends mainly on the dimensionless standoff distance γ for both coated and uncoated bubbles. This is because that the bubble dynamics are attenuated due to existence of the coating however the two Bjerknes forces reduce at a similar rate due to existence of the coating. The jet is directed towards the wall when the bubble is close to the wall (when γ is about 1.5 or smaller), and rotates toward the acoustic wave direction as increases. When is about 10 or larger, the wall effects are negligible and the jet is almost entirely along the acoustic wave direction. When γ is about 3.75, the primary and secondary Bjerknes forces due to the ultrasound and the wall, respectively, are comparable and the jet is directed along the bisector of the two directions.

4. The jet becomes sharper and the jet velocity and maximum volume increase with the dimensionless standoff distance γ, analogous to bubble dynamics without a coating.

5. The jet velocity, maximum volume and centroid movement decrease with shell thickness, and the rate of decrease increases with dimensionless standoff distance, γ. This demonstrates that the bubble dynamics are predominantly determined by the secondary Bjerknes force when the bubble is close to the rigid boundary.

6. As the shell viscosity is increased, the maximum volume and centroid movement of the bubble do not change significantly, but the jet velocity decreases. This suggests that the energy dissipated by the bubble coating is not significant globally, but is significant at the jet location where the strain is large.

7. For all cases of both coated and uncoated bubbles, the jet direction is approximately along the direction of the Kelvin impulse at the end of collapse, as the two Bjerknes forces reduce in a similarly way as bubble dynamics are attenuated by the coating.

(iii) Microbubble dynamics with viscous effect

Microbubble dynamics are usually associated with an irrotational flow in the bulk volume but a thin vorticity layer at the bubble surface. This phenomenon has thus been studied in chapter four using the boundary integral method (BIM) based on the viscous potential flow theory. The viscous effects are incorporated into the model through the normal stress balance at the bubble surface. In addition, the viscous correction pressure [50, 51] is implemented to resolve the discrepancy between the nonzero shear stress of the irrotational flow at a free surface and the physical boundary condition of zero shear stress.

The BIM model agrees well with the Gilmore equation for a spherical bubble oscillating in a viscous liquid for several cycles at $R_e = 10$. It agrees with the experimental data for transient bubble dynamics near a rigid boundary. We compared the maximum velocity of the bubble jet at $R_e = 200$ calculated using the axisymmetric VOF model [83] and the BIMs based on the inviscid potential flow theory (IPF), viscous potential flow theory (VPF) and the viscous correction of VPF (VCVPF), respectively. The results of all the

three BIMs correlate with the VOF in general. The jet velocity obtained using the VPF is smaller than the IPF and the jet velocity obtained using the VCVPF is smallest and closest to the VOF.

We analyse dynamics of bubbles at the size of micrometres near a rigid boundary subject to ultrasound in parameter regimes of clinical relevance and observed the following features.

1. The bubble absorbs and concentrates energy from ultrasound, resulting violent collapsing and jetting. This generates a rapid local flow of liquid around the bubble, which induces oscillating normal and shear stresses at membranes nearby, thus have the potential to enhance permeability of lipid bilayers.

2. The jet is directed to the boundary when the ultrasound propagates perpendicular to the wall. When the ultrasound propagates parallel to the wall, the jet is directed towards the wall when the standoff distance is small ($\gamma \leq 1.5$), along the acoustic wave direction as $\gamma \geq 10$ and along the bisector of the two directions around $\gamma \approx 4$.

3. When the bubble is located near the boundary, the jet velocity decreases significantly, being about 1000, 260 m/s at $\gamma = 4$, 1 respectively for the cases considered; the radius of the middle cross-section of the jet increases, being about 5% R_0, 20% R_0 at $\gamma = 4$, 1 respectively, where R_0 is the initial bubble radius.

4. Significant viscous effects are associated with acoustic microbubble dynamics, which cause the decreasing of the maximum volume, oscillation period, Kelvin impulse of the bubble and the energy of the bubble system. The direction of bubble jetting does not change significantly due to the viscous effects but the jet velocity decreases and the jet becomes thinner. The changes are relatively large as R_e changes from 50 to 13, but much smaller as R_e changes from ∞ to 50. This suggests the viscous effects are small as R_e is 50 or larger.

(iv) Toroidal bubble dynamics

In chapter five we simulated three-dimensional toroidal bubble using vortex ring model. It is challenging to simulate three dimensional toroidal bubble dynamics, which are associated with strong numerical instabilities due to jet impact, topological transition, and bubble rebound. A few of developments are described in chapter five to improve the vortex ring model for three dimensional toroidal bubbles. The transform from a singly connected bubble to a toroidal bubble is performed automatically. A finer mesh is generated by splitting each of triangles into four triangles after jet impact, to describe the local geometry associated a hole through the bubble penetrated by the bubble. The potential due to a vortex ring is calculated by using the Biot-Savart law where the integral from the infinite to the point considered is performed analytically. We evaluate the numerical model by comparing with the axisymmetric BIM and the experiment result. We analyse toroidal bubble dynamics subject to buoyancy near a vertical wall, including jet impacting and rebounding toroidal bubbles with oblique jetting.

6.2 Possible future developments

We have developed a robust computational model for simulation of three-dimensional microbubble dynamics considering the viscous effects. This model can be applied for more complex phenomena. One of the possible development is to model the interaction of a few bubbles, which are associated with wide applications [75, 94, 29, 64, 103]. It will be interesting and challenging to model coalescence two bubbles.

Another development is to model acoustic microbubble dynamics in a tube, which is associated with important biomedical applications [75, 16, 95, 103, 129]. The high speed liquid jet has clear potential to damage/penetrate the boundary. However, in the real situation, the jet speed will be attenuated or re-directed by the elastic deformation of the vessel boundary. The elasticity deformation of the vessel boundary should thus be modelled.

In the current study we assume that the liquid is incompressible, since the Mach number associated with bubble dynamics is usually small. However compressibility effects may not be not negligible in some cases particularly at the end of violent collapse, which is associated with emission of shockwaves [66]. Wang & Blake [121, 122], and Wang [119, 120] recently developed the weakly compressible flow theory for bubble dynamics. In the theory, the flow in the inner region near the bubble is approximately incompressible to second order in terms of the Mach number, and the flow in the outer region far away is obtained analytically. The compressible effects are appeared in the far field condition for the inner solution. We thus can develop the current three dimensional incompressible model to include the compressible effects using the weakly compressible flow theory.

List of References

[1] T. B. Benjamin and A. T. Ellis. The collapse of cavitation bubbles and the pressures thereby produced against solid boundaries. *Philosophical Transactions for the Royal Society of London. Series A, Mathematical and Physical Sciences*, pages 221–240, 1966.

[2] J. P. Best. The formation of toroidal bubbles upon the collapse of transient cavities. *Journal of Fluid Mechanics*, 251:79–107, 1993.

[3] J. P. Best and J. R. Blake. An estimate of the kelvin impulse of a transient cavity. *Journal of Fluid Mechanics*, 261:75–94, 1994.

[4] J. P. Best and A. Kucera. A numerical investigation of non-spherical rebounding bubbles. *Journal of Fluid Mechanics*, 245:137–154, 1992.

[5] P. R. Birkin, T. G. Leighton, and Y. E. Watson. The use of acoustoelectrochemistry to investigate rectified diffusion. *Ultrasonics sonochemistry*, 11(3):217–221, 2004.

[6] V. F. K. Bjerknes. Fields of force, 1906.

[7] J. R. Blake, G. S. Keen, R. P. Tong, and M. Wilson. Acoustic cavitation: the fluid dynamics of non–spherical bubbles. *Philosophical Transactions of the Royal Society of London. Series A: Mathematical, Physical and Engineering Sciences*, 357(1751):251–267, 1999.

[8] J. R. Blake, B. B. Taib, and G. Doherty. Transient cavities near boundaries. part 1. rigid boundary. *Journal of Fluid Mechanics*, 170:479–497, 1986.

[9] J. R. Blake, B. B. Taib, and G. Doherty. Transient cavities near boundaries part 2. free surface. *Journal of Fluid Mechanics*, 181:197–212, 1987.

[10] J. M. Boulton-Stone and J. R. Blake. Gas bubbles bursting at a free surface. *Journal of Fluid Mechanics*, 254:437–466, 1993.

[11] C. E. Brennen. *Cavitation and bubble dynamics*. Oxford University Press, New York, 1995.

[12] M. L. Calvisi, J. I. Iloreta, and A. J. Szeri. Dynamics of bubbles near a rigid surface subjected to a lithotripter shock wave. part 2. reflected shock intensifies non-spherical cavitation collapse. *Journal of Fluid Mechanics*, 616:63–97, 2008.

[13] M. L. Calvisi, O. Lindau, J. R. Blake, and A. J. Szeri. Shape stability and violent collapse of microbubbles in acoustic traveling waves. *Physics of Fluids (1994-present)*, 19(4):047101, 2007.

[14] A. R. Carson, C. F. McTiernan, L. Lavery, A. Hodnick, M. Grata, X. Leng, J. Wang, X. Chen, R. A. Modzelewski, and F. S. Villanueva. Gene therapy of carcinoma using ultrasound-targeted microbubble destruction. *Ultrasound in medicine & biology*, 37(3):393–402, 2011.

[15] G. L. Chahine and T. O. Perdue. Simulation of the three-dimensional behavior of an unsteady large bubble near a structure. In *Drops and bubbles: third international colloquium*, volume 197, pages 188–199. AIP Publishing, 1990.

[16] D. Chatterjee, P. Jain, and K. Sarkar. Ultrasound-mediated destruction of contrast microbubbles used for medical imaging and drug delivery. *Physics of Fluids (1994-present)*, 17(10):100603, 2005.

[17] D. Chatterjee and K. Sarkar. A newtonian rheological model for the interface of microbubble contrast agents. *Ultrasound in medicine & biology*, 29(12):1749–1757, 2003.

[18] H. Chen, W. Kreider, A. A. Brayman, M. R. Bailey, and T. J. Matula. Blood vessel deformations on microsecond time scales by ultrasonic cavitation. *Physical review letters*, 106(3):034301, 2011.

[19] C. C. Church. The effects of an elastic solid surface layer on the radial pulsations of gas bubbles. *The Journal of the Acoustical Society of America*, 97(3):1510–1521, 1995.

[20] R. H. Cole and R. Weller. Underwater explosions. *Physics Today*, 1(6):35–35, 2009.

[21] C. C. Coussios and R. A. Roy. Applications of acoustics and cavitation to noninvasive therapy and drug delivery. *Annu. Rev. Fluid Mech.*, 40:395–420, 2008.

[22] G. A. Curtiss, D. M. Leppinen, Q. X. Wang, and J. R. Blake. Ultrasonic cavitation near a tissue layer. *Journal of Fluid Mechanics*, 730:245–272, 2013.

[23] N. De Jong, R. Cornet, and C. T. Lancee. Higher harmonics of vibrating gas-filled microspheres. part one: simulations. *Ultrasonics*, 32(6):447–453, 1994.

[24] N. De Jong, R. Cornet, and C. T. Lancee. Higher harmonics of vibrating gas-filled microspheres. part two: Measurements. *Ultrasonics*, 32(6):455–459, 1994.

[25] N. De Jong, M. Emmer, A. Van Wamel, and M. Versluis. Ultrasonic characterization of ultrasound contrast agents. *Medical & biological engineering & computing*, 47(8):861–873, 2009.

[26] N. de Jong and L. Hoff. Ultrasound scattering properties of albunex microspheres. *Ultrasonics*, 31(3):175–181, 1993.

[27] N. de Jong, L. Hoff, T. Skotland, and N. Bom. Absorption and scatter of encapsulated gas filled microspheres: theoretical considerations and some measurements. *Ultrasonics*, 30(2):95–103, 1992.

[28] M. Delius, R. Denk, C. Berding, H. G. Liebich, M. Jordan, and W. Brendel. Biological effects of shock waves: Cavitation by shock waves in piglet liver. *Ultrasound in medicine & biology*, 16(5):467–472, 1990.

[29] R. Dijkink and C. D. Ohl. Laser-induced cavitation based micropump. *Lab on a Chip*, 8(10):1676–1681, 2008.

[30] S. Dindyal and C. Kyriakides. Ultrasound microbubble contrast and current clinical applications. *Recent patents on cardiovascular drug discovery*, 6(1):27–41, 2011.

[31] A. A. Doinikov and A. Bouakaz. Review of shell models for contrast agent microbubbles. *Ultrasonics, Ferroelectrics and Frequency Control, IEEE Transactions on*, 58(5):981–993, 2011.

[32] A. A. Doinikov and A. Bouakaz. Effect of a distant rigid wall on microstreaming generated by an acoustically driven gas bubble. *Journal of Fluid Mechanics*, 742:425–445, 2014.

[33] A. A. Doinikov, J. F. Haac, and P. A. Dayton. Modeling of nonlinear viscous stress in encapsulating shells of lipid-coated contrast agent microbubbles. *Ultrasonics*, 49(2):269–275, 2009.

[34] A. A. Doinikov, J. F. Haac, and P. A. Dayton. Resonance frequencies of lipid-shelled microbubbles in the regime of nonlinear oscillations. *Ultrasonics*, 49(2):263–268, 2009.

[35] A. A. Doinokov. *Bubble and Particle Dynamics in Acoustic Fields: Modern Trends and Applications: 2005*. Research Signpost, 2006.

[36] B. Dollet, S. M. Van Der Meer, V. Garbin, N. De Jong, D. Lohse, and M. Versluis. Nonspherical oscillations of ultrasound contrast agent microbubbles. *Ultrasound in medicine & biology*, 34(9):1465–1473, 2008.

[37] D. Fernandez Rivas, L. Stricker, A. G. Zijlstra, H. J. Gardeniers, D. Lohse, and A. Prosperetti. Ultrasound artificially nucleated bubbles and their sonochemical radical production. *Ultrasonics sonochemistry*, 20(1):510–524, 2013.

[38] K. Ferrara, R. Pollard, and M. Borden. Ultrasound microbubble contrast agents: fundamentals and application to gene and drug delivery. *Biomedical Engineering*, 9, 2007.

[39] S. W. Fong, E. Klaseboer, and B. C. Khoo. Interaction of microbubbles with high intensity pulsed ultrasound. *The Journal of the Acoustical Society of America*, 123(3):1784–1793, 2008.

[40] S. W. Fong, E. Klaseboer, C. K. Turangan, B. C. Khoo, and K. C. Hung. Numerical analysis of a gas bubble near bio-materials in an ultrasound field. *Ultrasound in medicine & biology*, 32(6):925–942, 2006.

[41] P. J. A. Frinking and N. de Jong. Acoustic modeling of shell-encapsulated gas bubbles. *Ultrasound in medicine & biology*, 24(4):523–533, 1998.

[42] F. R. Gilmore. The growth or collapse of a spherical bubble in a viscous compressible liquid. 1952.

[43] R. Goldman. Curvature formulas for implicit curves and surfaces. *Computer Aided Geometric Design*, 22(7):632–658, 2005.

[44] L. Hoff. *Acoustic characterization of contrast agents for medical ultrasound imaging*. Kluwer Academic Publishers, Dordrecht, Netherlands, 2001.

[45] L. Hoff, P. C. Sontum, and J. M. Hovem. Oscillations of polymeric microbubbles: Effect of the encapsulating shell. *The Journal of the Acoustical Society of America*, 107(4):2272–2280, 2000.

[46] N. A. Hosny, G. Mohamedi, P. Rademeyer, J. Owen, Y. Wu, M. X. Tang, R. J. Eckersley, E. Stride, and M. K. Kuimova. Mapping microbubble viscosity using fluorescence lifetime imaging of molecular rotors. *Proceedings of the National Academy of Sciences*, 110(23):9225–9230, 2013.

[47] C. T. Hsiao and G. L. Chahine. Breakup of finite thickness viscous shell microbubbles by ultrasound: A simplified zero-thickness shell model. *The Journal of the Acoustical Society of America*, 133(4):1897–1910, 2013.

[48] J. I. Iloreta, N. M. Fung, and A. J. Szeri. Dynamics of bubbles near a rigid surface subjected to a lithotripter shock wave. part 1. consequences of interference between incident and reflected waves. *Journal of Fluid Mechanics*, 616:43–61, 2008.

[49] A. R. Jamaluddin, G. J. Ball, C. K. Turangan, and T. G. Leighton. The collapse of single bubbles and approximation of the far-field acoustic emissions for cavitation induced by shock wave lithotripsy. *Journal of Fluid Mechanics*, 677:305–341, 2011.

[50] D. Joseph, T. Funada, J. Wang, and J. Wang. *Potential flows of viscous and viscoelastic liquids*, volume 21. Cambridge University Press UK, 2007.

[51] D. D. Joseph and J. Wang. The dissipation approximation and viscous potential flow. *Journal of Fluid Mechanics*, 505:365–377, 2004.

[52] D. D. Joseph, J. Wang, and T. Funada. The motion of a spherical gas bubble in viscous potential flow, 2005.

[53] S. Kaul. Microbubbles and ultrasound: a bird's eye view. *Transactions of the American Clinical and Climatological Association*, 115:137–148, 2004.

[54] J. E. Kennedy, F. Wu, G. R. Ter Haar, F. V. Gleeson, R. R. Phillips, M. R. Middleton, and D. Cranston. High-intensity focused ultrasound for the treatment of liver tumours. *Ultrasonics*, 42(1):931–935, 2004.

[55] H. Kim, J. C. Padrino, and D. D. Joseph. Viscous effects on kelvin–helmholtz instability in a channel. *Journal of Fluid Mechanics*, 680:398–416, 2011.

[56] S. J. Kim, K. H. Lim, and C. Kim. Deformation characteristics of spherical bubble collapse in newtonian fluids near the wall using the finite element method with ale formulation. *Korea-Australia Rheology Journal*, 18(2):109–118, 2006.

[57] E. Klaseboer, S. W. Fong, C. K. Turangan, B. C. Khoo, A. J. Szeri, M. L. Calvisi, G. N. Sankin, and P. Zhong. Interaction of lithotripter shockwaves with single inertial cavitation bubbles. *Journal of fluid mechanics*, 593:33–56, 2007.

[58] E. Klaseboer and B. C. Khoo. Boundary integral equations as applied to an oscillating bubble near a fluid-fluid interface. *Computational Mechanics*, 33(2):129–138, 2004.

[59] E. Klaseboer and B. C. Khoo. An oscillating bubble near an elastic material. *Journal of applied physics*, 96(10):5808–5818, 2004.

[60] E. Klaseboer, R. Manica, D. YC Chan, and B. C. Khoo. Bem simulations of potential flow with viscous effects as applied to a rising bubble. *Engineering Analysis with Boundary Elements*, 35(3):489–494, 2011.

[61] K. Kooiman, M. R. Böhmer, M. Emmer, H. J. Vos, C. Chlon, W. T. Shi, C. S. Hall, S. HPM. de Winter, K. Schroën, M. Versluis, de Jong N., and van Wamel A. Oil-filled polymer microcapsules for ultrasound-mediated delivery of lipophilic drugs. *Journal of Controlled Release*, 133(2):109–118, 2009.

[62] K. Kooiman, M. Foppen-Harteveld, A. FW. van der Steen, and N. de Jong. Sonoporation of endothelial cells by vibrating targeted microbubbles. *Journal of Controlled Release*, 154(1):35–41, 2011.

[63] H. Lamb. Hydrodynamics cambridge university press. *Cambridge, UK*, 1932.

[64] S. Lauterborn and W. Urban. Ultrasonic cleaning of submerged membranes for drinking water applications. *Journal of the Acoustical Society of America*, 123(5):3291–3291, 2008.

[65] W Lauterborn and H Bolle. Experimental investigations of cavitation-bubble collapse in the neighbourhood of a solid boundary. *Journal of Fluid Mechanics*, 72(02):391–399, 1975.

[66] W. Lauterborn and T. Kurz. Physics of bubble oscillations. *Reports on Progress in Physics*, 73(10):106501, 2010.

[67] T. G. Leighton. The acoustic bubble. 1994. *ISBN: 0-12-44190-8*, 1994.

[68] T. G. Leighton. Bubble population phenomena in acoustic cavitation. *Ultrasonics Sonochemistry*, 2(2):S123–S136, 1995.

[69] T. G. Leighton, F. Fedele, A. J. Coleman, C. McCarthy, S. Ryves, A. M. Hurrell, A. De Stefano, and P. R. White. A passive acoustic device for real-time monitoring of the efficacy of shockwave lithotripsy treatment. *Ultrasound in medicine & biology*, 34(10):1651–1665, 2008.

[70] T. A. Leslie and J. E. Kennedy. High-intensity focused ultrasound principles, current uses, and potential for the future. *Ultrasound quarterly*, 22(4):263–272, 2006.

[71] S. J. Lind and T. N. Phillips. The effect of viscoelasticity on a rising gas bubble. *Journal of Non-Newtonian Fluid Mechanics*, 165(15):852–865, 2010.

[72] S. J. Lind and T. N. Phillips. The influence of viscoelasticity on the collapse of cavitation bubbles near a rigid boundary. *Theoretical and Computational Fluid Dynamics*, 26(1-4):245–277, 2012.

[73] S. J. Lind and T. N. Phillips. The effect of viscoelasticity on the dynamics of gas bubbles near free surfaces. *Physics of Fluids (1994-present)*, 25(2):022104, 2013.

[74] O. Lindau and W. Lauterborn. Cinematographic observation of the collapse and rebound of a laser-produced cavitation bubble near a wall. *Journal of Fluid Mechanics*, 479:327–348, 2003.

[75] J. R. Lindner. Microbubbles in medical imaging: current applications and future directions. *Nature Reviews Drug Discovery*, 3(6):527–533, 2004.

[76] Y. Liu, K. Sugiyama, S. Takagi, and Y. Matsumoto. Surface instability of an encapsulated bubble induced by an ultrasonic pressure wave. *Journal of Fluid Mechanics*, 691:315–340, 2012.

[77] T. S. Lundgren and N. N. Mansour. Vortex ring bubbles. *Journal of Fluid Mechanics*, 224(5):177–196, 1991.

[78] P. Marmottant and S. Hilgenfeldt. Controlled vesicle deformation and lysis by single oscillating bubbles. *Nature*, 423(6936):153–156, 2003.

[79] P. Marmottant, S. van der Meer, M. Emmer, M. Versluis, N. de Jong, S. Hilgenfeldt, and D. Lohse. A model for large amplitude oscillations of coated bubbles accounting for buckling and rupture. *The Journal of the Acoustical Society of America*, 118(6):3499–3505, 2005.

[80] D. J. May, J. S. Allen, and K. W. Ferrara. Dynamics and fragmentation of thick-shelled microbubbles. *Ultrasonics, Ferroelectrics and Frequency Control, IEEE Transactions on*, 49(10):1400–1410, 2002.

[81] H. Miao, S. M. Gracewski, and D. Dalecki. Ultrasonic excitation of a bubble inside a deformable tube: Implications for ultrasonically induced hemorrhage. *The Journal of the Acoustical Society of America*, 124(4):2374–2384, 2008.

[82] Louis Melville Milne-Thomson. *Theoretical hydrodynamics*. Courier Dover Publications, 1996.

[83] V. Minsier, J. De Wilde, and J. Proost. Simulation of the effect of viscosity on jet penetration into a single cavitating bubble. *Journal of Applied Physics*, 106(8):084906, 2009.

[84] K. E. Morgan, J. S. Allen, P. A. Dayton, J. E. Chomas, A. L. Klibaov, and K. W. Ferrara. Experimental and theoretical evaluation of microbubble behavior: Effect of transmitted phase and bubble size. *Ultrasonics, Ferroelectrics and Frequency Control, IEEE Transactions on*, 47(6):1494–1509, 2000.

[85] W. L. Nyborg. Ultrasonic microstreaming and related phenomena. *The British journal of cancer. Supplement*, 5:156, 1982.

[86] C. D. Ohl, M. Arora, R. Dijkink, V. Janve, and D. Lohse. Surface cleaning from laser-induced cavitation bubbles. *Applied physics letters*, 89(7):074102, 2006.

[87] C. D. Ohl, M. Arora, R. Ikink, N. de Jong, M. Versluis, M. Delius, and D. Lohse. Sonoporation from jetting cavitation bubbles. *Biophysical journal*, 91(11):4285–4295, 2006.

[88] M. Overvelde, V. Garbin, J. Sijl, B. Dollet, N. De Jong, D. Lohse, and M. Versluis. Nonlinear shell behavior of phospholipid-coated microbubbles. *Ultrasound in medicine & biology*, 36(12):2080–2092, 2010.

[89] A. Pearson, J. R. Blake, and S. R. Otto. Jets in bubbles. *Journal of engineering mathematics*, 48(3-4):391–412, 2004.

[90] T. J. Pedley. The toroidal bubble. *Journal of Fluid Mechanics*, 32(01):97–112, 1968.

[91] A. Philipp and W. Lauterborn. Cavitation erosion by single laser-produced bubbles. *Journal of Fluid Mechanics*, 361:75–116, 1998.

[92] M. S. Plesset and A. Prosperetti. Bubble dynamics and cavitation. *Annual Review of Fluid Mechanics*, 9(1):145–185, 1977.

[93] S. Popinet and S. Zaleski. Bubble collapse near a solid boundary: a numerical study of the influence of viscosity. *Journal of Fluid Mechanics*, 464:137–163, 2002.

[94] M. Postema, A. van Wamel, J. Folkert, and N. de Jong. High-speed photography during ultrasound illustrates potential therapeutic applications of microbubbles. *Medical physics*, 32(12):3707–3711, 2005.

[95] S. Qin, C. F. Caskey, and K. W. Ferrara. Ultrasound contrast microbubbles in imaging and therapy: physical principles and engineering. *Physics in medicine and biology*, 54(6):R27, 2009.

[96] S. Qin and K. W. Ferrara. Acoustic response of compliable microvessels containing ultrasound contrast agents. *Physics in medicine and biology*, 51(20):5065, 2006.

[97] S. Qin and K. W. Ferrara. The natural frequency of nonlinear oscillation of ultrasound contrast agents in microvessels. *Ultrasound in medicine & biology*, 33(7):1140–1148, 2007.

[98] L. Rayleigh. On the pressure developed in a liquid during the collapse of a spherical cavity. *The London, Edinburgh, and Dublin Philosophical Magazine and Journal of Science*, 34(200):94–98, 1917.

[99] W. W. Roberts, T. L. Hall, K. Ives, J. S. Wolf Jr, J. B. Fowlkes, and C. A. Cain. Pulsed cavitational ultrasound: a noninvasive technology for controlled tissue ablation (histotripsy) in the rabbit kidney. *The Journal of urology*, 175(2):734–738, 2006.

[100] K. Sarkar, W. T. Shi, D. Chatterjee, and F. Forsberg. Characterization of ultrasound contrast microbubbles using in vitro experiments and viscous and viscoelastic interface models for encapsulation. *The Journal of the Acoustical Society of America*, 118(1):539–550, 2005.

[101] W. D. Song, M. H. Hong, B. Lukyanchuk, and T. C. Chong. Laser-induced cavitation bubbles for cleaning of solid surfaces. *Journal of applied physics*, 95(6):2952–2956, 2004.

[102] E. Stride and N. Saffari. Microbubble ultrasound contrast agents: a review. *Proceedings of the Institution of Mechanical Engineers, Part H: Journal of Engineering in Medicine*, 217(6):429–447, 2003.

[103] E. P. Stride and C. C. Coussios. Cavitation and contrast: the use of bubbles in ultrasound imaging and therapy. *Proceedings of the Institution of Mechanical Engineers, Part H: Journal of Engineering in Medicine*, 224(2):171–191, 2010.

[104] K. S. Suslick. Sonochemistry. *Science*, 247(4949):1439–1445, 1990.

[105] Y. Tomita and A. Shima. Mechanisms of impulsive pressure generation and damage pit formation by bubble collapse. *Journal of Fluid Mechanics*, 169:535–564, 1986.

[106] K. Tsigklifis and N. A. Pelekasis. Simulations of insonated contrast agents: Saturation and transient break-up. *Physics of Fluids (1994-present)*, 25(3):032109, 2013.

[107] K. Tsiglifis and N. Pelekasis. Radial oscillations of insonated contrast agents: Effect of the membrane constitutive. *J. Acoust. Soc. Am*, 123(6):4059, 2008.

[108] S. M. van der Meer, B. Dollet, M. M. Voormolen, C. T. Chin, A. Bouakaz, N. de Jong, M. Versluis, and D. Lohse. Microbubble spectroscopy of ultrasound contrast agents. *The Journal of the Acoustical Society of America*, 121(1):648–656, 2007.

[109] A. Vogel, W. Lauterborn, and R. Timm. Optical and acoustic investigations of the dynamics of laser-produced cavitation bubbles near a solid boundary. *Journal of Fluid Mechanics*, 206:299–338, 1989.

[110] H. J. Vos, B. Dollet, J. G. Bosch, M. Versluis, and N. De Jong. Nonspherical vibrations of microbubbles in contact with a walla pilot study at low mechanical index. *Ultrasound in medicine & biology*, 34(4):685–688, 2008.

[111] H. J. Vos, B. Dollet, M. Versluis, and N. De Jong. Nonspherical shape oscillations of coated microbubbles in contact with a wall. *Ultrasound in medicine & biology*, 37(6):935–948, 2011.

[112] C. Wang and B. C. Khoo. An indirect boundary element method for three-dimensional explosion bubbles. *Journal of Computational Physics*, 194(2):451–480, 2004.

[113] C. Wang, B. C. Khoo, and K. S. Yeo. Elastic mesh technique for 3d bim simulation with an application to underwater explosion bubble dynamics. *Computers & fluids*, 32(9):1195–1212, 2003.

[114] J. Wang and D. D. Joseph. Purely irrotational theories of the effect of the viscosity on the decay of free gravity waves. *Journal of Fluid Mechanics*, 559:461–472, 2006.

[115] J. Wang, D. D. Joseph, and T. Funada. Viscous contributions to the pressure for potential flow analysis of capillary instability of two viscous fluids. *Physics of Fluids (1994-present)*, 17(5):052105, 2005.

[116] Q. X. Wang. The evolution of a gas bubble near an inclined wall. *Theoretical and computational fluid dynamics*, 12(1):29–51, 1998.

[117] Q. X. Wang. Numerical simulation of violent bubble motion. *Physics of Fluids (1994-present)*, 16(5):1610–1619, 2004.

[118] Q. X. Wang. Unstructured mel modelling of nonlinear unsteady ship waves. *Journal of Computational Physics*, 210(1):368–385, 2005.

[119] Q. X. Wang. Non-spherical bubble dynamics of underwater explosions in a compressible fluid. *Physics of Fluids (1994-present)*, 25(7):072104, 2013.

[120] Q. X. Wang. Multi-oscillations of a bubble in a compressible liquid near a rigid boundary. *Journal of Fluid Mechanics*, 745:509–536, 2014.

[121] Q. X. Wang and J. R. Blake. Non-spherical bubble dynamics in a compressible liquid. part 1. travelling acoustic wave. *Journal of Fluid Mechanics*, 659:191–224, 2010.

[122] Q. X. Wang and J. R. Blake. Non-spherical bubble dynamics in a compressible liquid. part 2. acoustic standing wave. *Journal of Fluid Mechanics*, 679:559–581, 2011.

[123] Q. X. Wang and K. Manmi. Three dimensional microbubble dynamics near a wall subject to high intensity ultrasound. *Physics of Fluids (1994-present)*, 26(3):032104, 2014.

[124] Q. X. Wang, K. S. Yeo, B. C. Khoo, and K. Y. Lam. Nonlinear interaction between gas bubble and free surface. *Computers & fluids*, 25(7):607–628, 1996.

[125] Q. X. Wang, K. S. Yeo, B. C. Khoo, and K. Y. Lam. Strong interaction between a buoyancy bubble and a free surface. *Theoretical and Computational Fluid Dynamics*, 8(1):73–88, 1996.

[126] Q. X. Wang, K. S. Yeo, B. C. Khoo, and K. Y. Lam. Vortex ring modelling of toroidal bubbles. *Theoretical and Computational Fluid Dynamics*, 19(5):303–317, 2005.

[127] B. Yang and A. Prosperetti. Vapour bubble collapse in isothermal and non-isothermal liquids. *Journal of Fluid Mechanics*, 601:253–279, 2008.

[128] Y. X. Yang, Q. X. Wang, and T. S. Keat. Dynamic features of a laser-induced cavitation bubble near a solid boundary. *Ultrasonics sonochemistry*, 20(4):1098–1103, 2013.

[129] C. S. Yoon and J. H. Park. Ultrasound-mediated gene delivery. *Expert opinion on drug delivery*, 7(3):321–330, 2010.

[130] V. Zderic, A. A. Brayman, S. R. Sharar, L. A. Crum, and S. Vaezy. Microbubble-enhanced hemorrhage control using high intensity focused ultrasound. *Ultrasonics*, 45(1):113–120, 2006.

[131] A. M. Zhang and B. Y. Ni. Three-dimensional boundary integral simulations of motion and deformation of bubbles with viscous effects. *Computers & Fluids*, 92:22–33, 2014.

[132] A. M. Zhang, X. L. Yao, and X. B. Yu. The dynamics of three-dimensional underwater explosion bubble. *Journal of Sound and Vibration*, 311(3):1196–1212, 2008.

[133] S. Zhang and J. H. Duncan. On the nonspherical collapse and rebound of a cavitation bubble. *Physics of Fluids (1994-present)*, 6(7):2352–2362, 1994.

[134] S. Zhang, J. H. Duncan, and G. L. Chahine. The final stage of the collapse of a cavitation bubble near a rigid wall. *Journal of Fluid Mechanics*, 257:147–181, 1993.

[135] Y. L. Zhang, K. S. Yeo, B. C. Khoo, and C. Wang. 3d jet impact and toroidal bubbles. *Journal of Computational Physics*, 166(2):336–360, 2001.